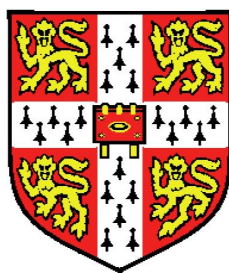


Metal Oxide / Organic Interface Investigations for Photovoltaic Devices



Olympia Pachoumi
Magdalene College
University of Cambridge

A thesis submitted for the degree of

Doctor of Philosophy

July 2014

To my parents

Acknowledgements

This thesis summarises work I have carried out as a PhD student of the Optoelectronics Group at Cavendish Laboratory of the University of Cambridge since October 2010. I am thankful to the Engineering and Physical Sciences Research Council and the A.G. Leventis Foundation for funding my research as well as Magdalene College for financial support towards the attendance of conferences. It has been quite a journey until I was able to complete this manuscript and I would like to take this opportunity to thank all those remarkable individuals who have contributed one way or another towards this work and who have made my journey worthwhile.

I would like to thank my supervisor Prof. Henning Sirringhaus for giving me the opportunity to work in his research group and pursue the projects I have, given me being a solar cell enthusiast in his transistor family. I would also like to thank him for all our discussions, his spectrum of knowledge and his insight are really inspiring, and especially for being as supportive as he has been, he appears to have a magic ability to resurrect ones motivation. Special thanks go to Dr Kulbinder Banger who has supported me all the way through my PhD and who I consider as my mentor. I want to thank him for offering me the opportunity to work on one of his projects and sharing his wisdom on experimental methods, showing me the way towards being more efficient and productive. I also want to thank Dr Yana Vaynzof, with whom I have worked very closely, for her support, for discussions and advice regarding my experimental results as well as for running experiments together. I thank Dr Cheng Li for sharing his knowledge and experience on metal oxides and for his electroabsorption spectroscopy

measurements. It has been an absolute delight collaborating with Cheng. I would like to thank Dr Artem Bakulin, Dr Chaw Keong and Aditya Sadhanala who have contributed towards this work with their expertise. Of course it is always good to have someone around when the spectrophotometer goes crazy in the dark-room or when you are in need of a great working transistor; for that I thank Iyad Nasrallah, who has been a great help with my spectroscopy experiments. I thank the OE and ME Group staff and in specific Dr Radoslav Chakalov, Dr Richard Gymer, Mrs Emily Heavens, Mr. Roger Beadle and Mr Alex Cook for making sure that everything is running smoothly.

Furthermore I would like to thank all the OE people for making this group such a pleasant environment to work. Thanks go to my current office mates Carlo, John and Deepak for coping with the tension of having four near-the-end PhD students in the same room and to my former office mates Josie, Chris, Milan, Iyad and Vahe for some scientific talk, brainstorming and mostly for the energising breaks. Special thanks to the people who made me feel so welcome in the OE when I was still a fresher; Sebi, Thomas, Aurelie, Riccardo, Mijung, Georgui, Chiara, Michael and Vincenzo and to the 2014 CUTECH Committee for making the past year so much fun. Kyriaki, Marina and Evangelia thank you for all the group therapy sessions along with coffee, tea, or sangria. Thanks to my high-school girlfriends for snapping me out of the hectic PhD life once in a while.

Finally, I can't thank my parents, Marina and Michali, enough for their endless support on every step of the way and for always being present, although 2000 miles away. I thank them for all the faith they have in me and for coping with my absence for eight years now. My sisters, Monica and Myrto thank you for always being there when I need you. My grandma, Olympia, thanks for spoiling me.

For all the time I spent as a PhD student here in Cambridge, every single day, every single achievement or failure wouldn't have been as fun and unique as they have been and still are if it weren't for

Panayiotis. I want to thank him for having to listen to me whine about all things that go wrong, he has been a constant source of motivation for me.

I declare that except where specific reference is made to the involvement of others, the work presented herein is my own. This dissertation has not been submitted in whole or in part for the award of a degree at this, or any other university and does not exceed 60,000 words in length.

Olympia Pachoumi
Magdalene College Cambridge, July 2014

Abstract

This thesis outlines investigations of metal oxide / organic interfaces in photovoltaic devices. It focuses on device instabilities originating from the metal oxide layer surface sensitivity and it presents suggested mechanisms behind these instabilities.

A simple sol-gel solution deposition technique for the fabrication of stable and highly performing transparent conducting mixed metal oxides (ZnMO) is presented. It is demonstrated that the use of amorphous, mixed metal oxides allows improving the performance and stability of interfacial charge extraction layers for organic solar cells. Two novel ternary metal oxides, zinc-strontium-oxide (ZnSrO) and zinc-barium-oxide (ZnBaO), were fabricated and their use as electron extraction layers in inverted organic photovoltaics is investigated. We show that using these ternary oxides can lead to superior devices by: preventing a dipole forming between the oxide and the active organic layer in a model ZnMO / P3HT:PCBM OPV as well as lead to improved surface coverage by a self assembled monolayer and promote a significantly improved charge separation efficiency in a ZnMO / P3HT hybrid device.

Additionally a spectroscopic technique allowing a versatility of characterisation for long-term stability investigations of organic solar cells is reported. A device instability under broadband light exposure in vacuum conditions for an inverted ZnSrO/PTB7:PC₇₀BM OPV is observed. Direct spectroscopic evidence and electrical characterisation indicate the formation of the PC₇₀BM radical anion associated with a loss in device performance. A charge transfer mechanism between a heavily doped oxide layer and the organic layers is suggested and discussed.

Contents

1	Introduction	1
2	Background	5
2.1	Oxide Semiconductors: zinc oxide	6
2.1.1	Electronic Structure	6
2.1.2	Electronic Properties	11
2.1.3	Surface Oxygen	14
2.1.4	Sol-gel Processing	17
2.2	Organic Semiconductors	18
2.2.1	Origin of Semiconducting Property	18
2.2.2	Optical Processes	19
2.2.3	Neutral and Charged Excitations	21
2.3	Organic Photovoltaic Devices	23
2.3.1	Charge Photogeneration	23
2.3.2	Built-in Potential	26
2.3.3	Open-circuit Voltage	28
2.3.4	Stability and Degradation	29
2.4	Organic Field Effect Transistors	32
	References	33
3	Experimental Methods	41
3.1	Materials	41
3.1.1	<i>P</i> -type Polymers	41
3.1.2	Fullerene Derivatives	44
3.1.3	ZnO, ZnSrO and ZnBaO	45

3.1.4	Tungsten Trioxide	46
3.2	Thin Film Fabrication	46
3.2.1	Organic Layer	47
3.2.2	Mixed Metal Oxides	48
3.2.3	Electron Blocking Layer	49
3.2.4	Electrode Deposition	49
3.3	Material Characterisation	51
3.3.1	Profilometry	51
3.3.2	Morphology Probes (<i>AFM, SEM, XRD</i>)	51
3.3.3	UV-Vis Spectroscopy	52
3.3.4	Photoemission Spectroscopy	53
3.3.5	Photothermal Deflection Spectroscopy	54
3.3.6	Electrical Conductivity	55
3.4	Device Characterisation	56
3.4.1	Photovoltaic Device Performance	56
3.4.2	Electroabsorption Spectroscopy	58
3.4.3	Pump-Push Photocurrent Spectroscopy	62
	References	63
4	ZnSrO and ZnBaO Electron Extraction Layers for Inverted Organic Photovoltaics	67
4.1	Introduction	68
4.2	Metal Oxide Characterisation	71
4.2.1	Chemical Composition	72
4.2.2	Surface and Bulk Microstructure	75
4.2.3	Optical Transmission	77
4.2.4	Surface Potentials	78
4.2.5	Electrical Conductivity	81
4.3	Device Performance	83
4.3.1	Doping Level	84
4.3.2	EQE Preliminary Measurements	86
4.3.3	UV Light Exposure and Nitrogen Annealing	87
4.4	Improvement Mechanism	91

4.4.1	Interfacial Band Alignment	92
4.4.2	Chemical Composition Stability	94
4.4.3	Built-in Potential	97
4.4.4	Electrical Hysteresis	99
4.5	Conclusions	101
	References	101
5	Interfacial Modification for Oxide/Polymer Hybrid Photovoltaics	107
5.1	Introduction	108
5.2	ZnSrO/P3HT Hybrid PV Devices	109
5.2.1	Doping Level and Device Performance	109
5.2.2	Open-circuit Voltage Improvement Discussion	111
5.2.3	Interfacial Charge Separation	113
5.3	Interfacial Modification Using PCBA	114
5.3.1	Device Performance	115
5.3.2	Charge Separation Efficiency	117
5.4	Conclusions	119
	References	120
6	Charge Accumulation Spectroscopy for Organic Photovoltaics	123
6.1	Introduction	124
6.2	Optical Transmittance	126
6.3	High Sensitivity Optical Spectroscopy Setup	128
6.4	External Light Source	130
6.5	Device Architecture Optimisation	133
6.5.1	Device Active Area	135
6.5.2	Transparent Top Electrode	137
6.6	Charge Induced Absorption in PTB7 Devices	138
6.6.1	PTB7 Field Effect Transistor	138
6.6.2	PTB7:PCBM Solar Cell	142
6.7	Conclusions	147
	References	148

7	Inverted Organic Photovoltaic Device Stability Investigations	151
7.1	Introduction	152
7.2	Operational Stability in Vacuum	153
7.2.1	Charge Induced Absorption	154
7.2.2	Device Performance	159
7.2.3	Suggested Mechanism	161
7.3	Operational Stability in Ambient Air	164
7.4	Conclusions	165
	References	167
8	Conclusions and Outlook	171

List of Figures

2.1	Neutral Oxygen (O) and Metal (M) atoms in vacuum (left) and respective ionised species in an oxide semiconductor stabilised by the Madelung potential (right). Adapted from Kamiya <i>et al.</i> ² . . .	7
2.2	Schematic electronic structure for oxide semiconductors indicating possible subgap defect states.	9
2.3	(Left) ZnO surface charge distribution and band bending after exposure to oxygen in the dark. (Right) Schematic illustration used by Verbakel <i>et al.</i> ²¹ to describe the UV light and bias voltage induced changes in the ZnO surface.	15
2.4	Energy diagram showing ground state absorptions (blue), excited state absorptions (red) and radiative emissions (green) that could be taking place for a conjugated polymer.	22
2.5	Molecular orbitals in the neutral state and in the presence of a polaron. Eg denotes the band-gap energy of the molecule whereas P1 and P2 show the polaron induced absorption.	23
2.6	Illustration of electronic processes taking place at a Donor/Acceptor (D/A) organic photovoltaic. An Frenkel exciton is formed at the donor upon photon absorption (1) which then diffuses at the D/A heterojunction (2) where it undergoes charge transfer forming a short-lived CT state (3) and further separating into free charges collected at the electrodes (4). <i>Loss mechanisms are not shown.</i> . . .	24

2.7	(a) The state model of charge separation, where dashed arrows represent optical transitions and γ and δ represent the relative amounts of BCP and free charges respectively. (b),(c) Corresponding band diagrams without and with interfacial modification. Reproduced from Vaynzof <i>et al.</i> ⁴⁴	25
2.8	<i>Inverted</i> and <i>Hybrid</i> OPV device architectures.	26
2.9	Schematic diagram of an established build-in potential, equal to the workfunction difference between the two electrodes. The arrows show the built-in field driven drift mechanism for photogenerated charges.	27
2.10	Suggested degradation mechanisms involving the polymer triplet state (left) and the interfacial CT state (right); figures adapted from Soon <i>et al.</i> ⁶⁷ and Grancini <i>et al.</i> ⁶⁸ respectively.	31
2.11	Device architecture of a bottom-contact top-gate field-effect transistor, where V_{gs} and V_{ds} is the voltage applied respectively to the gate and drain while the source is grounded. Negative and positive signs show an example of charge accumulation in a p-type semiconductor for a negative V_{gs}	33
3.1	Molecular structures of (a) P3HT and (b) PTB7 p-type polymers	43
3.2	Molecular structures of fullerene derivatives	44
3.3	Molecular alkoxide precursors	45
3.4	Ionisation potential (I_P), work-function (WF), Fermi level (E_F) and valence band minimum (E_{VBM}) estimated from a typical UPS spectrum. The inset shows the corresponding band diagram, where E_{VAC} denotes the vacuum level, E_{CBM} the conduction band minimum and E_g the band-gap energy (usually obtained from UV-Vis absorption spectroscopy). <i>HBEC</i> stands for high binding energy cut-off.	55
3.5	Sample configuration for two-point probe conductivity measurements.	56

LIST OF FIGURES

3.6	Dark (dashed) and under illumination (solid) current-voltage (IV) curves of a typical organic solar cell. V_{OC} is the open-circuit voltage, I_{SC} the short-circuit current whereas V_{MPP} and J_{MPP} the maximum power point voltage and current respectively.	58
3.7	Device architecture (a) and energy levels representation (b) diagrams. Figure kindly provided by C.Li.	60
3.8	(Left) J-V Device characteristics and (right) EQE of test device. Figures provided by C.Li.	60
3.9	(Left) First harmonic EA spectrum at -3V and first derivative of pure P3HT UV-Visible absorption spectrum and corresponding (right) EA response. Figures provided by C.Li.	61
3.10	(Left) Light intensity dependence of EA signal and (right) AC frequency dependence of the EA signal.	62
4.1	Zn2 <i>p</i> and O1 <i>s</i> XPS scans for ZnO.	72
4.2	Zn2 <i>p</i> , O1 <i>s</i> and Sr3 <i>d</i> XPS scans for ZnSrO.	73
4.3	Zn2 <i>p</i> , O1 <i>s</i> and Ba3 <i>d</i> XPS scans for ZnBaO.	74
4.4	XPS depth profiles for ZnO (top), Zn _{0.97} Sr _{0.03} O (bottom left) and Zn _{0.97} Ba _{0.03} O (bottom right) films on Si substrate.	75
4.5	θ - 2θ X-ray diffractogram of ZnO, Zn _{0.97} Sr _{0.03} O and Zn _{0.97} Ba _{0.03} O films on glass, annealed at 300 ⁰ C, showing no evidence of crystalline nature (background noise has been subtracted).	76
4.6	AFM surface morphology of ZnO (top), Zn _{0.97} Sr _{0.03} O (middle) and Zn _{0.97} Ba _{0.03} O (bottom) films on Si wafer, made at 300 ⁰ C. All three films show similar root mean square surface roughness (R_{rms}) close to 1nm.	77
4.7	SEM cross-sections of cleaved ZnO (left), Zn _{0.97} Sr _{0.03} O (centre) and Zn _{0.97} Ba _{0.03} O (right) films on silicon substrates.	77
4.8	Transmittance spectra for ZnO, Zn _{0.97} Sr _{0.03} O and Zn _{0.97} Ba _{0.03} O thin films on quartz glass substrate.	78

4.9	UPS spectra for ZnO, Zn _{0.97} Sr _{0.03} O and Zn _{0.97} Ba _{0.03} O thin films on Si substrate with annotated positioning of the onset (denoting the work function) and edge of absorption (denoting the valence band minimum).	80
4.10	Electrical current voltage characteristics for as prepared, N ₂ annealed and UV light exposed ZnO, Zn _{0.97} Sr _{0.03} O and Zn _{0.97} Ba _{0.03} O thin films on glass substrate with planar Al source-drain electrodes (W=3mm, L=100μm).	81
4.11	Schematic structure of an inverted organic photovoltaic device. . .	84
4.12	V _{OC} , J _{SC} , FF and power conversion efficiency (PCE), under 100 mWcm ⁻² AM 1.5G solar simulator conditions, for P3HT:PC ₆₀ BM inverted OPV devices with a ZnMO EEL against doping % where M is Sr (top) and Ba (bottom). Results for undoped ZnO are obtained from a single batch of devices.	85
4.13	J-V curves for best performing devices measured under 100mWcm ⁻² AM 1.5G solar simulator conditions.	86
4.14	The effect of (left) UV monochromatic light during an EQE measurement and (right) forward bias on EQE measurements.	87
4.15	External quantum efficiency (EQE) characteristics before and after light exposure (top) and with annealing in N ₂ atmosphere (bottom) of devices with ZnO, Zn _{0.97} Sr _{0.03} O and Zn _{0.97} Ba _{0.03} O EELs.	88
4.16	Current density - voltage characteristics in the dark (top) and under 580nm monochromatic illumination before and after light exposure of devices with ZnO, Zn _{0.97} Sr _{0.03} O and Zn _{0.97} Ba _{0.03} O EELs (corresponding to figure 4.15 top figure.	90
4.17	(top) UPS spectra for ZnO, ZnO/P3HT, ZnO/PC ₆₀ BM and ZnO/blend, (middle) UPS spectra for Zn _{0.97} Sr _{0.03} O, Zn _{0.97} Sr _{0.03} O/P3HT, Zn _{0.97} Sr _{0.03} O/PC ₆₀ BM and Zn _{0.97} Sr _{0.03} O/blend and (bottom) UPS spectra for Zn _{0.97} Ba _{0.03} O, Zn _{0.97} Ba _{0.03} O/P3HT, Zn _{0.97} Ba _{0.03} O/PC ₆₀ BM and Zn _{0.97} Ba _{0.03} O/blend where blend is P3HT:PC ₆₀ BM	92
4.18	Comparison of O1s scan for ZnO, Zn _{0.97} Sr _{0.03} O and Zn _{0.97} Ba _{0.03} O thin films.	95

LIST OF FIGURES

4.19	Surface oxygen % content with respect to the O1s XPS scans with prolonged UV light ($\sim 1 \text{ mWcm}^{-2}$, 375 - 405 nm) exposure time for ZnO, $\text{Zn}_{0.97}\text{Sr}_{0.03}\text{O}$ and $\text{Zn}_{0.97}\text{Ba}_{0.03}\text{O}$ thin films.	95
4.20	Change in O1s scan after 13h UV exposure for $\text{Zn}_{0.97}\text{Sr}_{0.03}\text{O}$ film.	96
4.21	Electroabsorption (EA) response measurements of OPV with ZnO, $\text{Zn}_{0.97}\text{Sr}_{0.03}\text{O}$ and $\text{Zn}_{0.97}\text{Ba}_{0.03}\text{O}$ as EEL, before (left) and after (right) UV light exposure. The built-in potential V_{bi} is determined from the extrapolation of the linear regime in reverse bias (+ applied bias).	98
4.22	Dark current-voltage characteristics of OPV devices in air. First a sweep was carried out starting from reverse bias (-3 V to +3 V) and then a reverse scan was measured starting from forward bias (+3 V to -3 V).	100
5.1	Schematic structure of a ZnO/organic hybrid photovoltaic device.	109
5.2	(a) V_{OC} , (b) J_{SC} , (c) FF and (d) PCE of ZnSrO/P3HT photovoltaic devices with varying % of Sr doping. Measurements carried out by Dr Vaynzof.	111
5.3	UV-Vis absorption spectra for ZnO and ZnSrO.	112
5.4	(a) UPS spectra of the valence band of ZnO and ZnSrO (energy level diagrams are shown in the inset) (b) IV characteristics for ZnO and ZnSrO thin films, (c) dark IV measurements of ZnO/P3HT and ZnSrO/P3HT photovoltaic devices.	113
5.5	(a) PPPc measurements on ZnO/P3HT and ZnSrO/P3HT photovoltaic devices (b) PDS measurements on ZnO and ZnSrO thin films, XPS O1s spectra of (c) ZnO and (d) ZnSrO.	115
5.6	(a) Open circuit voltage (V_{OC}), (b) short circuit current (J_{SC}), (c) fill factor (FF) and (d) power conversion efficiency (PCE) of hybrid photovoltaic devices with and without PCBA modifier. Measurements carried out by Dr Vaynzof.	117

5.7	(a) Pump-push photocurrent spectroscopy measurements on ZnO/P3HT and ZnSrO/P3HT photovoltaic devices with and without PCBA modifier (b) photothermal deflection spectroscopy measurements on ZnO and ZnSrO with and without PCBA modifier, (c) Ultra-violet photoemission spectra of ZnO/PCBA and ZnSrO/PCBA. .	118
5.8	Uv-vis absorption spectra of ZnO/N719 and ZnSrO/N719.	119
6.1	Diagram of the experimental setup, showing the main components of the optical system and the additional modifications needed for OPV optical spectroscopy measurements.	129
6.2	(a) Cryostat modification allowing for external light exposure and gas flow through side window, (b) cryostat top-view showing external light beam in comparison to sample active area (red) placed at an angle and spectrophotometer probe beam (black), (c) absorption spectrum of external white light source.	131
6.3	Non reproducible transmittance spectra taken in the dark and with (a)(b) white and (c) monochromatic external light on.	133
6.4	Device architecture diagram for inverted organic photovoltaic devices used for optical spectroscopy measurements.	134
6.5	(a) J-V characteristics for small and large area devices measured under 100 mWcm^{-2} AM 1.5G solar simulator conditions, (b) EQE for small area reference device, (c) device optical transmittance with three types of top electrodes, (d) J-V characteristics for large area, transparent device measured under the ELS.	136
6.6	Diagram of the bottom-contact top-gate PTB7 field effect transistor.	139
6.7	Transfer characteristics of a working PTB7 p-type OFET in linear (blue) and saturation (black) regimes. Dashed lines indicate the corresponding leakage current.	139
6.8	CAS spectra for a PTB7 transistor measured at different negative and positive voltages.	140

LIST OF FIGURES

6.9	Charge density dependence of the amplitude of the positive polarons (holes) and negative polarons (electrons) induced absorption. The absorption cross sections in each case are extracted from the slop of the linear fit.	141
6.10	CAS spectra for a PTB7 transistor measured at -50 V and +50 V applied V_{gs} showing the positive polaron and negative polaron induced absorption respectively.	142
6.11	CAS spectra for PTB7/PCBM OPV devices measured (a) at different forward voltage bias, (b) at +3 V and different sample orientation with respect to the probing beam and (c) for different ITO top-electrode thickness.	144
6.12	CAS spectra for (a) PTB7/PCBM OPV under forward voltage bias (charge injection) and (b) reverse voltage bias; and (c) for an OPV device (+1V) compared to a PTB7 OFET device ($V_{gs} = -50V$). . .	145
7.1	(a) Differential optical transmittance spectra for OPV device after prolonged light exposure, (b) Normalised area evolution over time under bleaching and CIA signals corresponding to spectra shown in (a), (c) corresponding dark current-voltage characteristics, (d) comparison between kinetics of (i) reverse current increase and (ii) CIA peak transmittance decrease.	156
7.2	(a) Differential spectrum of the transmission in the Vis/UV region, compared with absorption spectrum of a bare PCBM film and the first derivative of the PTB7 bare film absorption, changes in transmission of a (b) ZnSrO/PTB7:PCBM multilayer sample, (c) PTB7:PCBM sample and (d) ZnSrO sample after 50 hours of light exposure in vacuum.	157
7.3	Light current-voltage characteristics after different times of light exposure under vacuum (left) and respective key performance parameters (V_{OC} , I_{SC} and FF)(right).	159

7.4	(a) V_{OC} against $\ln(J_{SC}/J_0)$ for prolonged light exposure under vacuum conditions. V_{OC} and J_{SC} parameters were extracted from results shown in figure 7.3 and J_0 from the dark IV measurements shown in figure 7.1 (b) Ideality factor, n , as derived from slope against light exposure time.	160
7.5	(Left) UPS spectra for an as prepared ZnSrO thin film compared to one that has been subjected to an additional 1 hour annealing step at 300°C in Nitrogen atmosphere. The absorption onset shows an increased WF and the edge of absorption shows an increase in the VBM and hence n-type doping. The inset shows corresponding energy level diagrams. (Right) PPC decay for a bare ZnSrO film and a PCBM covered ZnSrO film. Insert is the same in a double logarithmic scale.	163
7.6	Change in transmission with constant illumination in air for OPV PTB7:PCBM device (left) and a PTB7:PCBM bare film (right). Graphs are offset for clarity.	165

List of Tables

3.1	Sample substrates and application	47
3.2	Organic solutions and processing conditions	48
3.3	Top-electrodes and deposition details	51
4.1	Cation radii and Gibbs energy of oxidation data on metal oxides ²⁶	70
4.2	Summary of metal oxides surface potential key parameters.	80
4.3	Summary of metal oxide/organic interface band alignment key parameters.	93

Chapter 1

Introduction

Organic photovoltaics (OPV) or solar cells is a promising technology for energy generation offering a variety of benefits that give a new perspective to solar power harvesting. The photovoltaic (PV) industry has been around for nearly 60 years and the traditional crystalline PV emerged as an environmentally stable technology promising clean and sustainable energy generation. Significant advances in material and device development utilising nanomaterials and nanotechnology has led to remarkable improvements in the efficiency of photovoltaics. OPV offers the additional advantage of low cost solution processed organic semiconductors allowing for the promising potential of printed solar cells. Thin film low temperature deposition has lead to flexible, lightweight solar modules radically transforming the traditional picture of a bulky rigid solar panel. High-speed manufacturing as well as low fabrication and transportation costs mean that remote, off-grid areas are now more accessible too. As a result of extensive research on the design and synthesis of conjugated polymers and small molecules remarkable progress has been made and power conversion efficiencies of 10% and above were reported recently. The operational stability and sensitivity to atmospheric components of these solar cells on the other hand is currently a challenging weakness. A significant improvement in the research field of OPV device stability happened around 2005 with the introduction of new device architecture, the inverted structure, which eliminated the need of a low work-function cathode. It was realised that the use of inorganic materials such as conducting metal oxides would inhibit photodegradation in air in inverted and hybrid photovoltaics, however there were

several implications with the use of solution processed metal oxides.

In this work we investigate the properties of photovoltaic devices and individual component materials in order to improve our understanding of metal oxide / organic interfacial processes in photovoltaics and suggest pathways towards more efficient systems, having a particular focus on degradation and stability. This dissertation explores two major concepts: (i) engineering improved novel mixed metal oxides and implementing them in devices and (ii) developing and using a high-resolution optical spectroscopy setup suitable for studying device stability. This research project was structured by first identifying a device instability, gaining good understanding of its origin and suggesting and implementing a way to be overcome. Then, we setup and use a spectroscopic technique to perform further investigations and build on the knowledge acquired along the way to conclude on the operation of an inverted device.

During the course of this project we came across different concepts, theories and their experimental manifestations; some of which are well understood and described and others are highly debatable. Reviewing the existing literature and keeping track of the relevant ongoing research was essential in understanding our results. In Chapter 2 a literature review of the most relevant background the motivation of this project is based on, as well as the interpretation of experimental results, is presented; whereas in Chapter 3 the materials used and established experimental methods are described. Our efforts to engineer and apply a novel set of mixed metal oxides is first presented in Chapter 4. Since we have fabricated novel materials we present an extensive material characterisation and have accumulated a variety of data on which future experiments were based on. In this chapter we discuss about the *UV light-soaking* step required in inverted solar cells with a solution processed zinc oxide electron transport layer and show how it can be circumvented by doping of zinc oxide with alkaline earth metals. We support our findings by carrying out sophisticated device characterisation and we suggest a mechanism behind this improvement. After having achieved a better performing inverted device we implement the hybrid device architecture and focus on charge separation at the oxide/organic interface to gain more insight into the interfacial physics of this system; this is summarised in Chapter 5. As our understanding of the processes and mechanisms taking place in the test devices

is growing we introduce a spectroscopic technique in order to characterise the in-situ stability of device in long time scales under different conditions. We present in Chapter 6 the challenges and our efforts towards establishing this technique and obtaining reliable data whereas finally in Chapter 7 we show our first data obtained. We identify an instability associated with prolonged light exposure in a reduced oxygen environment and we propose an associated charge transfer mechanism from the oxide to the organic. Finally in Chapter 8 we summarise the key conclusions of this project and discuss on the possible impact of our results as well as on the potential of the spectroscopic technique we have developed and further experiments that would add further value to our findings.

Chapter 2

Background

Since this thesis is dedicated to investigating photovoltaic systems where metal oxide/organic interfaces are involved we present in this chapter an overview of the fundamental concepts in the field of organic semiconductors, transparent conducting oxides and solar cells which are necessary to follow the discussions presented in the rest of the thesis. First we present a description of the electronic properties of zinc oxide and discuss on its optical, electronic and surface properties. We then introduce the theory behind the origin of the semiconducting properties of organic polymers and some of the optical processes that enable us to establish a connection between theories of electronic states and their experimental manifestations. We finish with an overview of device operation for organic and hybrid photovoltaics as well as a brief reference to organic field effect transistors.

2.1 Oxide Semiconductors: zinc oxide

In this section we introduce the fundamental and current understanding of electronic structures of oxide semiconductors and in specific for the case of zinc oxide. We will discuss the role of the oxide's structure in the resulting electronic properties such as the polycrystalline and amorphous natures. Oxide semiconductors are popular materials for thin film transistors (TFTs) because of their high mobility values, high transparency and large band-gap along with the ease of processing for large areas. Oxide semiconductors are often used in many other optoelectronic devices such as photovoltaics and light emitting diodes. Sufficiently conducting oxides with the appropriate electron affinities and ionisation potentials, can be employed as charge transport and injection layers and improve the energy level matching between an active organic semiconductor layer and the respective electrode.

In specific the majority of research involves ZnO due to its high transparency in the visible region, high carrier mobility compared to other n-type oxides, good solution processibility and low cost. The conduction band and valence band energy levels of undoped ZnO have been reported to lie around 4.1 - 4.4 eV and 7.6 - 7.8 eV respectively making it good electron selective layer.

Routes followed to improve the efficiency in such systems include the enhancement of ZnO film conductivity and the modification of workfunction by doping with group III elements. Besides the good functionality of ZnO in solar cells, thin films exhibit an instability under ambient air conditions and the conductivity of such films was shown to be sensitive to the presence of surrounding atmospheric gases and especially oxygen. Recently, Nomura *et al.* reported that amorphous oxide semiconductors (AOS) with the composition $a - InGaZnO_4$ (a-IGZO) can be applied in the fabrication of flexible, transparent TFTs having much improved performance and stability compared to conventional TFTs based on a-Si:H and organic materials.¹

2.1.1 Electronic Structure

ZnO films normally have a crystalline or poly-crystalline character even when deposited at low temperatures. The crystal structures shared by ZnO are wurtzite,

2.1 Oxide Semiconductors: zinc oxide

zinc blende and rocksalt. The thermodynamically stable structure of ZnO is the hexagonal wurtzite where the zinc (Zn) atoms are tetrahedrally co-ordinated to four oxygen (O) atoms with the O anions occupying the tetrahedral sites. This tetrahedral coordination is typical of sp^3 covalent bonding nature, however oxide semiconductors have strong ionicity and charge transfer occurs from metal to oxygen atoms.

The conduction band minimum (CBM) and valence band minimum (VBM) are formed of different ionic species. In the particular case of ZnO, which has a very strong ionicity the VBM is formed almost solely by the anion (occupied oxygen 2p-states) and the CBM is made mainly by the cation (unoccupied 4s Zn-states), although the anions still show some contribution. Under these circumstances the electronic structure is stabilized by the Madelung potential formed by these ions, raising the electronic levels in cations and lowering the levels in anions as illustrated in Figure 2.1. For a metal atom M and an oxygen atom O being apart in vacuum the highest occupied atomic orbitals for their stable neutral states are very close. When they come close an electron transfer occurs due to the difference in electron affinities resulting in the ionised form of the atoms. The resulting electrostatic potential formed between the cation and anion sites is the Madelung potential, which consequently stabilises the ionised states.

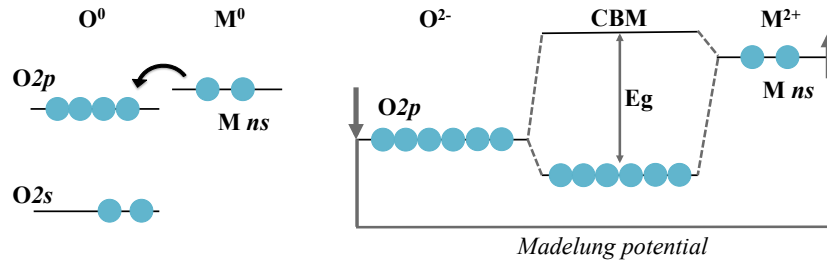


Figure 2.1: Neutral Oxygen (O) and Metal (M) atoms in vacuum (left) and respective ionised species in an oxide semiconductor stabilised by the Madelung potential (right). Adapted from Kamiya *et al.*²

Since the CB in oxides is mainly made of the empty spherically extended s orbitals of the heavy metal cations, they are characterised by large band dispersion which was used to explain the large electron mobilities in amorphous

mixed metal oxide structures which was initially thought unlikely due to strong scattering often present in disordered structures.³

2.1.1.1 Defect States

Generally unintentionally doped polycrystalline ZnO thin films exhibit n-type conductivity attributed to deviation from stoichiometry. The n-type conductivity met naturally in the wurtzite structure is usually attributed either to native defects such as the Zn-on-O antisite, the Zn interstitial and the oxygen vacancy or foreign atoms such as a hydrogen in ZnO, however there is a great deal of controversy over which of these defects is the dominant source of n-type conductivity. In oxides the energy levels of an oxygen vacancy (V_o) (the non-bonding state of the metal cation) can be formed in or near the CB allowing the vacancies to act as a shallow donor but not as an effective electron trap. However, such donor states are not stable in many oxides and the oxygen deficiencies can either form shallow donors or deep occupied states depending on the local structure of the oxygen deficiency. In the case of ZnO, first-principles calculations have shown that (V_o) forms a deep fully-occupied state and hence it is not likely that it is contributing towards the n-type conductivity of in unintentionally doped films.⁴ The formation energy of these deep oxygen deficiencies is found to depend on the coordination structure around (V_o), with an increasing energy for increasing coordination number of the metal ion.⁵ Later we see how this feature is being exploited when synthesising more efficient and stable new mixed metal oxides.

An other native defect of ZnO that could be responsible for the donor levels is the zinc interstitial (Zn_i). Despite Zn_i being a shallow donor ($\sim 30\text{meV}$), a background donor concentration of $\sim 10^{16}$ is not expected to be dominated by Zn_i due to its high formation energy. It is possible, however that a complex of Zn_i defects might occur at lower formation energy. On the other hand first-principles studies suggested that none of the native defects shows the characteristics of high concentration shallow donors. In other cases it has been suggested that the n-type conductivity of unintentionally doped ZnO is only due to hydrogen, which is a shallow donor.

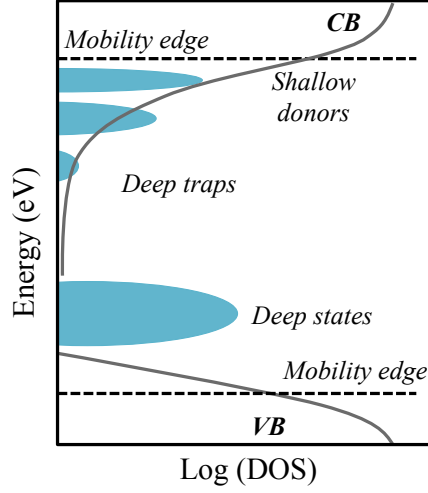


Figure 2.2: Schematic electronic structure for oxide semiconductors indicating possible subgap defect states.

This is further supported by first-principles calculations; hydrogen can potentially diffuse easily into ZnO in large amounts, due to its high mobility, as it is always present in all growth methods. Figure 2.2 shows a schematic electronic structure of an oxide semiconductor indicating potential shallow donor states just below the CBM and trap states or deep states just above the VBM. In theory any of these states should result in subgap absorption and for a sufficiently high absorption coefficient could be detected experimentally. The spread of suggestions, calculations and studies make it difficult to predict the nature of the n-type donors in un-doped ZnO grown by a variety of techniques including magnetron sputtering, CVD, spray pyrolysis and sol-gel.⁶

2.1.1.2 Doping

For low resistivity at room temperature to be achieved as desired, ZnO conductivity need to be enhanced. The two most common approaches followed are: (i) the creation of intrinsic donors i.e. to introduce lattice defects such as oxygen vacancies or Zn atoms on interstitial sites by controlling the deposition conditions or (ii) the introduction of extrinsic dopants i.e. substituting Zn-sites with group III elements or halogens with oxidation number minus one on oxygen lattice sites.

Doping is also often implemented as a way to modify the band gap of ZnO. It has been reported before that adding Mg to ZnO increases the bandgap whereas Cd decreases the band gap allowing for band gaps in the range of 2.3 eV to 5.5 eV to be achieved.^{7,8,9} Recently, it has been reported in our group by Hoyer *et al.*⁹ that the bandgap of Mg-doped ZnO does not change much until above 40 at% Mg content when a change to the rock-salt phase from the wurtzite Mg-doped ZnO phase is observed.

For covalent semiconductors doping is explained by the substitution of a host lattice site by an externally added cation/anion based on the number of valence electrons and chemical bonds between the host and dopant. In case of n-type conductivity a metal atom is substituted by a metal with higher valence releasing a free electron which contributes to the n-type conductivity. A typical example is the addition of Al^{+3} to the ZnO lattice by substituting Zn^{+2} . In the case of amorphous oxide semiconductors the concept of substitution does not have a physical valid sense therefore employing a simple counting rule, where the ionised constituents and their formal ionic charges sum is considered, makes more sense.

Recently, there has been increasing interest in amorphous mixed metal oxide systems.^{2,1,10,5} Mixing two or more cations with different ionic charges and different sizes was proven to form high mobility, stable amorphous structures. The additional incorporation of a stabilizer cation that has a strong chemical bond with oxygen ions can be used to control the carrier concentration. One of the main issues with solution processed oxide semiconductors, also discussed later on, is instabilities associated with the adsorption and desorption of O_2 and H_2O related molecules at oxygen deficient sites. Doping with Gallium has shown to improve the long-term stability of InGaZnO TFTs.³ As clarified by first-principles density-functional theory², GaO bonds are much stronger than ZnO bonds, meaning that the incorporation of gallium suppresses the formation of oxygen deficiencies and the consequent generation of mobile electrons. On the other hand, the incorporation of high gallium content deteriorates the electron mobility. The field of mixed metal oxides opens the way towards a great variety new ternary and quaternary oxide systems offering the potential to tune the oxide electronic properties.

2.1.2 Electronic Properties

2.1.2.1 Electrical Conductivity

Transparent conducting oxide properties are described by the Drude free electron theory.¹¹ The electrical conductivity σ for a semiconductor is determined by the product of number of charge carriers n , the mobility μ of these charge carriers and the elementary electron charge e . Resistivity ρ is defined as the inverse of the conductivity.

$$\sigma = en\mu = \frac{1}{\rho} \quad (2.1)$$

From the above equation it is clear that for high conductivity both high electron concentration and high mobility are required. The number of charge carriers can be increased by doping that essentially can be done by substitutional doping, creation of oxygen vacancies and implantation of metal interstitials. Depending on the valence of dopants or vacant sites acceptor/donor sites will induce p/n-type conductivity. The other possibility for promoting conductivity is to increase the electron mobility.

Charge carrier concentration (n): is dependent on the oxide stoichiometry and doping level. N-type conductivity in unintentionally doped ZnO films can be attributed to stoichiometric deviation owing to oxygen deficiency or an excess of metal atoms. An oxygen deficiency such as a doubly charged oxygen vacancy, can be achieved by removing oxygen atoms when treating the film in a reducing environment. Positively charged oxygen vacancies however can act as traps and a high concentration can result in a reduction of the charge carriers and the conductivity. As already mentioned the charge carrier concentration can be increased by n-type doping. As the electron concentration increases with doping, the Fermi energy is shifted towards the conduction band and is moved into the conduction band making it a degenerate semiconductor. At sufficiently high electron concentration the optical band-gap can increase with increasing carrier concentration leading to absorption towards shorter wavelengths. This shift in the band-gap induced by doping is known as the Moss-Burstein shift.^{12,13} A general trend of

lower resistivity with increased carrier concentration has been realised. For the electrical conductivity to be activated the donor levels must be ionised. For ionisation to occur a minimum energy equal to the energy difference between the conduction band minimum and the donor level is required. For a deep donor the ionisation energy might be greater than room temperature and therefore will not contribute towards the conductivity under these conditions. The Fermi energy position increases as the dopant concentration increases however this is valid up to a maximum amount of doping which is described by the solubility of a dopant into the host material. Excess doping will not move the Fermi level any further but instead excess metallic ions are not activated and segregate into the grain boundaries resulting in mobility degradation by impurity and grain boundary scattering.

Charge carrier mobility (m) : The electron mobility (m_e) can be expressed by equation 2.2 where τ is the relaxation time of the charge carriers due to the scattering effects which can be expressed in terms of the drift velocity V_F and mean free path of the charge carriers l_{mfp} . M^* is the charge carrier effective mass.

$$m_e = \frac{e\tau}{M^*} = \frac{el_{mfp}}{M^*V_F} \quad (2.2)$$

Normally more than one source of scattering is present such as lattice scattering, neutral impurity scattering, electron-electron scattering, electron impurity scattering and ionised impurity scattering. At high electron concentration, carrier transport is primarily limited by ionised impurity scattering caused by the Coulomb interaction between the electron and the ionised dopant. Thus beyond an optimum carrier concentration carrier mobility drops and conductivity also starts decreasing. In the case of polycrystalline films, grain boundaries introduce an important scattering mechanism. High density of interface states is concentrated at the boundaries, these act as traps and scattering centres for free charge carriers from the bulk.¹⁴

2.1.2.2 Workfunction

Workfunction is defined as the minimum amount of energy required to remove an electron from a solid to just outside the material at temperature $T = 0$ K. For metal oxide semiconductors the workfunction equals the difference between its fermi energy (E_F) and the vacuum level assuming that the electron is removed from the highest occupied electronic level, to an arbitrary fixed reference, the vacuum level E_{VAC} . Measurements have shown that there are two major material properties contributing towards the workfunction value ($\Phi = -(\mu + q\psi_s)$): a bulk property defined by the chemical potential μ and a surface property defined by the surface potential ψ_s .¹⁵

The workfunction shows a strong dependence on the surface conditions of ZnO and it might vary depending on the orientation of the surface crystal and any surface adsorbates that may cause a dipole layer to form at the surface. Experimental values for the ZnO work function often vary from 3.5 eV to 4.3 eV; the lower limit of 3.5 eV has been observed for a zinc-terminate (0001) polar surface and has been correlated to high charge carrier densities.^{16,17} As we will see later on the measured work function for undoped and doped ZnO used for the purposes of this experiment lies in the range $3.6 \text{ eV} \pm 0.1 \text{ eV}$. The voltage across this dipole layer is defined as the surface potential ψ_s and is essentially a measure of the electron density at the surface. The adsorption of atoms or molecules at the surface can induce charge transfer between the solid and the adsorbate and hence a dipole moment between the two; as a result the surface potential changes. This effect can be approximated by a parallel plate capacitor model and the shift in surface potential is described by:

$$\Delta\psi_s = \frac{n_{ads}}{\epsilon_0 \cdot \epsilon_r} \cdot \mathbf{p} \cdot \mathbf{n}, \quad (2.3)$$

where n_{ads} is the adsorbates density, \mathbf{p} the dipole moment and \mathbf{n} the surface normal unit vector.¹⁸ The dipole moment between an adsorbed molecule and the surface is given by the product of the fractional charge exchange between the two and the position of the adsorbate with respect to the surface. The degree of charge exchange is controlled by the difference in electronegativity of the adsorbate and host surface. An adsorbate of higher/lower electronegativity

than that of the substrate will attract/repel electrons causing a drop/increase in the surface potential and hence an increase/decrease in the workfunction $\Delta\Phi = -\Delta\psi_s$.

2.1.3 Surface Oxygen

One of the principal problems currently hampering most semiconductor device applications of ZnO is a lack of control of the surface properties and electrical conductivity. Metastable phenomena such as persistent photoconductivity with accompanied excessive n-type doping upon illumination and strong sensitivity of thin film surface properties, such as conductivity and workfunction, to the presence of adsorbed species, are very common. While this surface sensitivity of ZnO is being exploited in the field of sensors, UV photodetectors and memory devices, failure to recognise and control them may have been a contributing factor in failed attempts of reproducibility and extreme scatter in performance of ZnO optoelectronic devices. The important role surface and interfacial defects play in optoelectronic device operation has been emphasised in many occasions as well as the need for a better understanding of the mechanisms behind relevant instabilities.

In wurtzite ZnO, the primary polar plane (0001) and associated direction [0001] is the most commonly used surface and direction for growth. This polar surface however is very reactive and unstable in oxidising environments resulting in unstable electrical, structural and optical properties in ambient atmosphere. Instability of ZnO thin films in ambient air has been attributed to O₂ adsorption at the V_o sites on the polar surfaces and/or at the grain boundary interfaces. The presence of adsorbed oxygen at the nanocrystal surface of ZnO films has previously been suggested to lead to electron trapping and reducing the free carrier density. As a result conductivity was shown to decrease on exposure to air and most interestingly was shown to enhance after a forming process of UV exposure or voltage stress. It was verified before using electrostatic force microscopy that UV illumination changes the surface states leading to a change in the electric field within films of ZnO nanoparticles.^{19,20}

Oxygen adsorption on clean ZnO surfaces results in charge transfer of elec-

2.1 Oxide Semiconductors: zinc oxide

trons to the oxygen atoms, producing a negatively charged surface and positively charged donors within the surface space charge region. This causes an upward band bending and an increased carrier concentration toward the surface as shown in figure 2.3(left). Oxygen adsorption near a surface state (e.g. oxygen deficient sites) creates a negatively charged ion by capturing a free electron from n-type ZnO according to equation 2.4. Adsorbed oxygen can also be desorbed under UV irradiation or a voltage bias as photogenerated and injected holes respectively, move towards the surface and neutralise the negative oxygen ion according to equation 2.5. An schematic illustration describing this process is given in figure 2.3(right).

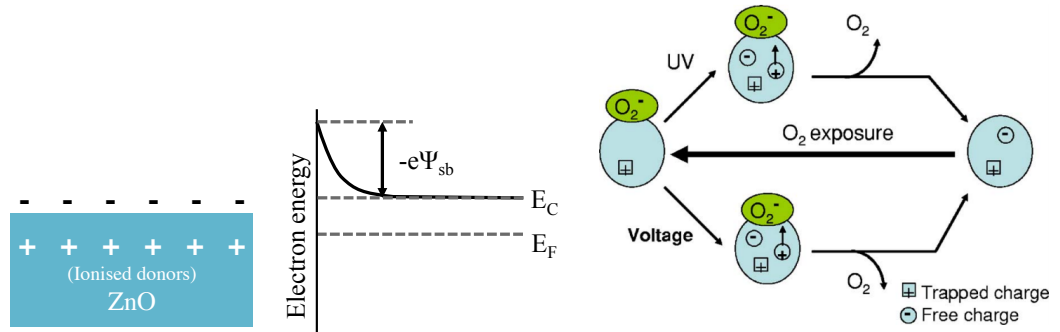


Figure 2.3: (Left) ZnO surface charge distribution and band bending after exposure to oxygen in the dark. (Right) Schematic illustration used by Verbakel *et al.*²¹ to describe the UV light and bias voltage induced changes in the ZnO surface.

2.1.3.1 Persistent Photoconductivity

It has been known for many years that exposure of ZnO to above band-gap light results in an increase in conductivity but persists long after the light is turned off.²² However, two processes with different kinetics were identified for both the activation and relaxation of the photocurrent; a fast process and a slower process

that in both cases continues long after the first process has ended. The initial rapid photocurrent rise can be explained by the initial excitation of electrons to higher energy states. The slower photocurrent rise has been attributed to photoexcited states that exhibit a short lifetime and probability for a lattice relaxation at the surface.²³

The mechanism behind the persistence of photocurrent after turning off illumination is currently under debate. The initial rapid drop can be associated with conduction-band electrons recombining with photogenerated holes at the surface. The slower relaxation might be associated with free carriers interacting with surface states and grain boundaries. It has been argued that UV light causes loosely bound surface oxygen to desorb from the surface resulting in a reduced surface electron depletion region and leading to enhanced photoconductivity. Subsequent re-adsorption of oxygen will result to the recovery of the excess conductivity. Another approach is that adsorption of oxygen at the surface and/or electron trapping in the depletion region increases band bending, resulting in an increased bulk/surface energy barrier that leads to persistence of the photoconductivity.²⁴

The traditional approach to describe the persistent photoconductivity kinetics has been to use the Kohlrausch stretched exponential function analysis, which is often used to describe decays in the presence of an energy transfer in disordered systems. The Kohlrausch function, as it is applied to photocurrent transient relaxation, is as follows:

$$I(t) = I_{sat} \exp[-(t/\tau)^\gamma], \quad (2.6)$$

where I_{sat} is the saturation photocurrent, τ is the relaxation time constant and γ a stretching parameter falling into a range between zero and one to distinguish the kinetics from a classical exponential decay. This persistence is dependent on the availability of ambient oxygen and has led to the suggestion of surface electron depletion region tightly related to the surface density of negatively charged adsorbed surface oxygen species. In vacuum, desorbed oxygen is pumped away, therefore, the state of oxygen desorption persists for longer.

Furthermore in ZnO nanostructures with higher surface area/volume ratio

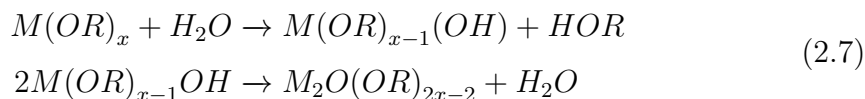
such as nanowires and whiskers, the large increase in photoconductivity observed in vacuum was attributed to surface photolysis of lattice oxygen.^{25,26} Although oxygen vacancies are not likely to contribute towards ZnO electron conductivity they might be correlated with surface trapping mechanisms; they are more likely to be found close to surfaces and their positive charge might attract negatively charged oxygen species.^{27,28}

2.1.4 Sol-gel Processing

Metal oxide thin films on glass substrates, for inverted solar cells, can be prepared by a variety of techniques such as magnetron sputtering²⁹, spray pyrolysis³⁰, sol-gel³¹, chemical vapour deposition and Chemical bath deposition³² resulting in different film properties. In this project we exploit the sol-gel deposition technique due to its simplicity and the diversity it offers in forming high-performance mixed oxide materials from solution at low process temperatures and does not require any sophisticated and expensive equipment.

The sol-gel process is broadly defined as the preparation of ceramic materials (e.g. metal oxides) by preparation of a sol (colloidal suspension of solid particles in a liquid), gelation of the sol (particles in sol attach to each other forming macroscopic network) and removal of the solvent.³³ Metal oxide thin films and ternary oxide semiconductors of the form $M_x^1 M_y^2 O_z$ (where M^1 and M^2 can be metals Al, In, Ga, Sn, Sr, Ba and Zn) can be prepared by spin coating an appropriate precursor, suspended in solution, on substrate followed by annealing (250°C - 350°C) in order to decompose the precursor and remove the organic part. The class of precursors most widely used is the alkoxides which essentially means an organic ligand attached to a metal or metalloid atom. This project is focused on zinc oxide and ternary metal oxide films prepared by the sol gel process as described by K.K.Banger *et al.* that showed remarkable performance in thin film transistors application.^{10,34} When metal alkoxides are exposed to an aqueous environment, hydrolysis and condensation occur by nucleophilic substitution and addition mechanisms. The relative reaction scheme for the hydrolysed formation of metal oxides from alkoxide precursors can be described by the following

reaction:



These reactions involve proton transfer from the incoming water molecule to the bound alkoxide ligand, followed by subsequent elimination of the protonated leaving group, thus affording the MOM frameworks at low temperatures.

2.2 Organic Semiconductors

The broad field of organic electronics involves the utilisation of conductive conjugated polymers or small molecules in electronic applications such as light emitting devices, photovoltaic devices and field effect transistors. A conjugated polymer is a carbon-based macromolecule characterised by strong intramolecular electronic interactions and relatively weak intermolecular electronic interactions; and is hence treated as a quasi-one dimensional system. As a consequence of this quasi-one dimensionality conjugated polymers exhibit properties which are quite different in corresponding inorganic semiconductors e.g electron-electron interactions are weakly screened, electrons and lattice are strongly coupled and they exhibit a wealth of quasi-particles such as excitons, polarons and magnons. Undoped conjugated polymers are semiconductors with optical gaps of $\sim 2 - 3$ eV and large exciton binding energies ($\sim 0.5 - 1.5$ eV). Conduction of conjugated polymers is attributed to the delocalisation of valence π electrons; and it is described by the π -electron theories emerging from the sp^2 hybridisation concept for chemical bond description in organic molecules.

2.2.1 Origin of Semiconducting Property

The concept of sp^n hybridisation emerges from the Linear Combination of Atomic Orbitals (LCAO) method which is used to describe chemical bonds by constructing a new set of orbitals (hybrid orbitals) by mixing appropriate atomic orbitals. For carbon-based molecules the relevant hybrid orbitals are sp , sp^2 and sp^3 resulting from LCAO of the four outer valence orbitals of carbon: $2s$, $2p_x$, $2p_y$

and $2p_z$.³⁵ Considering a bond between two carbon atoms (along the x-axis) sp^2 hybridisation involves the formation of three sp^2 hybrids per carbon atom (constructed from the $2s$, $2p_x$ and $2p_y$ orbitals), forming three σ orbitals. The remaining $2p_z$ orbital forms a π orbital lying perpendicular to the plane. Electrons in σ orbitals are localised in the σ bonds (in plane at 120° to one another) whereas it is possible for electrons in the π orbitals (out of plane) to delocalise (conjugate) throughout the molecule. It is this electron delocalisation that leads to the conducting properties of organic semiconductors.

Ethane (C_2H_4) is the simplest example where sp^2 hybridisation occurs. The two carbons form two σ bonds each with a hydrogen atom whereas overlapping between the two σ and two π ($2p_z$) orbitals on adjacent sides, form a weak double bond. Mixing of the two $2p_z$ orbitals leads to bonding (π) and anti-bonding (π^*) combinations with energy difference defined by the individual atomic potentials. When extending this model to a polymer of chain of $n = \infty$ units, the result is a band of π states between the π (all bonding) and π^* (all anti-bonding) states. Such a configuration predicts a one dimensional metallic conductivity along the chain, however this is not the case due to the “Peierls instability” which states that a one-dimensional metal is unstable with respect to a lattice distortion that opens a bandgap at the Fermi surfaces between the highest occupied molecular orbital (HOMO) and the lowest unoccupied molecular orbital (LUMO); and hence the semiconducting property of conjugated polymers.

2.2.2 Optical Processes

Here we describe some of the important linear and non-linear optical processes that enable us to establish a connection between the electronic states of conjugated polymers and optical spectroscopy measurements. We emphasise on one-photon absorption processes upon interaction of an electromagnetic field with matter. For a system of N polymers per unit volume under the influence of a driving electric field \mathbf{E} the polarisation response \mathbf{P} is,

$$\mathbf{P} = \epsilon_0(\chi^{(1)}\mathbf{E} + \chi^{(2)}\mathbf{E}\mathbf{E} + \chi^{(3)}\mathbf{E}\mathbf{E}\mathbf{E} + \dots), \quad (2.8)$$

where ϵ_0 is the dielectric constant in free space. χ^n denotes the n th order susceptibility and is an $n+1$ order tensor.

Rewriting the above equation as,

$$\mathbf{P} = \chi_{eff}^{(1)}(\mathbf{E})(\mathbf{E}), \quad (2.9)$$

we see that polarisation can be expressed in terms of an electric field dependent linear susceptibility.

Taking into account linear optical processes, for transitions from the ground state, $|0\rangle$, to the excited states, $|J\rangle$, of energies E_J , the first order susceptibility at frequency ω (simplified for a polymer oriented along the x axis) can be expressed in terms of the oscillator strength f_J for the transition from $|0\rangle$ to $|J\rangle$ and the angular transition frequency $\Omega_J = (E_J - E_0)/\hbar$

$$\chi^{(1)}(\omega) = \frac{Ne^2}{m\epsilon_0} \sum_J \frac{f_J}{\Omega_J^2 - \omega^2}, \quad (2.10)$$

$$f_J = \frac{2m}{e^2\hbar} \Omega_J \langle 0 | \hat{\mu}_x | J \rangle^2, \quad (2.11)$$

where $\hat{\mu}_x$ is the component in the x - direction of the dipole operator $\hat{\mu}$ and f_J satisfies,

$$\sum_J f_J = N_e, \quad (2.12)$$

where N_e is the number of π -electrons in the polymer.

The linear absorption coefficient $\alpha(\omega)$, defined as the fraction of energy absorbed in passing through a unit thickness of material can be obtained from the relative permittivity which is equivalent to $\chi^{(1)}(\omega) + 1$ as,

$$\alpha(\omega) = \frac{\pi\omega N}{nc\epsilon_0\hbar} \sum_J \langle 0 | \hat{\mu}_x | J \rangle^2 \delta(\omega - \Omega_J) \quad (2.13)$$

$\langle 0 | \hat{\mu}_x | J \rangle$ is the transition dipole moment and for its evaluation the Frank Condon principle, which assumes that the electronic transition occurs so quickly that the nuclear coordinates remain stationary, is adopted for simplification. Mathematically, this implies that the electronic and nuclear component of the wave-

function can be separated and that the total energy of a given state is a sum of the electronic and vibrational energies, where for each electronic state there is a number of vibronic states with increasing energy. Under the Franck Condon principle the excited states are represented by parabolas, to represent the harmonic potential of the electronic state involved. The allowed electronic/vibronic transitions taking place under absorption of a photon are determined by the selection rules some of which are discussed in the following sections. For each electronic state there is a series of horizontal lines to represent the vibronic levels of increasing energy. Electronic transitions occurring from the ground state to the first excited state and its vibronic replicas are also discussed later on.

2.2.3 Neutral and Charged Excitations

Here we introduce excitations arising from the electronic structure of organic semiconductors. These include neutral and charged excitations. Neutral excited states are formed by the absorption of a photon to form singlet excitons. Due to the low dielectric constant of organic molecules the resulting excited state, known as Frenkel exciton³⁶ is strongly bound ($\sim 0.5 - 1.0$ eV) and it will remain bound unless an extrinsic mechanism, such as an internal potential gradient, separates the electron-hole pair. The strongly bound exciton is one of the major differences organic semiconductors have as compared to inorganic semiconductors where excited states, Wannier excitons³⁷, are weakly bound and separated to charges at room temperature; and it needs to be taken into account when designing organic photovoltaic systems.³⁸ A singlet (S) or triplet (T) exciton can be formed by combining an electron and a hole with individual spins. As optical transitions are only allowed between states of opposite symmetry, light absorption from the ground state (S_0) can only lead to a transition to the first singlet excited state (S_1) or other higher-lying singlet states. Eventually the excited state will radiatively decay to the ground state unless if another mechanism is involved (such as inter-system crossing that can transform singlets into triplets). One possible decay route is the emission of a photon in a process known as fluorescence. The combination of vibrational relaxation and migration to potentially lower energy sites causes the emission to be at lower energy than the absorption and this dif-

ference is called the Stokes shift.³⁹ Figure 2.4 summarises the allowed ground state absorptions (blue), excited state absorptions (red) and radiative emissions (green) that could be taking place for a conjugated polymer.

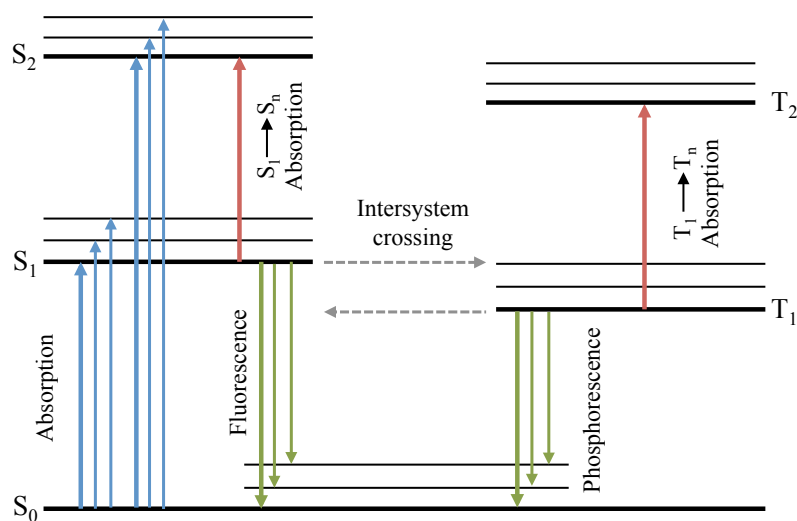


Figure 2.4: Energy diagram showing ground state absorptions (blue), excited state absorptions (red) and radiative emissions (green) that could be taking place for a conjugated polymer.

As the work of this thesis concentrates on charge generation and transport in these photoactive polymers for photovoltaic applications, excitations associated with the charged state of the polymer are of particular interest. As a consequence of strong electron-lattice coupling in the presence of a perturbation such as an electron or a hole the organic molecule reorganises itself into a charge along with a local distortion, known together as a polaron. In the presence of a polaron the electronic levels of the molecule are modified too. The HOMO and LUMO energies are pushed into the gap giving rise to new sub-bandgap optical transitions; this is illustrated in figure 2.5.

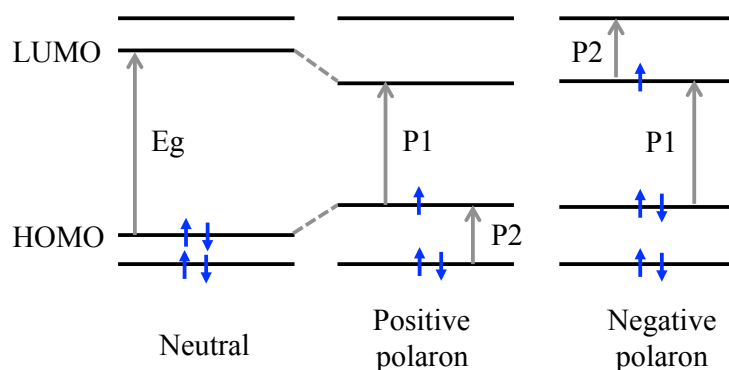


Figure 2.5: Molecular orbitals in the neutral state and in the presence of a polaron. E_g denotes the band-gap energy of the molecule whereas P1 and P2 show the polaron induced absorption.

2.3 Organic Photovoltaic Devices

2.3.1 Charge Photogeneration

An organic photovoltaic device (OPV), or solar cell, is defined as a solar cell that applies semiconducting conjugated polymers as the active components for the photo-current generation and the power conversion process. From the initial light absorption to the collection of charges at the electrode, a large number of electronic processes are involved in the operation of an OPV device; a summary is illustrated in figure 2.6. It has already been mentioned that π -electrons of conjugated polymers with small band-gaps (~ 2 eV) can be excited by absorbing a photon with an energy greater or equal to the band-gap, lying in the visible part of the spectrum. This absorption corresponds to the first optical excitation from the highest occupied molecular orbital (HOMO) to the lowest unoccupied molecular orbital (LUMO). In the case of organic semiconductors this optical excitation produces a coulombically bound electron-hole state, a Frenkel exciton.³⁶ Thus a strong electric field is required for efficient exciton dissociation to free electron/hole carriers at room temperature. Such local fields can be supplied via electron Donor(D)/Acceptor(A) interfaces (i.e interfaced between materials with sufficiently different electron affinities and ionization potentials i.e > 0.75

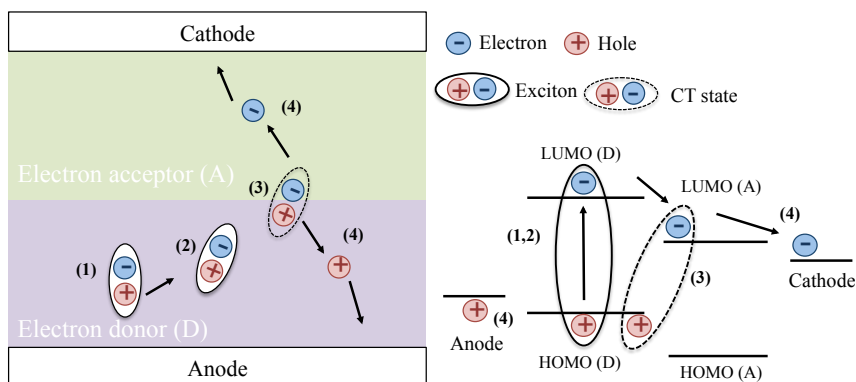


Figure 2.6: Illustration of electronic processes taking place at a Donor/Acceptor (D/A) organic photovoltaic. An Frenkel exciton is formed at the donor upon photon absorption (1) which then diffuses at the D/A heterojunction (2) where it undergoes charge transfer forming a short-lived CT state (3) and further separating into free charges collected at the electrodes (4). *Loss mechanisms are not shown.*

eV) which are commonly achieved using a bilayer planar heterojunction or a *bulk heterojunction* (BHJ).⁴⁰ In this thesis D/A heterojunctions involving a polymer-fullerene BHJ and a polymer-metal oxide bilayer planar heterojunction were used.

For photoinduced charge transfer to occur between the donor and acceptor the exciton needs to diffuse at a D/A interface within its diffusion length otherwise it decays via radiative or non-radiative pathways and its energy is lost for the power conversion. After the exciton has successfully diffused at a heterojunction it undergoes charge transfer forming an interfacial electron-hole pair known as a short-lived CT state, the precise nature of which is highly debatable.^{41,42,43} This CT state can be *bound* or *free* depending on the donor/acceptor interface properties. Vaynzof *et al.* have demonstrated that the formation of bound charge pairs (BCP) leads to increased recombination of the photogenerated charges thus hindering the performance of polymer/ZnO cells; and how the formation of BCP can be overcome but interfacial modification.⁴⁴ A model of charge separation taking into account the concepts of BCP at an exemplary organic/inorganic interface is shown in figure 2.7. Bakulin *et al.* have recently shown that efficient OPV blends inhibit the formation of bound charge pairs.⁴²

Once the charges are separated there is no preferred direction for their internal

fields thus a symmetry breaking condition is essential for further separation of the charges and avoidance of recombination; since opposite charges will alternatively diffuse towards each other by the charge carrier species concentration gradient. A driving force to promote field induced drift current is achieved at short circuit conditions by using different workfunction electrodes and it is further discussed in the following section.

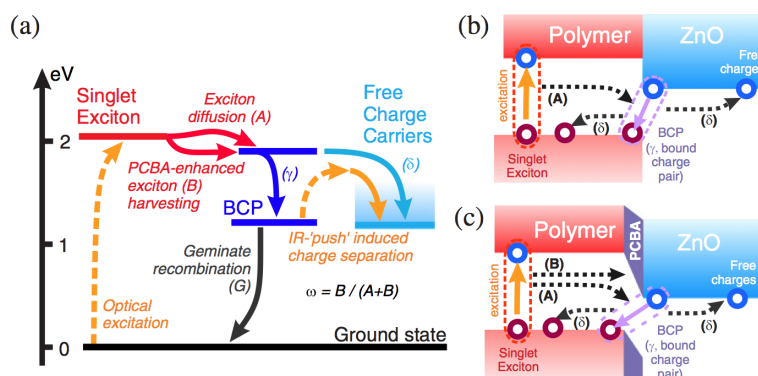


Figure 2.7: (a) The state model of charge separation, where dashed arrows represent optical transitions and γ and δ represent the relative amounts of BCP and free charges respectively. (b),(c) Corresponding band diagrams without and with interfacial modification. Reproduced from Vaynzof *et al.*⁴⁴

Inverted and hybrid architectures

The inverted and hybrid structures used for the purposes of this project, are illustrated in figure 2.8. In both architectures the organic layer is sandwiched between two inorganic layers. Other inorganic materials can be used, however here we emphasise on the use of transparent conducting oxides. The major difference between the two is the use of the n-type metal oxide layer. In the *inverted* architecture the metal oxide layer is used as an electron extraction layer (EEL) and does not contribute towards the exciton separation whereas in the *hybrid* architecture the metal oxide layer is used as the electron acceptor and the CT state is formed at the organic/metal oxide interface. The latter is the topic of discussion in chapter 5.

In both architectures the acidic PEDOT:PSS layer and the low work function

metals often used as a hole transport layer and top electrode respectively in the *standard* architecture, are substituted by transparent conductive oxides used as electron selective layers and high workfunction metals (Au,Ag), offering better ambient interface device stability. The metal oxide layer and high workfunction metal provide a more efficient barrier effect inhibiting oxygen diffusion to the organic layer whereas the oxides act as UV filters as well. As a consequence device operational stability of two weeks and continuous operation in air at 100 mWcm⁻², AM1.5G for 100h for devices without encapsulation to 80% of the initial performance has been reported.^{45,46,47}

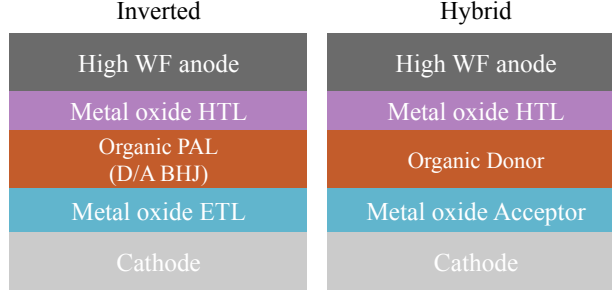


Figure 2.8: *Inverted* and *Hybrid* OPV device architectures.

2.3.2 Built-in Potential

It has been already mentioned that a driving force is required for efficient transport of the photogenerated charges from the organic photo-active layer to the collection electrodes. This driving force is a key for photovoltaic energy conversion and must be built-in to the device (i.e. maintained at short circuit conditions). Using the drift-diffusion model the current J at a point in the presence of an built-in potential V_{bi} and a carrier density gradient ∇n at short circuit conditions can be described by:

$$J = eD_e \nabla n + e\mu_e n \frac{V_{bi}}{L} \quad (2.14)$$

where n , μ_e and D_e represent the electron number density mobility and diffusion coefficient, respectively.^{48,49} L is the distance from the heterojunction to

the cathode. When the device is under illumination $n > 0$ and E_{eff} is non-zero, a net drift current will result, alternatively a net diffusion current may result depending on the gradients of the carrier densities.

A built-in electrostatic field can be established at the interface between two materials of different workfunction. An exemplary schematic diagram based on a Metal-Insulator-Metal (MIM) model⁵⁰ is shown in figure 2.9. It is evident that the resulting field will drive electrons to the right (cathode) and holes to the left (anode). This configuration can be extended to the organic photovoltaic diode configuration; assuming that there is no significant charge accumulation of intrinsic states or extrinsic defect states, and provided that the workfunctions of the anode and cathode lie between the polymers LUMO and HOMO. As a consequence the contact with the cathode presents a lower resistance path for electrons than holes, from the semiconductor to the metal and the opposite holds at the contact with the anode. This type of junction with the electrodes is an example of a *Schottky Barrier*.

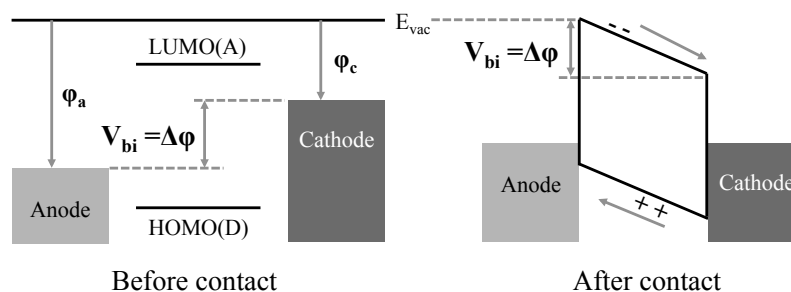


Figure 2.9: Schematic diagram of an established built-in potential, equal to the workfunction difference between the two electrodes. The arrows show the built-in field driven drift mechanism for photogenerated charges.

The above discussion on the built-in field established by the workfunction difference between the two electrodes was based on the assumption that the semiconductor interfaces involved are perfect. Both intrinsic and extrinsic defects (e.g. surface morphology or surface adsorbed impurities) tend to induce extra electronic states with energies in the band-gap which could act as charge trap states influencing the potential distribution across the interface.⁵¹ Any ac-

cumulation of charges at the interface will create a band bending, which leads to a reduction of the electric field in the bulk of the device.⁵² In the case of an induced interfacial dipole V_{int} contributing to the change in workfunctions, the built-in field will be affected according to equation 2.15 and a reduced (screened) effective field will be measured instead.^{53,48}

$$\Delta\phi = q(V_{bi} + V_{int}) \quad (2.15)$$

2.3.3 Open-circuit Voltage

The open-circuit voltage V_{OC} of a solar cell originates from the difference between the quasi-Fermi levels in the electron and hole extracting regions of the device. It has been demonstrated that for a photodiode, based on a single layer of conjugated polymer, the V_{OC} scales with the workfunction difference between the electrodes; this is in agreement with the MIM model.⁵⁰ In bilayer devices made by electron and hole accepting organic semiconductors, the V_{OC} was also found to scale linearly with the work function difference, however, with an additional contribution depending on the light intensity. In polymer/fullerene BHJ solar cells V_{OC} is found to scale with the difference between the HOMO energy of the donor and the LUMO energy of the fullerene acceptor. This scaling of the V_{OC} with HOMO(D)-LUMO(A) is valid provided that the quality of the electrical contact between the organic and the electrodes is not limiting.⁵⁴ In the case of *non-ohmic* contact small dependence on the contacts workfunction was explained by pinning of the electrode Fermi level to the reduction potential of the organic semiconductor. In the case of *ohmic* contact V_{OC} will be limited by voltage losses at the contacts due to band-bending. Mihailitchi *et al.* have expressed this loss by the following simple equation:

$$q(V_{OC} + \Delta V_{bb}) = HOMO(D) - LUMO(A), \quad (2.16)$$

where ΔV_{bb} is the sum of the voltage losses at each contact due to band-bending.⁵⁴

It is often the case that the theoretical maximum value for V_{OC} is not achieved, even when the contact with the electrodes is efficient. Losses in the value of V_{OC} have been correlated to non-radiative recombination losses at the donor/acceptor

interface.^{55,56} In order to correlate experimentally measured V_{OC} to these losses manifesting as current losses the following equation is commonly used:

$$V_{OC} = \frac{nkT}{q} \ln \left(\frac{J_{SC}}{J_0} + 1 \right), \quad (2.17)$$

where n is the diode ideality factor, J_{SC} and J_0 represent the short-circuit and dark saturation current respectively, q is the electron charge, k the Boltzmann constant and T represents temperature. The above equation is derived from the ideal-diode equation for current injection and it is assuming that at open circuit voltage the injected current equals the photogenerated current J_{SC} , whereas n accounts for deviations from the ideal diode equation. Typically, J_0 is determined by injection and recombination mechanisms of the free carriers.⁵⁷

2.3.4 Stability and Degradation

The primary focus of this thesis was to investigate organic photovoltaic systems involving metal oxide layers, and in specific ZnO. The motivation behind OPV systems involving metal oxides comes from the remarkable improvement in device stability performance when metal oxides are incorporated in the device structure. The numerous benefits of the inverted and hybrid architectures in comparison with the standard architecture have already been discussed, however a different range of instabilities has been identified with the use of solution processed ZnO and TiO₂. Here we present degradation mechanisms and device instabilities mentioned in literature which are relevant with this project.

2.3.4.1 Active Layer Photo-oxidation

It is well known that the organic semiconductor active layer in an organic photovoltaic is susceptible to photooxidation. Many conjugated macromolecules are particularly vulnerable towards molecular oxygen but only when irradiated. Irradiation of P3HT in ambient air was shown to provoke a continuous decrease in the visible band absorption intensity of P3HT centred at 520nm.^{58,59} As a result the polymer is said to be photo-bleached, however the exact mechanism behind this degradation is debatable. A mechanism which involves the radical

oxidation of the *n-hexyl* side chains and the subsequent oxidation of the sulfur atom of the thiophene ring has been proposed to account for the breaking of the macromolecule backbone and loss of π -conjugation.

Degradation of similar polymers has been correlated to the ability of a particular carbon in the polymer chain to be oxidised which can be described in terms of the energy of the bonds being broken and the stability of the radical formed.⁶⁰ In the past few years, two mechanisms have been identified as being mainly responsible for organic semiconductor degradation in the presence of oxygen: (i) oxygen sensitization, mediated by long lived triplet states with an energy level higher than the differential energy between the oxygen singlet state and its ground triplet state; and (ii) electron transfer from the photoexcited polymer to molecular oxygen, generating the superoxide, O_2^- , which is a very reactive anionic radical.^{61,62,63}

Recently, it has been realised that the HOMO level positioning of a polymer is not a sufficient criterion to conclude on its photochemical stability and that identifying the correlation between individual polymer structure and polymer photochemical stability can be the key towards the design of more stable materials.^{64,65,66} On the other hand the role of interfacial dynamics in the stability of organic photovoltaic devices has been proven to be critical. In fact, degradation of an individual layer can be substantially affected when in contact with another layer. For example it has been reported before that device degradation is strongly inhibited when the active polymer is blended with the fullerene acceptor due to the radical scavenging properties of the fullerene and single exciton quenching mechanisms. Soon *et al.*⁶⁷ and Distler *et al.*⁶³ on the other hand identified a destabilizing role of the fullerene, in PTB7:PCBM and PCPDTBT:PCBM blends respectively; and the significance of the electron affinity of the electron acceptor is under debate. A model suggesting the involvement of the polymer donor triplet state in the photo-degradation has been suggested whereas Grancini *et al.* have demonstrated that such a triplet state is not involved in the photo-degradation kinetics of the photovoltaic blend when exposed to ambient conditions. Instead the interfacial CT state is involved in the generation of reacting and harmful species such as superoxide, upon electron transfer to contaminants such as OH^- , OOH^- and $O_2(H_2O)_n$.⁶⁸ Schematic diagrams suggested by the authors of the relevant

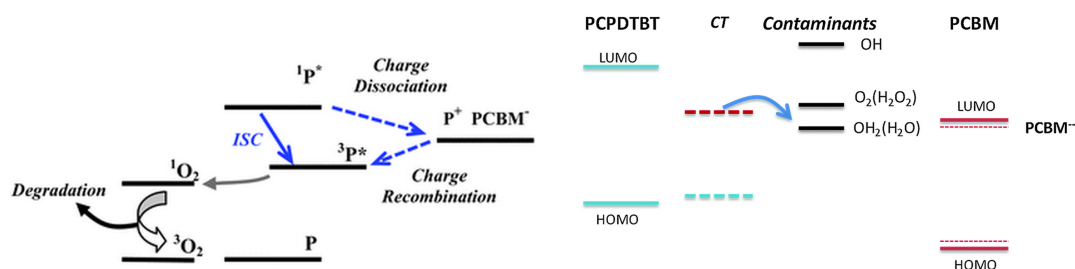


Figure 2.10: Suggested degradation mechanisms involving the polymer triplet state (left) and the interfacial CT state (right); figures adapted from Soon *et al*⁶⁷ and Grancini *et al*⁶⁸ respectively.

papers are summarised in figure 2.10. Beyond air degradation it has to be noted that chemical instabilities such as chain scission or cross-linking, can still occur with UV-Visible light exposure in inert atmosphere.

2.3.4.2 UV Light Soaking Step

The need of a UV light soaking step before achieving good photovoltaic performance is one of the most common instabilities associated with the use of solution processed ZnO as electron transport layer in inverted organic solar cells.^{69,70,71,72} The resulting improvement in device performance is non-permanent and its origin not fully understood.^{73,74} The initially poor s - shaped IV characteristics of the device gradually changes to normal diode-like IV characteristics as ZnO is photo-activated. This has been attributed to an increase in the ZnO conductance due to surface oxygen desorption with UV light; based on a chemical mechanism proposed by Verbakel *et al.*⁷⁵ and elaborated by Krebs *et al.*⁷⁶ (see section 2.1.3). Under UV irradiation the ZnO layer becomes doped by free electrons. Manor *et al.* proposed that this improvement is a result of better selectivity properties of ZnO with additional doping, since the minority carriers number density in the layer drops with the Fermi level rising, and a more efficient electron transport through the PCBM-ZnO contact.⁷⁷ However, under concentrate sunlight experiments, Tromholt *et al.* demonstrated degradation of a P3HT:PCBM/ZnO device and loss of the diode character as a result of significant shunting, which was attributed to tunnelling of holes from P3HT to ZnO at extremely high *n*-doping

levels of ZnO.⁷⁸

Although it is well known that the lifetime of devices without any EEL is very short as opposed to devices with a ZnO EEL the question whether such instabilities of the ZnO surface properties could have any effect on the long-term air degradation of the device has yet to be addressed.

2.4 Organic Field Effect Transistors

In chapter 6 we use the Charge Accumulation Spectroscopy technique⁷⁹ to detect the polaron induced absorption in PTB7 organic field effect transistors (OFETs) and compare it to charge induced absorption obtained for PTB7:PCBM inverted organic solar cells. Here we present the basic principles behind organic field effect transistors and describe briefly the device operation.

A transistor is a three terminal electronic switch for which a voltage applied to one pair of terminals (V_{gs} for gate-source terminals and V_{ds} for drain-source terminals), changes the current through the other pair of terminals. A typical bottom-contact, top-gate transistor is shown in figure 2.11 and consists of three electrodes (gate, source and drain), a semiconductor layer and a dielectric. The semiconductor layer permits for current flow through the source-drain channel whereas the insulating dielectric layer isolates the gate electrode from the semiconductor. V_{gs} controls the conductivity of the channel in the semiconductor between the source and drain electrodes. Without an applied V_{gs} , the current is determined by the intrinsic bulk conductivity of the semiconductor. An applied V_{gs} can induce charges at the interface to form a highly conductive accumulation layer and lead to an increased measured current. For a unipolar transistor (either n-type or p-type semiconductor) an accumulation layer or the majority charge carriers (electrons or holes) will form when the right gate voltage is applied (positive or negative). Ambipolar transistors on the other hand are capable of both p-type and n-type conductivity and respective accumulation layers will form in both positive and negative gate voltage bias.

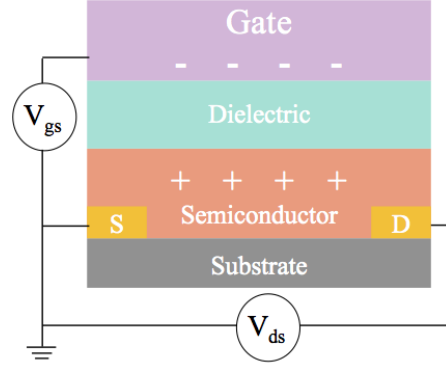


Figure 2.11: Device architecture of a bottom-contact top-gate field-effect transistor, where V_{gs} and V_{ds} is the voltage applied respectively to the gate and drain while the source is grounded. Negative and positive signs show an example of charge accumulation in a p-type semiconductor for a negative V_{gs} .

References

- [1] Nomura, K., , Ohta, H., Takagi, A., Kamiya, T., Hirano, M., and Hosono, H. (2004) *Nature*, **432**, 488. 6, 10
- [2] Kamiya, T., Nomura, K., and Hosono, H. (2009) *J. Display Technol.*, **5**, 273. xi, 7, 10
- [3] Kamiya, T. and Hosono, H. (2010) *NPG Asia Mater.*, **2**, 15. 8, 10
- [4] Oba, F., Nishitani, S., Isotani, S., and Adachi, H. (2001) *J. Appl. Phys.*, **90**, 825. 8
- [5] Kamiya, T., Nomura, K., Hirano, M., and Hosono, H. (2008) *Phys. Stat. Solidi (c)*, **5**, 3098. 8, 10
- [6] Morkoc, H. and Ozgur, U. (2009) *Zinc Oxide: Fundamentals, Materials and Device Technology*, Wiley-VCH, Weinheim. 9
- [7] Yadav, M.K., Ghosh, M., Biswas, R., Raychaudhuri, A.K., and Mookerjee, A. (2007) *Phys. Rev. B*, **76**, 195 450. 10
- [8] Janotti, A. and Van de Walle, C. (2009) *Rep. Prog. Phys.*, **72**, 126 501. 10

-
- [9] Hoye, R.L.Z., Ehrler, B., Böhm, M.L., Rojas, D.M., Altamimi, R.M., Alyamani, A.Y., Vaynzof, Y., Sadhanala, A., Ercolano, G., Greenham, N.C., Friend, R.H., MacManus-Driscoll, J.L., and Musselman, K.P. (2014) *Adv. Energy Mater.*, **4**, 1301544. 10
 - [10] Banger, K.K., Yamashita, Y., Mori, K., Peterson, R.L., Leedham, T., Rickard, J., and Sirringhaus, H. (2011) *Nature Materials*, **10**, 45–50. 10, 17
 - [11] Drude, P. (1900) *Ann. Phys.*, **3**, 369. 11
 - [12] Burstein, E. (1954) *Phys. Rev.*, **93**, 632. 11
 - [13] Moss, T. (1961) *Optical Properties of Semiconductors*, Academic, New York. 11
 - [14] Hartnagel, H., Dawar, A., Jain, A., and Jagadish, C. (1995) *Semiconducting Transparent Thin Films*, Institute of Physics Publishing. 12
 - [15] Baikie, I., Vanderwerf, K., Oerbekke, H., Broeze, J., and Vansilfhout, A. (1989) *Rev. Sci. Instrum.*, **60**, 930. 13
 - [16] Ellmer, K., Klein, A., and Rech, B. (2007) *Transparent Conductive Zinc Oxide: Basics and Applications in Thin Film Solar Cells*, Springer. 13
 - [17] Winget, P., Schirra, L.K., Cornil, D., Li, H., Coropceanu, V., Ndione, P.F., Sigdel, A.K., Ginley, D.S., Berry, J.J., Shim, J., Kim, H., Kippelen, B., Brédas, J.L., and Monti, O.L.A. (2014) *Adv. Mater.*, **26**, 4711. 13
 - [18] Dagan, S., Amirav, A., and Fuju, T. (1995) *Int. J. Mass Spectrom. Ion Processes*, **151**, 159. 13
 - [19] Ton-That, C., Phillips, M., Foley, M., Moody, S., and Stampfl, A. (2008) *Appl. Phys. Lett.*, **92**, 261916. 14
 - [20] Sharma, P., Pandey, A., Zolnierkiewicz, G., Guskos, N., and Rudowicz, C. (2009) *J. Appl. Phys.*, **106**, 094314. 14

REFERENCES

- [21] Verbakel, F., Meskers, S.C.J., and Janssen, R.A.J. (2006) *Applied Physics Letters*, **89**, 102 103. xi, 15
- [22] Mollow, E. (1956) *Proceedings of the conference on photoconductivity*, John Wiley and Sons, Inc., New York. 15
- [23] Reemts, J. and Kittel, A. (2007) *J. Appl. Phys.*, **101**. 16
- [24] Moore, J. and Thompson, C. (2013) *Sensors*, **13**, 9921. 16
- [25] Collins, R. and Thomas, D. (1958) *Phys. Rev.*, **112**, 388. 17
- [26] Bao, J., Shalish, I., Su, Z., Gurwitz, R., Capasso, F., Wang, X., and Ren, Z. (2011) *Nanoscale Research Letters*, **6**, 404. 17
- [27] Mosbacker, H., Strzhemechny, Y., White, B., Smith, P., Look, D., Reynolds, D., Litton, C., and Brillson, L. (2005) *Appl. Phys. Lett.*, **87**, 012 102. 17
- [28] Janotti, A. and Van de Walle, C. (2005) *Appl. Phys. Lett.*, **87**, 228. 17
- [29] Zhao, Z., Teki, R., Koratkar, N., Efstathiadis, H., and Haldar, P. (2010) *Appl. Surf. Sci.*, **256**, 6053. 17
- [30] Vaynzof, Y., Kabra, D., Zhao, L., Chua, L.L., Steiner, U., and Friend, R.H. (2011) *ACS Nano*, **5**, 329. 17
- [31] Sun, Y., Seo, J.H., Takacs, C., Seifert, J., and Heeger, A.J. (2011) *Adv. Mater.*, **23**, 1679. 17
- [32] Saeed, T. and O'Brien, P. (1995) *Thin Solid Films*, **271**, 35. 17
- [33] Brinker, C. and Scherer, G. (1990) *Sol-Gel Science: The Physics and Chemistry of Sol-Gel Processing*, Academic, New York. 17
- [34] Gwinner, M., Vaynzof, Y., Banger, K.K., Ho, P.K.H., Friend, R.H., and Sirringhaus, H. (2010) *Advanced Functional Materials*, **20** (3457). 17
- [35] Barford, W. (2005) *Electronic and Optical Properties of Conjugated Polymers*, Oxford University Press. 19

-
- [36] Liang, W. (1970) *Physics Education*, **5**, 226. 21, 23
 - [37] Wannier, G. (1937) *Phys. Rev.*, **52**, 191. 21
 - [38] Veldman, D., Meskers, S.C.J., and Janssen, R.A.J. (2009) *Adv. Funct. Mater.*, **19**, 1939. 21
 - [39] Pope, M. and Swenberg, C. (1955) *Electronic Processes in Organic Crystals*, Clarendon Press, Oxford, UK. 22
 - [40] Gunes, S., Neugebauer, H., and Sariciftci, N.S. (2007) *Chem. Rev.*, **107**, 1324. 24
 - [41] Grancini, G., Maiuri, M., Fazzi, D., Petrozza, A., Egelhaaf, H.J., Brida, D., Cerullo, G., and Lanzani, G. (2012) *Nature Materials*, **11**, 1. 24
 - [42] Bakulin, A., Rao, A., Pavelyev, V., van Loosdrecht, P.H.M., Pshenichnikov, M.S., Niedzialek, D., Cornil, J., Beljonne, D., and Friend, R.H. (2012) *Science*, **335**, 1340. 24
 - [43] Jailaubekov, A.E., Willard, A., Tritsch, J., Chan, W.L., Sai, N., Gearba, R., Kaake, L., Williams, K., Leung, K., Rossky, P.J., and Zhu, X.Y. (2013) *Nature Materials*, **12**, 66. 24
 - [44] Vaynzof, Y., Bakulin, A., Gelinas, S., and Friend, R.H. (2012) *Phys. Rev. Lett.*, **108**, 246 605. xii, 24, 25
 - [45] Sahin, Y., Alem, S., de Bettignies, R., and Nunzi, J. (2005) *Thin Solid Films*, **476**, 340. 26
 - [46] Lee, K., Kim, J., Parks, S., Kim, S., Cho, S., and Heeger, A.J. (2007) *Adv. Mater.*, **19**, 2445. 26
 - [47] Fan, B., Hany, R., Moser, J., and Nuesch, F. (2008) *Org. Electron.*, **9**, 85. 26
 - [48] Nelson, J. (2003) *The Physics of Solar Cells*, Imperial College Press, London. 26, 28

REFERENCES

- [49] Ramsdale, C., Barker, J.A., Arias, A.C., MacKenzie, J., Friend, R.H., and Greenham, N.C. (2002) *J. Appl. Phys.*, **92**, 4266. 26
- [50] Liu, J., Shi, Y., and Yang, Y. (2001) *Adv. Funct. Mater.*, **11**, 420. 27, 28
- [51] Bardeen, J. (1947) *Phys. Rev.*, **71**, 717. 27
- [52] Malliaras, G.G., Salem, J.R., Brock, P.J., and Scott, J.C. (1998) *J. Appl. Phys.*, **84**, 1583. 28
- [53] Fonash, S. (2010) *Solar Cell Device Physics*, Academic, New York, 2nd edn.. 28
- [54] Mihailetchi, V.D., Blom, P., Hummelen, J.C., and Rispens, M.T. (2003) *J. Appl. Phys.*, **94**, 6849. 28
- [55] Vandewal, K., Tvingstedt, K., Gadisa, A., Inganäs, O., and Manca, J. (2009) *Nat. Mater.*, **8**, 904. 29
- [56] Benson-Smith, J., Goris, L., Vandewal, K., Haenen, K., Manca, J., Vanderzande, D., Bradley, D.D.C., and Nelson, J. (2007) *Adv. Funct. Mater.*, **17**, 451. 29
- [57] Braun, D. (2003) *J. Polym. Sci. B Polym. Phys.*, **41**, 2622. 29
- [58] Manceau, M., Rivaton, A., Gardette, J.L., Guillerez, S., and Lemaitre, N. (2009) *Polym. Degrad. Stab.*, **94**, 898. 29
- [59] Hintz, H., Egelhaaf, H.J., Peisert, H., and Chasse, T. (2010) *Polym. Degrad. Stab.*, **95**, 818. 29
- [60] Posada, F., Philippart, J.L., Kappler, P., and Gardette, J.L. (1995) *Polym. Degrad. Stab.*, **50**, 141. 30
- [61] Distler, A., Kutka, P., Sauermann, T., Egelhaaf, H.J., Guldi, D., Di Nuzzo, D., Meskers, S., and Janssen, R.A.J. (2012) *Chem. Mater.*, **24**, 4397. 30
- [62] Hoke, E., Sachs-Quintana, I.T., Lloyd, M., Kauvar, I., Mateker, W., Nardes, A., Peters, C., Kopidakis, N., and McGehee, M.D. (2012) *Adv. Energy Mater.*, **2**, 1351. 30

-
- [63] Aguirrea, A., Meskers, S.C.J., Janssen, R.A.J., and Egelhaaf, H.J. (2011) *Organic Electronics*, **12**, 1657. 30
- [64] Xiaohan, Y., Tong, X., Li, B., Wang, C., and Liu, H. (2011) *J. Polym. Sci. A Polym. Chem.*, **49**, 2969. 30
- [65] Manceau, M., Helgesen, M., and Krebs, F.C. (2010) *Polym. Degrad. Stab.*, **95**, 2666. 30
- [66] Manceau, M., Bundgaard, E., Carle, J., Hagemann, O., Helgesen, M., Sondergaard, R., Jorgensen, M., and Krebs, F.C. (2011) *J. Mater. Chem.*, **21**, 4132. 30
- [67] Soon, Y.W., Cho, H., Low, J., Bronstein, H., McCulloch, I., and Durrant, J.R. (2013) *Chem. Commun.*, **49**, 1291–1293. xii, 30, 31
- [68] Grancini, G., De Bastiani, M., Martino, N., Fazzi, D., Egelhaaf, H.J., Sauermann, T., Antognazza, M., Lanzani, G., Caironi, M., Franco, L., and Petrozza, A. (2014) *Phys. Chem. Chem. Phys.*, **16**, 8294. xii, 30, 31
- [69] Gilot, J., Wienk, M.M., and Janssen, R.A.J. (2007) *Applied Physics Letters*, **90**, 143512. 31
- [70] Steim, R., Choulis, S.A., Schilinsky, P., and Brabec, C.J. (2008) *Applied Physics Letters*, **92**, 093303. 31
- [71] Kim, C.S., Lee, S.S., Gomez, E.D., B., K.J., and Loo, Y.L. (2009) *Applied Physics Letters*, **94**, 113302. 31
- [72] Sista, S., Park, M.H., Hong, Z., Wu, Y., Hou, J., Kwan, W.L., Li, G., and Yang, Y. (2010) *Advanced Materials*, **22**, 380. 31
- [73] Schmidt, H., Zilberberg, K., Schmale, S., Flügge, H., Riedl, T., and Kowalsky, W. (2010) *Applied Physics Letters*, **96**, 243305. 31
- [74] Kim, J., Kim, G., Choi, Y., Lee, J., Heum Park, S., and Lee, K. (2012) *Journal of Applied Physics*, **111**, 114511. 31

REFERENCES

- [75] Verbakel, F., Meskers, S.C.J., and Janssen, R.A.J. (2007) *Journal of Applied Physics*, **102**, 083 701. 31
- [76] Krebs, F.C., Tromholt, T., and Jørgensen, M. (2010) *Nanoscale*, **2**, 873. 31
- [77] Manor, A., Katz, E.A., Tromholt, T., and Krebs, F.C. (2011) *Advanced Energy Materials*, **1**, 836. 31
- [78] Tromholt, T., Manor, A., Katz, E.A., and Krebs, F.C. (2011) *Nanotechnology*, **22**, 225 401. 32
- [79] Di Pietro, R. (2012) *Charge Accumulation Spectroscopy of Organic Semiconductors*, Ph.D. thesis, University of Cambridge. 32

Chapter 3

Experimental Methods

This chapter aims to give a detailed description of the fabrication steps followed and characterisation methods exploited for all samples including devices that were used in this project. Results for the work carried out as described in this section are presented and discussed in the following chapters.

3.1 Materials

In this chapter we summarise all materials used for the purposes of this project. Materials include: photo-active organic semiconductors used as electron donors (p-type polymers P3HT and PTB7) and electron acceptors (fullerenes PC₆₀BM, PC₇₀BM, PCBA), conducting metal oxides used as electron transport/acceptor layers (ZnO, ZnSrO and ZnBaO), WO₃ as a hole transport layer and Ag and ITO as electrodes.

3.1.1 *P*-type Polymers

Poly(3-hexylthiophene)

Poly(3-hexylthiophene-2,5-diyl) commonly known as P3HT is a p-type semiconductor (figure 3.1) that is optimised for OPV applications. P3HT was introduced as an improved alternative to polyphenylene vinylene (PPV) with higher (hole) mobility and wider absorption. Regioregular P3HT self-organises in a lamella structure with two-dimensional conjugated sheets formed by inter-chain stacking

allowing for efficient inter-chain transport of charge carriers¹ and (hole) mobilities as high as $10^{-1} \text{ cm}^2\text{V}^{-1}\text{s}^{-1}$.^{2,3} The bandgap of P3HT is around 1.9eV limiting the absorbance below a wavelength of 650 nm. Due to the low excitonic diffusion length of organic semiconductors ($\sim 10 \text{ nm}$) donor and acceptor phases are dispersed throughout the active layer of an OPV in a bulk heterojunction (BHJ).⁴ P3HT is often combined with an n-type acceptor, such as a fullerene derivative, for use as the photoactive component. A strong dependence on thermal annealing is observed for the P3HT:PC₆₀BM system. The process of thermal annealing causes P3HT to crystallise which induces a thermodynamically driven rearrangement of donor and acceptor phases resulting in an improved conduction of charge carriers and improved absorption profile.⁵ Thermal annealing has different effects associated with the fullerene derivative and are mentioned in section 3.1.2. Performance efficiencies up to 4 % (NREL Certified) can be achieved for an optimised P3HT:PC₆₀BM solar cell.

For the purposes of this project P3HT was supplied by Merck Chemicals LTD ($M_w = 54200 \text{ g mol}^{-1}$, $M_n = 23600 \text{ g mol}^{-1}$, $RR \sim 94.2 \%$). P3HT:PC₆₀BM was used as the photoactive layer in a model system to study the dependence of inverted organic solar cell device performance and stability on metal oxide electron extraction layers (see chapter 4). P3HT:PC₆₀BM was chosen since it has been extensively characterised and it is well understood both from the structural and electrical point of view. A blend of both materials is deposited to form a bulk heterojunction. It has been previously reported that when this blend is deposited on an ITO covered glass substrate via spin-coating (which is the case here) PC₆₀BM tends to form a few nanometers thin layer on the ITO interface before the composition of the film is even in the bulk of the film.

Poly-thienothiophene-benzodithiophene

Poly-thienothiophene-benzodithiophene (PTB) polymers is a class of low bandgap polymers base on alternating ester substituted thieno[3,4-*b*]thiophene (TT) and benzodithiophene (BDT) monomer units attached with different side groups.^{6,7} As a result of the stabilization of the quinoidal structure from TT these polymers have low bandgaps of about 1.6 eV, showing efficient absorption around the region with the highest photon flux of the solar spectrum (700 nm). The rigid backbone

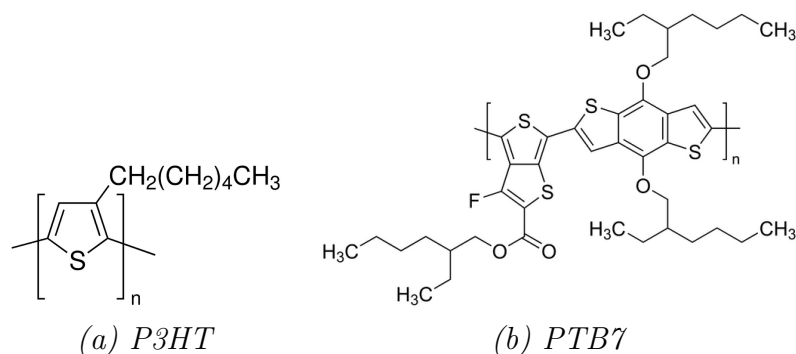


Figure 3.1: Molecular structures of (a) P3HT and (b) PTB7 p-type polymers

results in a good hole mobility and side chains of ester and BDT allow for good solubility in organic solutions and good miscibility with a fulleride acceptor.⁸ In addition the introduction of fluorine into the TT results to a low lying HOMO energy level and an enhanced V_{OC} .⁷ The polymer alignment is found to be in the form of a stack on the substrate in the face-down confirmation favouring charge transport.⁹ All of these advantages make the BHJ of PTB polymer/fullerene one of the most highly efficient organic solar cell systems to date.

The derivative Poly[[4,8-bis[(2-ethylhexyl)oxy]benzo[1,2-b:4,5-b'] dithiophene -2,6-diyl][3-fluoro-2-[(2-ethylhexyl)carbonyl]thieno[3,4-b]thiophenediyl]] commonly known as PTB7 (see figure 3.1) exhibits excellent photovoltaic effect when used in PTB7:PC₇₀BM systems reaching certified efficiencies of up to $\sim 9\%$.^{8,10}

The HOMO and LUMO energy levels of PTB7 were determined by cyclic voltammetry at -5.15 eV and -3.31 eV respectively. However PTB7 has been reported to be relatively unstable with regards to photostability. This instability has been assigned with singlet oxygen generation from triplet excitons.¹¹ For the purposes of this project PTB7 was supplied by *1-Material Inc.* and was used as the semiconductor in organic field effect transistors to detect the PTB7 polaron absorption; as well as in PTB7:PC₇₀BM inverted organic solar cells to study the dependence of device performance and stability on different bias conditions (chapters 6 and 7).

3.1.2 Fullerene Derivatives

Fullerenes are spherical, all carbon structures consisting of 12 pentagons which are completely surrounded by n hexagons (see figure 3.2 for molecular structures of discussed fullerene derivatives). One of the most famous applications of fullerenes is found as electron acceptors in organic solar cells due to their excellent electron acceptor functionality and high electron mobilities. The origin of the high electron affinity of fullerenes is ascribed to the reduced strain energy of the carbon cluster with the capture of an electron. Negatively charged carbon atoms exhibit more sp^3 character and hence longer bond lengths to their neighbours resulting in lower strain energy.¹²

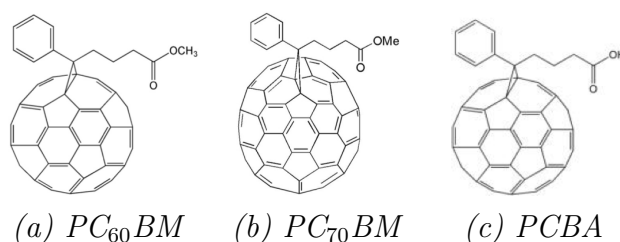


Figure 3.2: Molecular structures of fullerene derivatives

PC₆₀BM, PC₇₀BM and PCBA

C_{60} or Buckminsterfullerene is the smallest stable fullerene whereas phenyl- C_{61} -butyric acid methyl ester ($PC_{60}BM$) and phenyl- C_{71} -butyric acid methyl ester ($PC_{70}BM$) are high soluble C_{60} derivatives allowing for compatibility with the BHJ processing for OPVs. The major improvement of $PC_{70}BM$ compared to $PC_{60}BM$ is having much larger absorption of light in the visible range. In some cases fullerene derivatives have been used for work-function modification of a substrate. For example the self assembled monolayer phenyl- C_{61} -butyric acid ($PCBA$) has been shown to increase a ZnO substrate work-function from 3.6 eV to 4.1eV due to an interfacial dipole moment pointing away from ZnO.¹³ The molecular structures for $PC_{60}BM$, $PC_{70}BM$ and $PCBA$ are shown in figure 3.2. For the purposes of this project all fullerene derivatives were provided from “Solenne BV” (purity > 99 %).

3.1.3 ZnO, ZnSrO and ZnBaO

ZnO has been widely used as electron extraction layer (EEL) in inverted organic photovoltaics due to its beneficial properties such as high conductivity and transparency, as well as the simplicity and low cost of solution processing. Our group has developed a low-temperature, solution-processing approach to fabricate mixed metal oxides based on sol-gel processing of metal alkoxide precursors (see section 2.1.4 for more detail).¹⁴ This technique was used before to produce highly performing ZnO as electron injector in organic ambipolar light emitting field effect transistors¹⁵ as well as high performance mixed metal oxide IZO and IGZO thin film transistors (TFTs).¹⁴

For the purposes of this project we have fabricated two novel ternary oxides, zinc strontium oxide (ZnSrO) and zinc barium oxide (ZnBaO) by incorporating the alkaline earth metals strontium or barium into a ZnO film in a one step sol-gel process using metal alkoxide molecular precursors shown in figure 3.3 (provided by “Multivalen Ltd”). Zinc-bis methoxyethoxide, $Zn(OCH_2CH_2OCH_3)_2$ was used for ZnO deposition and barium or strontium isopropoxide, $Ba(OC_3H_7)_2$ or $Sr(OC_3H_7)_2$ for doping. This is done by simple spin coating of a precursor solution or a mixture of two different precursor solutions and annealing the resulting films at $300^{\circ}C$ to decompose the organic constituents and densify the film.

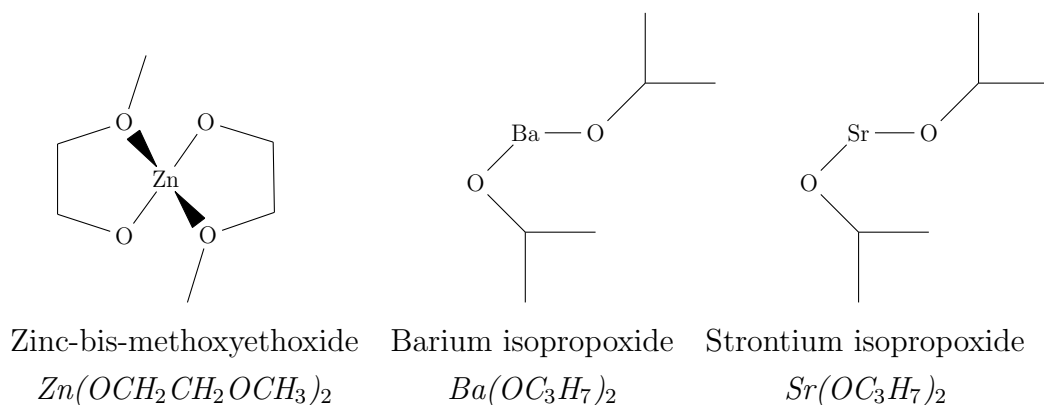


Figure 3.3: Molecular alkoxide precursors

Our choice of these alkaline earth metals is inspired by barium and strontium oxides having wide band gaps (4.0 - 6.5 eV), binary oxidation states (+2) and,

in particular, a higher Gibbs energy of oxidation than gallium. Based on the findings that the incorporation of gallium can suppress the formation of oxygen deficiencies due to the fact that GaO bonds are much stronger than ZnO bonds (see discussion in section 2.1.1.2), we believe that the tight oxygen binding to Ba and Sr will too suppress the formation of oxygen vacancies in the film and might impart a higher operational stability on the charge extraction layers.

3.1.4 Tungsten Trioxide

Transition metal oxides with exceptionally deep lying electronic states such as V_2O_5 , WO_3 and MoO_3 are widely used in the field of organic electronics to realise p-type doping of organic materials and assist hole injection for OLED's, OPVs and OFET's.^{16,17,18} Several research groups have reported a large improvement in performance and stability of OPVs with the incorporation of a thin layer of WO_3 or MoO_3 ^{19,20,21}. It has been claimed that MoO_3 leads to device improvement by preventing electrons from leaking to the hole-collecting contact, based on the interpretation of a electron affinity (EA) and ionisation energies (IE) estimated at 2.7 eV and 5.3 eV respectively.^{16,22} However, more recently ultraviolet and inverse photoemission spectroscopy investigations revealed that the actual values EA and IE are actually much higher (6.7 eV and 9.7 eV respectively) showing clearly that the gap and conduction band position of MoO_3 do not provide an electron barrier as assumed.^{23,24} Therefore the improvement in device performances was attributed to p-type doping of the OSC by MoO_3 . Measurements on WO_3 and V_2O_5 exhibit very similar deep lying electronic states pointing out that the same mechanism takes place as in the case of MoO_3 .¹⁷ All three oxide can be easily deposited via thermal evaporation. In this project WO_3 was preferred after device optimisation.

3.2 Thin Film Fabrication

OPV, OFET devices, single layer (SL) and bi-layer samples (BL) were deposited on a variety of substrates suitable for each measurement. All substrate types were cleaned by sonicating in di-ionised water, acetone and iso-propanol for 10

3.2 Thin Film Fabrication

minutes each, followed by an oxygen plasma step at power of 250 W for 10 minutes just before use. The information on which substrate was used for each sample application can be found summarised in table 3.1.

Table 3.1: Sample substrates and application

Substrate	Features	Sample	Application
Corning 1737F Glass	Low alkali boro-aluminosilicate Flat	SL/BL two-terminal device OFET	IV $\Delta T/T$ XRD
Spectrosil 2000 fused silica	Transmittance >90% 180nm-2000nm	SL/BL OPV	IV $\Delta T/T$
Native oxide wafer SiO ₂ /Si	Conductive	SL/BL	XPS UPS SEM AFM
ITO coated soda lime glass	$15\Omega\text{cm}^{-2}$ sheet resistance	OPV	IV UV-Vis EA PPP

3.2.1 Organic Layer

Photo-active layer

All organic materials were received in powder form and were processed and stored in inert glove-box atmosphere at all times (O_2 , H_2O < 10 ppm). Thin films of organic semiconductors were deposited by means of spin-coating from solution.²⁵ All solutions were prepared using anhydrous solvents and were left stirring at 70°C for at least 24 hours prior spin-coating, using a motor activated hotplate. In all cases the solution was filtered through a 0.2 μm pore size PTFE, hydrophylic filter and spin-coated at a speed of 700 rpm for a time of 180 seconds to form a thin uniform film. The film is then annealed on a hotplate inside the glovebox to get rid of the solvent and, depending on the polymer, to change its morphology. Solutions were used within 2-days after preparation unless otherwise stated. For

the deposition of organic photoactive layers used for organic and hybrid devices we followed the fabrication procedures reported in literature for optimised device performance. For the deposition of thin film of single organic layers for the purposes of spectroscopy or conductivity measurements we followed an empirical recipe so that we obtained the required thickness of ~ 10 nm. P3HT:PC₆₀BM (1:1 by weight) was spin-coated from a 1,2-dichlorobenzene (DCB) solution (40 total gL⁻¹) to give ~ 200 nm films.^{26,27} PTB7:PC₇₀BM (1:1.5 by weight) was spin-coated from a chlorobenzene (CB) solution (35 total gL⁻¹) with 3 vol% 1,8-diiodooctane as co-solvent to give films ~ 100 nm thick.²⁸ P3HT for the purposes of P3HT/ZnO hybrid devices was spin-coated from a CB solution (20 gL⁻¹) to give ~ 200 nm films.^{29,13} A summary of the corresponding solutions and annealing conditions used for different organic films can be found in table 3.2. The thickness values for organic materials were obtained by means of thickness profilometry.

Table 3.2: Organic solutions and processing conditions

Material	Solvent	Post treatment
P3HT:PC ₆₀ BM	(1:1) 40 gL ⁻¹ in DCB	10 minutes at 130 ⁰ C
PTB7:PC ₇₀ BM	(1:1.5) 35 gL ⁻¹ in CB+DIO	overnight at 80 ⁰ C
P3HT (Hybrid PV)	20 gL ⁻¹ in CB	10 minutes at 130 ⁰ C
PTB7, PC ₆₀ BM, PC ₇₀ BM	10 gL ⁻¹ in CB	overnight at 80 ⁰ C

Interface modification PCBA The substrates were modified with a self-assembled monolayer (SAM) of PCBA (Solenne) by immersing the samples for 30 minutes into an anhydrous CB solution 0.1 g/l of the SAM. The samples were then flushed three times with CB to remove excess PCBA. The obtained SAM thickness was estimated by means of X-ray photoemission spectroscopy to be ~ 11 Å which is in good agreement with the expected thickness of a PCBA monolayer¹³ Deposition of the PCBA SAM was carried out by Dr Y.Vaynzof.

3.2.2 Mixed Metal Oxides

Thin films of ZnO and mixed metal oxides Zn_{1-x}Sr_xO/Zn_{1-x}Ba_xO were fabricated by means of sol-gel process using molecular alkoxide precursors (see section 3.1.3). Metal alkoxides exposed to an aqueous environment undergo hydrolysis

and condensation allowing for the metal-oxygen-metal network and hence the metal oxide formation, to occur at low temperatures.¹⁴ For this reason annealing was performed in cleanroom air conditions of controlled humidity. Anhydrous zinc and strontium/barium precursor solutions in 2-methoxyethanol and isopropanol respectively of molar concentration 0.3 M were mixed in a molar oxide ratio of choice to determine the designated alkaline earth doping level x . It was made sure that the doped solutions were colourless, clear solutions and were used on the same day. The precursor solutions were spin-coated at 500 rpm for 1 second followed by 2000 rpm for 1 minute in an inert nitrogen atmosphere followed by a brief 5 minute heating cycle on a 120°C preheated hotplate. The samples were then annealed at 300°C for 1 hour in air and after that let to cool at room temperature. The samples prepared following the above procedure are referred to “as prepared” to discrete from samples which were further annealed for 20 minutes in inert nitrogen atmosphere at 300°C. The oxide thickness was measured by scanning electron microscopy to be 20 - 30 nm.

3.2.3 Electron Blocking Layer

For the fabrication of inverted OPV devices a thin tungsten trioxide (WO_3) layer serving as an electron blocking layer (EBL) was thermally evaporated between the organic active layer and the top electrode at a rate of 0.03 - 0.05 nm s⁻¹ and working pressure of $\sim 10^{-6}$ mbar using a CMS-18 Kurt J. Lesker thermal evaporator inside a glovebox. In the case of a non-transparent device where Ag was evaporated as a top electrode a thin layer of 6 nm was sufficient to serve as EBL, however in the case of a semi-transparent device where ITO was deposited via active ion plasma sputter coating a thicker layer of 20 nm was employed to avoid diffusion of ITO to the organic layer. SuperVac Tungsten Oxide in the form of powder and 99.99% pure was provided from Testbourne Ltd.

3.2.4 Electrode Deposition

For the purposes of this project several different devices were fabricated involving several different top electrodes. The electrode material was chosen such that contact resistance should not be a limiting factor for charge injection and ohmic

contact was achieved whereas conductivity was as high as possible.

Thermally Evaporated Ag and Al

Thermally evaporated electrodes were deposited using an integrated CMS-18 Kurt J. Lesker thermal evaporation system in nitrogen glovebox conditions (O_2 , $H_2O < 10$ ppm); this way the sample was never exposed to air (except for the case of Al in OFETs where the evaporator was kept in cleanroom conditions). During evaporation the chamber pressure was kept below 10^{-6} mbar to limit any oxidation of evaporated ions. The film thickness was measured using an integrated crystal thickness monitor. The material was evaporated through a shadow mask to form the required pattern in each case.

Sputter Coated ITO

ITO was sputter coated by means of r.f. dc sputtering^{30,31} using an Edwards Auto 306 DC and RF Sputter Coater. Films were deposited by bombarding the ITO sputtering target (provided by Testbourne Ltd.) with high-energy Argon plasma ions (RF = 50 W, WP = 5×10^{-4} mbar). The film thickness was monitored using an integrated crystal thickness monitor. Substrates were secured between a ferromagnetic sample holder and the patterning mask with the use of small magnets. This was done in order to make sure that the sample is in good contact with the mask and avoid evaporation of any material outside the margins of the mask (sputter coating has generally a much poorer resolution than thermal evaporation).

Highly Transparent Top Electrode

Particular caution was needed when preparing devices for high resolution optical spectroscopy measurements, where a highly transparent device was required (see chapter 6). For both transparent OPV and OFET devices a highly transparent yet electrically conductive layer is needed to achieve both device operation and high optical transmittance signal to noise ratio. These conditions were found to be best satisfied by (i) a thermally evaporated ultra-thin (5 nm) aluminium layer as top gate for transistors and (ii) a 100 nm thick sputter coated ITO layer as top electrode for solar cells. A summary of the electrodes used for different devices

is shown in table 3.3.

Table 3.3: Top-electrodes and deposition details

Device	Electrode (thickness/nm)	Method	Deposition rate (nm s ⁻¹)
Two-terminal device	Al (100)	Thermal evaporation	0.05 - 0.1
OPV (non-transp.)	Ag (40)	Thermal evaporation	0.05 - 0.1
OPV (transparent)	ITO (100)	Sputter coating	0.2 - 0.7
OFET (transparent)	Al (5)	Thermal evaporation	0.02 - 0.03

3.3 Material Characterisation

A series of physical and chemical analytical techniques as well as electrical measurements were exploited to analyse individual materials prior to being incorporated into an OPV device. Analysing the individual materials systematically can help correlate specific device behaviour to particular layers or interfaces. The need of performing extensive material characterisation was in specific essential for the two novel amorphous mixed metal oxide systems that we have fabricated (chapter 4). Furthermore, when performing stability measurements it was necessary to have information on relative material stability (chapter 7). The film deposition procedure and suitable substrate used for each technique are summarised in the previous section 3.2 and table 3.1 respectively.

3.3.1 Profilometry

Film thickness for the organic layer was measured using a stylus profilometer *Veeco Dektak IIA*. An average was measured by taking several measurements at different film sections by carefully scratching off the organic layer alongside the substrate and recording the height step.

3.3.2 Morphology Probes (*AFM*, *SEM*, *XRD*)

Atomic Force Microscopy (AFM)

Atomic force microscopy was used to investigate the morphology of the novel

mixed, metal oxide films on Si wafer (chapter 4). AFM is a well established imaging technique most commonly used to visualise surface topology providing angstrom range resolution under ideal conditions. Measurements were carried out using a *Veeco Digital Instruments - Dimension 3100* AFM in tapping mode. Topography images and root mean square (RMS) roughness estimates were measured using SPM software in order to compare the film surface quality/crystallinity of different samples.

Scanning Electron Microscopy (SEM)

Scanning electron microscopy has a superior spatial resolution (subnano to 20 nm) and offers a large analysis area ranging from nanometers to millimeters. SEM is a vacuum technique that uses a focused beam of high energy electrons to generate a signal derived from electron-sample interactions when the incident electrons are decelerated in the solid sample. An ultra-high resolution scanning electron microscope *Hitachi S-5500* was used (using 1 - 5 kV energy electrons); the secondary electrons signal was used to produce SEM images. A simple cross section sample holder was used to measure film thickness.

X-ray Diffraction

X-ray diffraction technique is based on Bragg's Law and the principle that an X-ray incident upon a sample will be either transmitted or scattered by the electrons of the atoms in the material. When two X-ray waves with phases separated by an integer number of wavelengths add to make a new wave with a larger amplitude constructive interference occurs and it manifests itself as a peak in an X-ray diffractogram. A high-resolution X-ray diffractometer *Bruker D8* was used to identify crystallographic features in the metal oxide films by comparison with data from known structures. The absence of peaks indicates an amorphous structure. XRD measurements were carried out by Dr.K.K.Banger.

3.3.3 UV-Vis Spectroscopy

Transmission spectra were measured using an *Agilent HP- 8453 UV-Vis* spectrometer. This spectrometer combines two light sources, a deuterium- discharge

lamp and a tungsten lamp for ultraviolet (UV) and visible (Vis) and short wave near infrared (SWNIR) range respectively allowing a spectral range of 190 - 1100 nm. Using a source lens a single collimated beam of light is directed through a correction filter through the sample to the spectrograph where using a holographic grating light is dispersed onto an array of diodes allowing for the spectrum to be measured simultaneously. A clean blank spectrosil was used as reference.

3.3.4 Photoemission Spectroscopy

Photoemission Spectroscopy (PES) is a technique based on the photoelectric effect.³² The surface of the test sample is exposed to high-energy monochromatic photons, resulting in electrons being expelled from the surface upon ionisation. X-ray photoemission spectroscopy (XPS) is typically used to examine core-levels using soft X-rays (200 - 2000 eV) whereas Ultraviolet photoemission spectroscopy (UPS) is used to examine valence levels using vacuum UV irradiation (10 - 45 eV). Samples for PES were fabricated on native oxide/Si substrates and transferred into an ultra-high vacuum (UHV) chamber *ESCALAB 250Xi* (*Thermo Scientific*). PES measurements were carried out by Dr.Y.Vaynzof

X-ray Photoemission Spectroscopy

X-ray Photoemission Spectroscopy was used to characterise the chemical composition of the novel mixed, metal oxides in order to define doping, depth profile and their stability. Measurements were carried out using a XR6 monochromated Al K_{α} source ($h\nu = 1486.6$ eV) and a pass energy of 20 eV. For depth profiling measurements Ar^{+} ion gun (energy of 2000 eV) was used for the etching process. The obtained kinetic energies of the collected core electrons are used to estimate binding energies which are unique to each element. A database of these energies is used to identify distinct transitions originating from a specific element in a particular measurement. Furthermore, different molecular environments affect the core electron binding energies and manifest themselves in the resulting peak shapes (signal intensity against binding energy spectrum).

Ultraviolet Photoemission Spectroscopy

Ultraviolet Photoemission Spectroscopy (UPS) is a very surface-sensitive technique as the photoelectron escape depth is only $\sim 1 - 2$ nm. UPS measurements were performed using a double-differentially pumped He gas discharge lamp emitting He I radiation ($h\nu = 21.22\text{eV}$) with a pass energy of 2 eV.

UPS is a powerful technique for studying the electronic structure of solids. Figure 3.4 shows how important surface potentials such as ionisation potential (I_P), work-function (WF) w.r.t vacuum level (E_{VAC}) and the Fermi level w.r.t the valence band minimum (E_{VBM}) can be estimated from a UPS spectrum. At low binding energies (to the right) the “valence band edge” also refer to as the “HOMO edge” (for organic materials) provides a direct measure of the E_F at the sample surface. The Fermi level of the spectrometer serves as a binding energy reference and is calibrated using a metallic sample. At the high-energy end (to the left) the “secondary electron onset” or “high binding energy cut-off (HBEC)”, provides a direct measure of the specimen’s WF (referenced to the Helium source energy 21.22 eV).

3.3.5 Photothermal Deflection Spectroscopy

Photothermal deflection spectroscopy (PDS) is a highly sensitive spectroscopic technique often used to detect low-lying sub-bandgap absorption features in organic and inorganic materials. PDS detects the non-radiative decay of excited states in a sample by measuring a thermally induced reflection of a probe laser beam propagating parallel to the sample surface. PDS samples were immersed into a cuvette (with optically accessible windows) containing an inert liquid Fluorinert FC-72. Measurements were performed using a chopped monochromatic light illuminating the sample and CW laser beam (670 nm) passing through the refractive index gradient near the sample surface producing a deflection proportional to the absorbed light at that particular wavelength. The deflection, which is proportional to the absorption in the sample, is measured using a position sensing detector and read by a lock-in detector. Measurements were carried out by A.Sadhanala

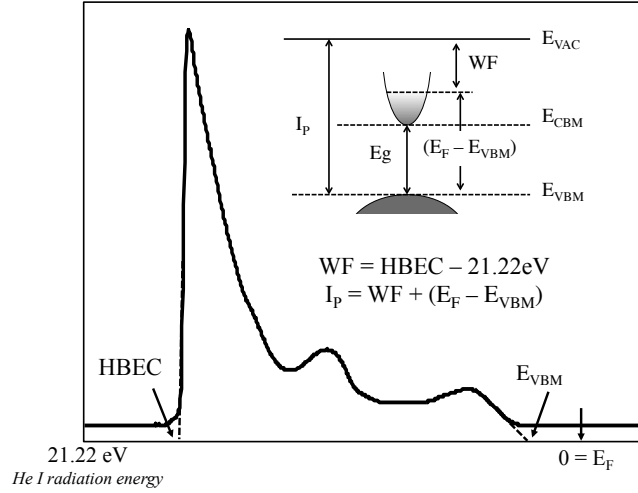


Figure 3.4: Ionisation potential (I_P), work-function (WF), Fermi level (E_F) and valence band minimum (E_{VBM}) estimated from a typical UPS spectrum. The inset shows the corresponding band diagram, where E_{VAC} denotes the vacuum level, E_{CBM} the conduction band minimum and E_g the band-gap energy (usually obtained from UV-Vis absorption spectroscopy). *HBEC* stands for high binding energy cut-off.

3.3.6 Electrical Conductivity

The conductivity of a material can be obtained by measuring the current-voltage (IV) characteristics and physical dimensions of a bar of material. Electrical conductivity measurements were performed to characterise the electronic transport properties of the metal oxide films fabricated in this project and their sensitivity to UV light exposure. Furthermore, time dependent IV characteristics were obtained to characterise the persistent photoconductivity effect for a bare ZnSrO and a fullerene covered ZnSrO film.

The electrical characteristics of ZnO, ZnSrO and ZnBaO thin films were determined by means of two-point probe measurements between two planar aluminium electrodes (electrode width $W = 3$ mm, distance $L = 100$ μm) deposited on top of the oxide thin films as shown in figure 3.5. Aluminium has been chosen as a metal due to the high conductivity and low contact resistance with the metal oxides. Using the IV curves and the film thickness we can estimate conductivity

values according to equation 3.1

$$\sigma \equiv \frac{I}{V} \times \frac{W}{Lt} \quad (3.1)$$

where σ is the conductivity, I the current at voltage V (given that characteristics are linear), W the width of the channel, L the length of the electrodes and t the thickness of the film.

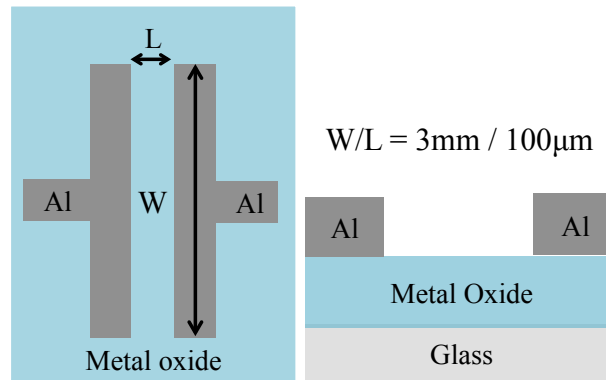


Figure 3.5: Sample configuration for two-point probe conductivity measurements.

3.4 Device Characterisation

3.4.1 Photovoltaic Device Performance

External quantum efficiency and current-voltage measurements were performed to assess the performance of inverted organic and hybrid photovoltaic devices.

External Quantum Efficiency

The external quantum efficiency (EQE) quantity is used to define the ratio of the number of electrons collected at the device electrodes to the incident photons number. It is typically measured for monochromatic light only and it is wavelength (λ) dependent. EQE/% plotted against λ/nm is known as the spectral response of the device. In practice it is easier to measure current and light intensity, rather electron and photon numbers. The short-circuit current density (J_{SC})

measured at incident light of wavelength λ and intensity I can be converted to number of electrons using equation 3.2

$$EQE = \frac{1240J_{SC}}{\lambda I}, \quad (3.2)$$

where 1240 accounts for the appropriate conversion factors (Planck's constant, speed of light and elemental charge) and providing that λ is in nanometres. EQE as a function of wavelength was measured by dispersing light from a tungsten filament (Newport 250W QTH) through a monochromator (Oriel Cornerstone 130). To obtain accurate and reliable measurements the light was focused on a device pixel (area 0.045 cm^2) making sure that the spot size was smaller than the active area. This way the effective device area and the spot size are the same and hence cancel from the numerator and denominator of the efficiency calculation (equation 3.2). The light power was measured by a calibrated reference photodiode of known spectral response. Given that the spot size is contained within the active area of the photodiode the number of photons of a particular wavelength, incident can be determined.

Current-Voltage Characteristics

For typical characterisation of photovoltaic devices we carried out current-voltage (IV) measurements under dark and illumination. Typical such measurements are illustrated in figure 3.6. In the following equations the current density quantity ($J = I/\text{active area}$) is used to account for the active area of the device. For the *light* J-V curve (solar cell under operation) the current density at zero voltage is referred to as the short-circuit current density (J_{SC}) and the voltage at zero current as the open-circuit voltage (V_{OC}). At the maximum power point (J_{MPP}, V_{MPP}), the product of current and voltage is maximum ($P_{max} = J_{MPP} \times V_{MPP}$). Dividing P_{max} with the product of J_{SC} and V_{OC} yields the fill factor (FF):

$$FF = \frac{V_{MPP} \times J_{MPP}}{V_{OC} \times J_{SC}} \quad (3.3)$$

The power conversion efficiency (PCE) of the device is defined as the ratio of the output electrical power to the input light power and is described by:

$$PCE = \frac{V_{OC} \times J_{SC} \times FF}{I} \quad (3.4)$$

For low intensity ($< 1 \text{ mWcm}^{-2}$), monochromated light IV measurements the

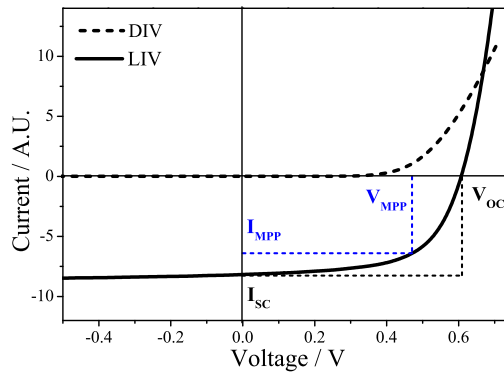


Figure 3.6: Dark (dashed) and under illumination (solid) current-voltage (IV) curves of a typical organic solar cell. V_{OC} is the open-circuit voltage, I_{SC} the short-circuit current whereas V_{MPP} and J_{MPP} the maximum power point voltage and current respectively.

same light source as for EQE measurements was used. High intensity (100 mWcm^{-2}), AM 1.5G light IV measurements were measured using a calibrated Abet Sun 3000 solar simulator, corrected for spectral mismatch using a calibrated reference Si cell. Voltage bias was applied and current was measured using a Keithley 2635 source-measure unit.

3.4.2 Electroabsorption Spectroscopy

Electroabsorption (EA) spectroscopy measures changes in absorption under the application of an external electric field, which is modulated by a periodic external field. This technique is based on the theory of the electric field effect on the dielectric function of solids developed by means of perturbation theory.³³ The fundamental EA-response is proportional to the imaginary part of the third order

susceptibility $\text{Im}\chi^{(3)}(h\nu)$ and the square of the electric field inside the material³⁴

$$\Delta\alpha(h\nu) \propto \frac{\Delta R}{R}(h\nu) \propto \text{Im}\chi^{(3)}(h\nu)E^2, \quad (3.5)$$

where α is the absorption coefficient, $h\nu$ is the photon energy, R is the reflectance and E is the electric field. In a uniform dielectric, the response to a sinusoidal voltage of the form $V = V_0 + V_{ac}\sin(\omega t)$ is

$$\begin{aligned} \frac{\Delta R}{R}(h\nu) &\propto \chi(h\nu)V^2 \\ &= \chi(h\nu)\{V_{ac}^2[1 - \cos(2\omega t)]/2 \\ &\quad + 2V_{ac}V_0\sin(\omega t) + V_0^2\} \end{aligned} \quad (3.6)$$

It follows from the above equation that in the presence of a static potential the EA can be modulated at both the fundamental and the second harmonic frequency of the applied ac voltage. For the purposes of this project we are interested in measuring the built-in voltage (V_{bi}) across a polymer and therefore concentrate on the signal measured at the fundamental frequency ω . Taking into account that the “true” dc voltage across the polymer (V_0) is equal to the externally applied dc voltage (V_{dc}) minus the built-in voltage across the polymer, the following equation is derived from equation 3.6

$$\begin{aligned} \frac{\Delta R}{R}(\omega) &\propto \chi(h\nu)V_0V_{ac}\sin(\omega t) \\ &\propto (V_{dc} - V_{bi})V_{ac}\sin(\omega t) \end{aligned} \quad (3.7)$$

From equation 3.7 it is expected that the EA response modulated at ω , at a constant photon energy ($h\nu$) and amplitude (V_{ac}) should vary linearly with V_{dc} and vanish when V_{dc} compensates the built-in voltage of the device, which mainly originates from the difference of work-function of the two electrodes.³⁵

For EA measurements, light from a combination of a 150W xenon arc lamp (Oriel 6253) and a 50W quartz tungsten halogen lamp (Oriel 6332) was dispersed through a monochromator illuminator (Newport 7340). The photodiode used for the detection was an silicon photodiode (OPT 301) with a home-made amplifier circuit. A dual channel lock-in amplifier (SR 830 from Stanford Re-

search Systems) and a digital dc multimeter (HP34401A) were used. Before

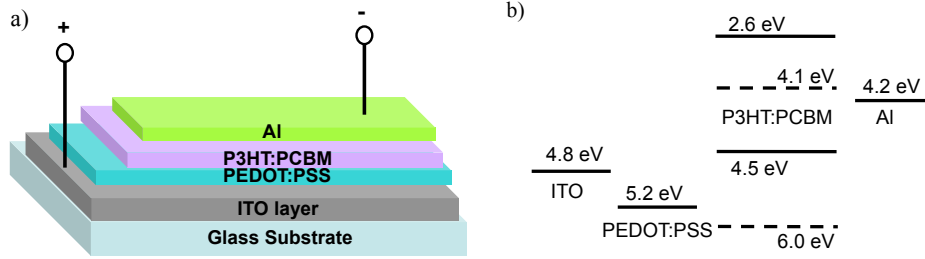


Figure 3.7: Device architecture (a) and energy levels representation (b) diagrams. Figure kindly provided by C.Li.

carrying out the necessary measurements for chapter 4 we performed some preliminary tests on a model solar cell system to verify the reliability of the system. Figure 3.7 shows the device architecture and energy level diagram for a model ITO/PEDOT:PSS/P3HT:PCBM/Al solar cell device; and the corresponding device characteristics shown in Figure 3.8 confirm the functionality of the device.

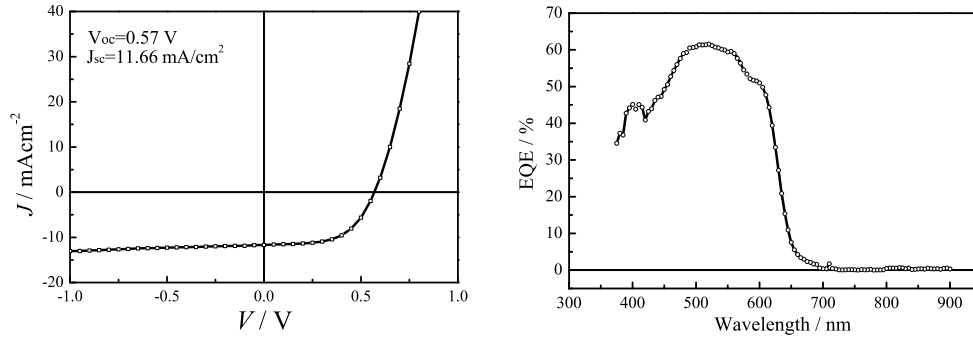


Figure 3.8: (Left) J-V Device characteristics and (right) EQE of test device. Figures provided by C.Li.

Figure 3.9(left) shows the first harmonic EA spectrum at -3 V as well as the first derivative of pure P3HT UV-visible absorption spectrum. These two lines are consistent with each other, which indicate that the EA signal of device is mainly from the P3HT. Also, the EA spectrum exhibits the first derivative

lineshape, indicating that the dipole moment induced by the external field in the P3HT material is the main contribution of the EA signal. To obtain the optimal signal-to-noise ratio, we carried out the bias dependence EA response at photon energy of ~ 2.0 eV. The corresponding first harmonic EA response as a function of external bias is shown in figure 3.9(right). The value of the device V_{bi} is obtained from the extrapolation of the linear regime in reverse bias and is equal to 0.9 V, This is consistent with the work function difference between PEDOT:PSS and Al indicated in the energy diagram therefore verifying the functionality of the setup. The control measurements shown in figure 3.10 show that the EA signal is independent of the intensity of the probe light and that there is no influence as well for AC frequencies above 500 Hz (AC frequency). We used an AC frequency of 2013.31 Hz for all experiments. All EA measurements were performed by Cheng Li.

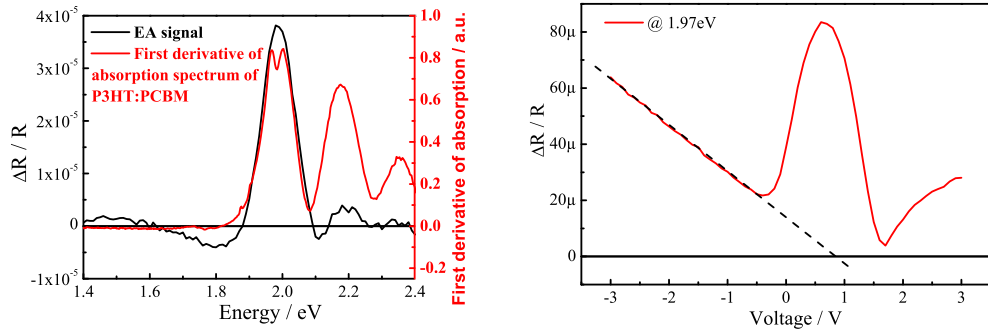


Figure 3.9: (Left) First harmonic EA spectrum at -3V and first derivative of pure P3HT UV-Visible absorption spectrum and corresponding (right) EA response. Figures provided by C.Li.

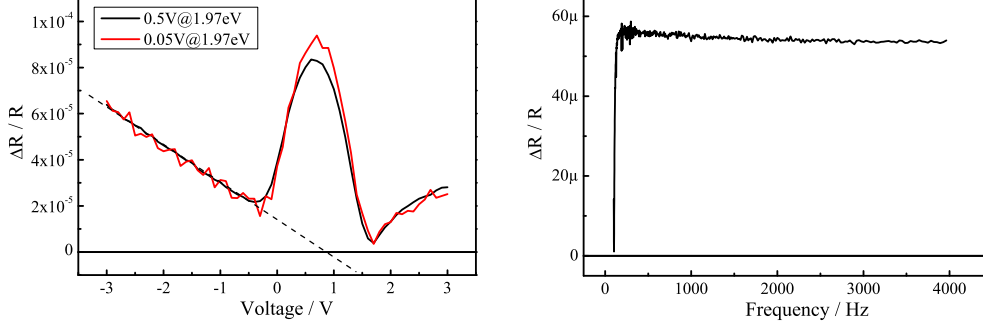


Figure 3.10: (Left) Light intensity dependence of EA signal and (right) AC frequency dependence of the EA signal.

3.4.3 Pump-Push Photocurrent Spectroscopy

Pump-push-photocurrent spectroscopy (PPPc) is a new time-resolved technique, recently developed by Bakulin *et al.*, that directly probes bound, interfacial charge-pairs.³⁶ A regenerative 1 kHz Ti:Sapphire amplifier system (Coherent, Legend Elite Duo) was used to pump a broadband non-collinear optical amplifier (Clark) and a 3-stage home-built optical parametric amplifier to generate visible pump pulses (~ 540 nm central wavelength, ± 20 nm bandwidth) and infrared push pulses (2000 ± 100 nm), respectively. ~ 1 nJ pump and $\sim 1 \mu$ J push pulses were focused onto a $\sim 1 \text{ mm}^2$ spot on the device. The reference photocurrent from a photodiode was detected at a pump repetition frequency of 1 kHz by a lock-in amplifier. The push beam was mechanically chopped at ~ 370 Hz, and its effect on the photocurrent was also detected by a lock-in amplifier. Push pulse by itself also induced minor current in the device due to absorption from sub-gap states and long-lived trapped charges. This current component was delay independent and was subtracted from the presented measurements. PPPc measurements were performed by Dr A.A.Bakulin.

References

- [1] Sirringhaus, S., Brown, P.J., Friend, R.H., Nielsen, M.M., Bechgaard, K., Langeveld-Voss, B.M.W., Spiering, A.J.H., Janssen, R.A.J., Meijer, E.W., Herwig, P., and de Leeuw, D.M. (1999) *Nature*, **401**, 685–688. 42
- [2] Choulis, S.A., Kim, Y., Nelson, J., Bradley, D.D.C., Giles, M., Shkunov, M., and McCulloch, I. (2004) *Applied Physics Letters*, **85**, 3890–3892. 42
- [3] Raja, M., Lloyd, G.C.R., Sedghi, N., Eccleston, W., Lucrezia, R.D., and Higgins, S.J. (2002) *J. Appl. Phys.*, **92**, 1441. 42
- [4] Shaw, P.E., Ruseckas, A., and Samuel, I.D.W. (2008) *Advanced Materials*, **20**, 3516–3520. 42
- [5] Yang, X. and Uddin, A. (2014) *Renewable and Sustainable Energy Reviews*, **30**, 324 – 336. 42
- [6] Liang, Y., Wu, Y., Feng, D., Tsai, S.T., Son, H.J., Li, G., and Yu, L. (2009) *Journal of the American Chemical Society*, **131**, 56–57. 42
- [7] Liang, Y., Wu, Y., Feng, D., Tsai, S.T., Son, H.J., Li, G., and Yu, L. (2009) *Journal of the American Chemical Society*, **131**, 56–57. 42, 43
- [8] Liang, Y., Xu, Z., Xia, J., Tsai, S.T., Wu, Y., Li, G., Ray, C., and Yu, L. (2010) *Advanced Materials*, **22**, E135–E138. 43
- [9] Liang, Y., Wu, Y., Feng, D., Tsai, S.T., Son, H.J., Li, G., and Yu, L. (2009) *Journal of the American Chemical Society*, **131**, 56–57. 43
- [10] He, Z., Zhong, C., Huang, X., Wong, W.Y., Wu, H., Chen, L., Su, S., and Cao, Y. (2011) *Advanced Materials*, **23**, 4636–4643. 43
- [11] Soon, Y.W., Cho, H., Low, J., Bronstein, H., McCulloch, I., and Durrant, J.R. (2013) *Chem. Commun.*, **49**, 1291–1293. 43
- [12] Allemand, P.M., Koch, A., Wudl, F., Rubin, Y., Diederich, F., Alvarez, M.M., Anz, S.J., and Whetten, R.L. (1991) *Journal of the American Chemical Society*, **113** (3), 1050. 44

-
- [13] Vaynzof, Y., Kabra, D., Zhao, L., Ho, P.K.H., Wee, A.T.S., and Friend, R.H. (2010) *Applied Physics Letters*, **97**, 033 309. 44, 48
 - [14] Banger, K.K., Yamashita, Y., Mori, K., Peterson, R.L., Leedham, T., Rickard, J., and Sirringhaus, H. (2011) *Nature Materials*, **10**, 45–50. 45, 49
 - [15] Gwinner, M., Vaynzof, Y., Banger, K.K., Ho, P.K.H., Friend, R.H., and Sirringhaus, H. (2010) *Advanced Functional Materials*, **20** (3457). 45
 - [16] Reynolds, K.J., Barker, J.A., Greenham, N.C., Friend, R.H., and Frey, G.L. (2002) *J. Appl. Phys.*, **92**, 7556. 46
 - [17] Meyer, J., Hamwi, S., Kröger, M., Kowalsky, W., Riedl, T., and Kahn, A. (2012) *Adv. Mater.*, **24**, 5408. 46
 - [18] Di Pietro, R. (2012) *Charge Accumulation Spectroscopy of Organic Semiconductors*, Ph.D. thesis, University of Cambridge. 46
 - [19] Soultati, A., Georgiadou, D., Douvas, A., Argitis, P., Alexandropoulos, D., Vainos, N., Stathopoulos, N., Papadimitropoulos, G., Davazogloua, D., and Vasilopoulou, M. (2014) *Microel. Eng.*, **117**, 13. 46
 - [20] Tao, C., Ruan, S., Xie, G., Kong, X., Shen, L., Meng, F., Liu, C., Zhang, X., W., D., and Chen, W. (2009) *Appl. Phys. Lett.*, **94**, 043 311. 46
 - [21] Han, S., Shin, W., Seo, M., Gupta, D., Moon, S.J., and Yoo, S. (2009) *Organic Electronics*, **10**, 791. 46
 - [22] Bolink, H., Coronado, E., Orozco, J., and Sessolo, M. (2009) *Adv. Mater.*, **21**, 79. 46
 - [23] Kröger, M., Hamwi, S., Meyer, J., Riedl, T., Kowalsky, W., and Kahna, A. (2009) *Org. Electron.*, **10**, 932. 46
 - [24] Irfan, Ding, H., Gao, Y., Small, C., Kim, D.Y., Subbiah, J., and So, F. (2010) *Appl. Phys. Lett.*, **96**, 243 307. 46
 - [25] Ling, M. and Bao, Z. (2004) *Chem. Mater.*, **16**, 4824. 47

REFERENCES

- [26] Moulé, A.J., Bonekamp, J.B., and Meerholz, K. (2006) *J. Appl. Phys.*, **100**, 094 503. 48
- [27] Li, G., Shrotriya, V., Yao, Y., and Yang, Y. (2005) *J. Appl. Phys.*, **98**, 043 704. 48
- [28] Collins, B.A., Li, Z., Tumbleston, J.R., Gann, E., McNeill, C.R., and Ade, H. (2013) *Advanced Energy Materials*, **3** (1), 65–74. 48
- [29] Olson, D.C., Lee, Y.J., White, M., Kopidakis, N., Shaheen, S.E., Ginley, D.S., Voigt, J.A., and Hsu, J.W.P. (2007) *Journal of Physical Chemistry C*, **111**, 16 640. 48
- [30] Cui, H.N. and Xi, S.Q. (1996) *Thin Solid Films*, **288**, 325. 50
- [31] Zhang, K., Zhu, F., Huan, C., and Wee, A. (1999) *J. Appl. Phys.*, **86**, 974. 50
- [32] Hüfner, S. (2003) *Photoelectron Spectroscopy: Principles and Applications*, Springer-Verlag, 3rd edn.. 53
- [33] Aspnes, D.E. and Rowe, J.E. (1972) *Phys. Rev. B*, **5**, 4022. 58
- [34] Campbell, I.H., Hagler, T.W., and Smith, D.L. (1996) *Phys. Rev. Lett.*, **76**, 1900. 59
- [35] Campbell, I.H., Hagler, T.W., Smith, D.L., and Ferraris, J.P. (1996) *Physical Review Letters*, **76**, 1900. 59
- [36] Bakulin, A., Rao, A., Pavelyev, V., van Loosdrecht, P.H.M., Pshenichnikov, M.S., Niedzialek, D., Cornil, J., Beljonne, D., and Friend, R.H. (2012) *Science*, **335**, 1340. 62

Chapter 4

ZnSrO and ZnBaO Electron Extraction Layers for Inverted Organic Photovoltaics

In this chapter we investigate the benefits of using two novel ternary oxides, Strontium (Sr) and Barium (Ba) doped Zinc Oxide (ZnO), as electron extraction layers (EEL) in performance and stability of inverted organic photovoltaics. After thorough characterisation of the novel oxide thin films and devices we demonstrate that the use of amorphous, mixed metal oxides allows improving the performance and stability of interfacial charge extraction layers for organic photovoltaics and we propose a mechanism behind this improvement.¹

¹Part of work discussed in this chapter has been previously published in: (a) *“Improved Performance and Stability of Inverted Organic Solar Cells with Sol-Gel Processed, Amorphous Mixed Metal Oxide Electron Extraction Layers comprising Alkaline Earth Metals”* O. Pachoumi, C. Li, Y. Vaynzof, K.K. Banger and H. Sirringhaus, Adv. Energy Mater. 3, 1428-1436 (2013) and (b) *“Stability investigations of inverted organic solar cells with a sol-gel processed ZnSrO or ZnBaO electron extraction layer”* O. Pachoumi, C. Li, Y. Vaynzof, K.K. Banger, H. Sirringhaus, Proc. SPIE 8830, Organic Photovoltaics XIV, 88300E (2013).

4.1 Introduction

During the last decade significant effort has been devoted to improving the poor operational stability of organic photovoltaic devices (OPV).¹ Although many of the underlying mechanisms leading to degradation are yet not fully understood in many cases poor device stability has been associated with oxidation of low metal electrodes and the acidic nature of specific charge extraction layers like PEDOT:PSS. Research focused on degradation due to these factors has led to the design of the *inverted* architecture and the resulting devices, known as inverted organic photovoltaic devices, exhibited significant improvements in device stability (see section 2.3). Despite the advantages the inverted architecture offers a new range of instabilities related to interlayer and interface processes is commonly observed. Such instabilities were associated with solution processed conductive metal oxides, such as ZnO and TiO₂ which are widely used in optoelectronic devices and serve as electron extraction layers (EEL) in OPV. The need of a UV light soaking step before achieving good photovoltaic performance is one of the most common manifestations of these instabilities when ZnO is used as EEL.^{2,3,4,5,6,7} The resulting improvement in device performance is non-permanent and its origin not fully understood (see section 2.3).

ZnO has drawn special interest due to its beneficial properties such as high conductivity and transparency, as well as the simplicity and low cost of solution processing.^{8,9,10,11} It is well known that the ZnO surface and hence its electronic properties are sensitive to oxygen adsorption/desorption depending on the deposition method and the surrounding ambient conditions. It has been suggested that under dark conditions, oxygen adsorbs at oxygen deficient surface states creating a negatively charged ion by trapping a free electron from the n-type ZnO.¹² Oxygen desorption can be introduced by UV irradiation, N₂ annealing or by applying a positive bias when in diode configuration, which has been exploited in diodes with memory effects.^{13,14,15} Thus depending on a variety of parameters the surface of the ZnO thin film exhibits different electronic properties resulting in an unreliable and unpredictable OPV performance.

In TFT applications it has been realized some time ago that the use of amorphous, ternary and quaternary mixed metal oxides, such as InGaZnO, produced

by sputtering provides improved device performance and stability compared to pure binary compounds, such as In_2O_3 or ZnO . The incorporation of Ga as a dopant stabilizes the concentration of oxygen vacancies in the film and allows for robust control of carrier concentration and threshold voltage. It is natural to ask whether similar benefits could also be achieved when using oxides as EELs in organic solar cells. Recently, ZnO films doped with indium have been investigated as EELs.¹⁶ A small increase in short circuit current was observed, but no stability measurements were reported. Our group has recently developed a low-temperature, solution-processing approach to mixed, metal oxides based on sol-gel processing of metal alkoxide precursors. This route provides versatile access to a wide range of mixed metal oxides and compositions and we demonstrated fabrication of high-performance TFTs of InZnO and InGaZnO at process temperatures as low as 230°C .¹⁷

Furthermore, inspired by the LiF/Al bilayer cathode for Organic Light Emitting Diodes (OLEDs)¹⁸ various organic and inorganic alkali or alkaline earth metal compounds and complexes (such as CaF_2 , SrF ,^{19,20} Cs_2CO_3 ,^{21,22} Li_2O ,²³ Liq ,²⁴ and $\text{Ba}(\text{OH})_2$ ²⁵) have been used to modify the injection/ extraction properties of an Al cathode or ZnO EEL, in various organic electroluminescent devices by workfunction modification or doping of the organic semiconductor.

In this work we investigate the application of such sol-gel processed, amorphous mixed metal oxides as EELs in OPV. We investigate in particular the use of amorphous oxides comprising alkaline earth metals, such as strontium and barium. Our choice of Sr and Ba metals was primarily inspired by their higher Gibbs energy of oxidation than gallium (based on the calculation of the Gibbs energy of oxidation for a variety of dopants candidates) and their larger cation radii (see table 4.1); in addition to their binary oxidation states (+2) as well as the wide band gaps (4.0 - 6.5 eV) of the oxides they form. The tight oxygen binding to Sr and Ba is thought to suppress the formation of oxygen vacancies in the film and might impart a higher operational stability on the charge extraction layers. In addition the fact that Ba and Sr have significantly larger cation radii than Zn could impart sufficient disorder in the resulting ternary oxide framework to promote the formation of an amorphous phase. Recently, it was reported in our group that replacing gallium oxide with either barium or strontium oxide affords

amorphous, high performance semiconducting oxides with high carrier mobility up to $25 \text{ cm}^2 \text{ V}^{-1} \text{ s}^{-1}$ and demonstrates improved electrical stability.²⁶

Table 4.1: Cation radii and Gibbs energy of oxidation data on metal oxides²⁶

Metal oxide	Cation radii (pm)	$-\Delta G_f$ (eV)	$-\Delta G_f/\text{oxygen}$ (eV)
ZnO	134	6.32	6.32
BaO	222	10.33	10.33
SrO	215	11.14	11.14
MgO	160	11.16	11.16
CaO	197	11.93	11.93
In ₂ O ₃	167	5.40	3.60
Ga ₂ O ₃	135	6.49	4.33
HfO ₂	159	9.94	4.97
ZrO ₂	160	10.20	5.10
Al ₂ O ₃	143	10.41	6.94
Y ₂ O ₃	180	11.87	7.91

Using poly [3-hexylthiophene] (P3HT): [6, 6]-phenyl C60 butyl acid methyl ester (PC₆₀BM) cells as a model system we present a comprehensive study on the origin of the device performance improvement upon UV light soaking observed in ZnO EELs and demonstrate that the need for light soaking can be circumvented by doping ZnO with alkaline earth metals such as Strontium or Barium at a doping composition as low as 3 at%. Since we have synthesized two novel mixed metal oxides we find it crucial that we analyze the individual materials systematically to collect information on relative material stability. In section 4.2 the individual oxides: ZnO, ZnSrO and ZnBaO are analysed prior to being incorporated into an OPV device using a variety of probe techniques (microscopy, spectroscopy and electrical measurements). In section 4.3 the complete OPV device is analysed in order to study a wide range of phenomena related to interlayer and interface processes, which could contribute to the overall device performance and stability. After demonstrating that the light soaking step is circumvented and the overall device performance improved with Sr and Ba doping we discuss in section 4.4

how results obtained from a variety of probe techniques (including EA, IV and XPS) can help interpret the mechanism behind this improvement.

4.2 Metal Oxide Characterisation

Since we have fabricated two novel ternary oxides: zinc strontium oxide ($\text{Zn}_{1-x}\text{Sr}_x\text{O}$) and zinc barium oxide ($\text{Zn}_{1-x}\text{Ba}_x\text{O}$) we performed an extensive characterization of the films chemical composition, surface roughness and morphology, optical transmittance, energy levels and electrical conductivity, to understand in detail the effect of doping on the oxide properties and hence the origin of their improved performance compared to binary ZnO. The Ba-doped ZnO and Sr-doped ZnO films were fabricated by means of sol-gel deposition using alkoxide molecular precursor solutions. The doped films were spin-coated from Ba-doped or Sr-doped zinc oxide inks where the ZnO alkoxide precursor and BaO or SrO alkoxide precursor solutions were mixed in a ratio of choice to determine the designated alkaline earth doping level x , described in more detail in section 3.2.2. First we investigate the effect of doping level on device performance. Clear inks of barium zinc oxide and strontium zinc oxide at 9:1, 8:2, 7:3, 6:4 and 5:5 zinc to dopant molar oxide ratio were prepared, thin films were deposited from them and OPV devices fabricated. The resulting device performance showed a sharp decrease in the short-circuit current density and power conversion efficiency when the dopant ratio was increased from 9:1 to 8:2 and above (not shown here). This significant drop in current was thought to be due to a drop in conductivity of the resulting mixed metal oxide film. We therefore turned our focus towards lower doping levels ($x < 20\%$). The results of this study are presented later on in section 4.3.1 figure 4.12, where the Sr/Ba precursor solution content (vol.%) at this point represents the postulated dopant percentage. The optimum % doping level with regards to device performance efficiency for both Sr and Ba was found to be 3%. The actual metal oxide content (at.%) was verified by XPS analysis only for the optimum doping % films and is presented in the first subsection. The following metal oxide characterisation study presented in the following subsections accounts for these optimised and verified films.

4.2.1 Chemical Composition

High-resolution X-ray photoemission spectroscopy (XPS) was undertaken to verify the incorporation of Sr and Ba in the ZnO film and to determine the elemental compositions of the optimised films. It should be noted that the doping percentage for the optimised Ba-doped and Sr-doped ZnO films under investigation was intended to be 3% in both cases. $Zn2p$, $O1s$, $Sr3d$ and $Ba3d$ spectra of the three films (undoped ZnO, 3% Ba-doped and 3% Sr-doped ZnO) are depicted in figures 4.1, 4.2 and 4.3. The binding energies of zinc and oxygen show the formation of ZnO (1022 eV for $Zn2p$ and 530 eV for $O1s$)²⁷. The incorporation of Sr and Ba in the doped films can be clearly seen in the scans. The chemical state of strontium, corresponding to the binding energies of 137 eV and 135 eV for $Sr3d3$ and $Sr3d5$ respectively²⁸ was detected in the ZnSrO films (figure 4.2). The chemical state of barium, corresponding to the binding energies 797 eV and 781 eV for $Ba3d3$ and $Ba3d5$ respectively²⁹, was detected in the ZnBaO films (figure 4.3).

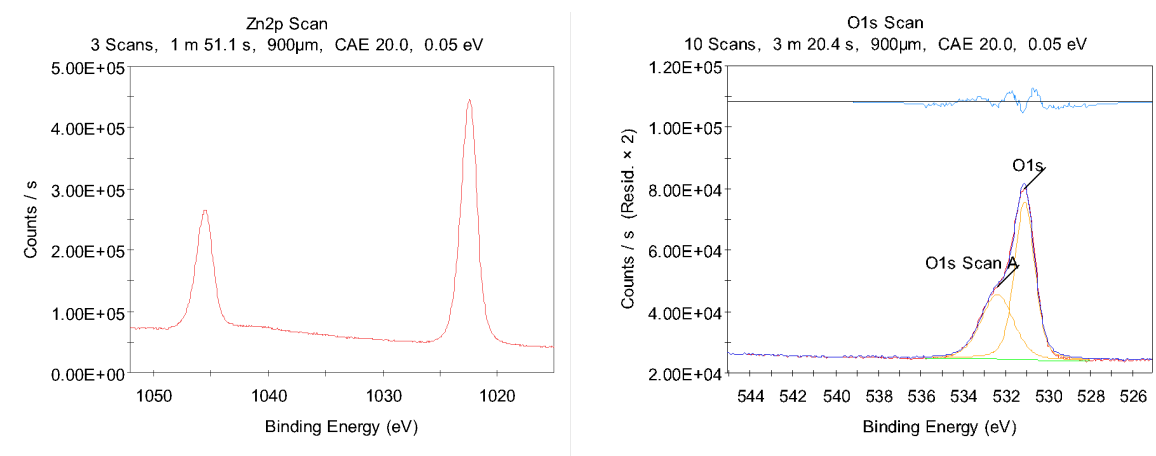


Figure 4.1: $Zn2p$ and $O1s$ XPS scans for ZnO.

In order to gather more information regarding the chemical composition of the metal oxide films in the bulk we have recorded depth profile XPS measurements for the three films. The XPS depth profiles for the undoped ZnO, 3% Sr-doped and 3% Ba-doped ZnO thin films are shown in figure 4.4 and show the atomic percentages derived from the $Sr3d5$, $Ba3d5$, $Zn2p$, $O1s$ and $C1s$ integrated

4.2 Metal Oxide Characterisation

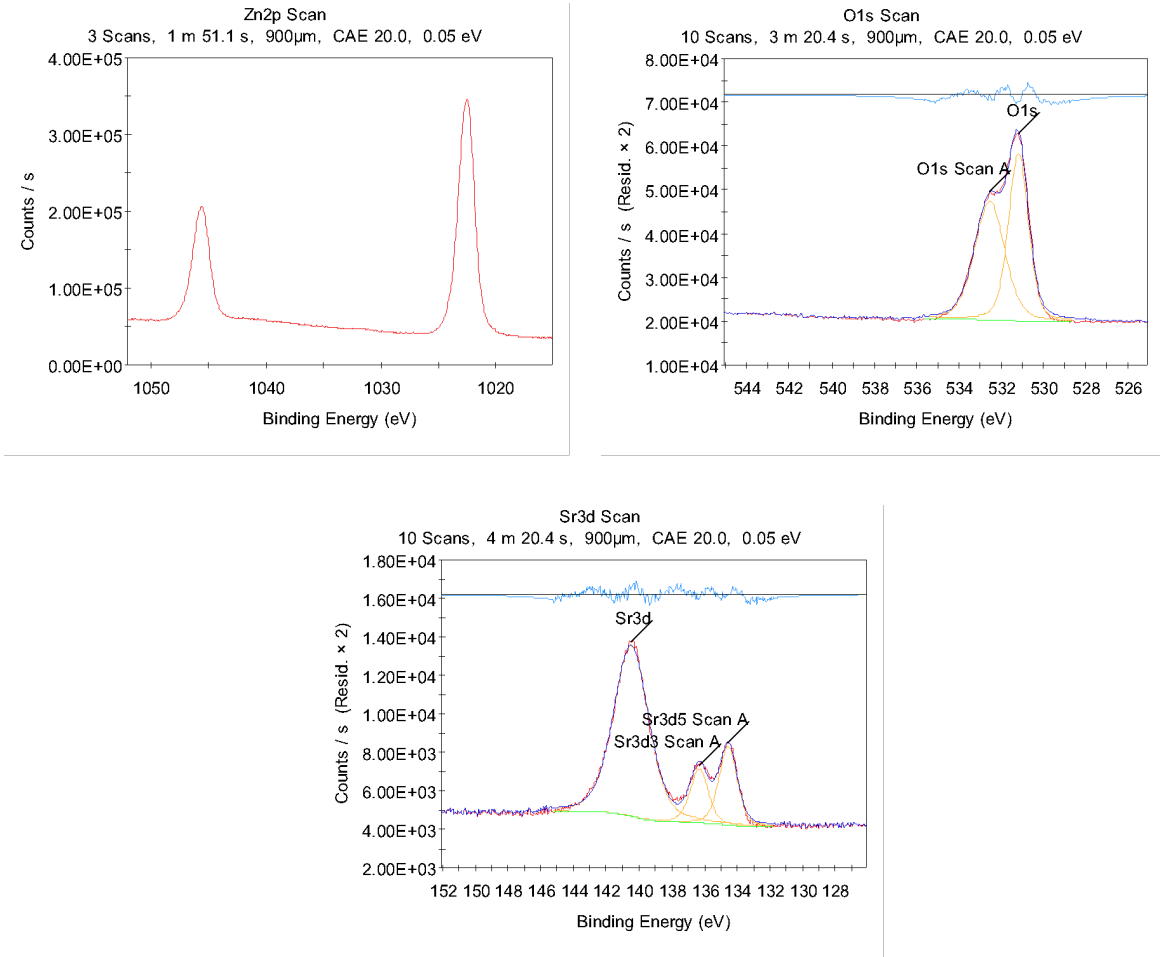


Figure 4.2: Zn2p, O1s and Sr3d XPS scans for ZnSrO.

XPS peaks. In all films the carbon 1s peak is present only on the surface as a result of adsorbed hydrocarbon contamination indicating that despite relatively low annealing temperature the precursor decomposes cleanly leaving no organic residues that can be detected by XPS. An atomic composition of 3.18 ± 0.07 % Sr and 3.17 ± 0.05 % Ba, close to the expected 3%, was obtained. In addition the atomic composition was homogeneous throughout the film and there was no evidence for segregation of the dopant to the surface i.e. bulk and surface compositions are very similar. Both doped films show comparable oxygen deficiency to the undoped ZnO film suggesting that the doping process does not cause a

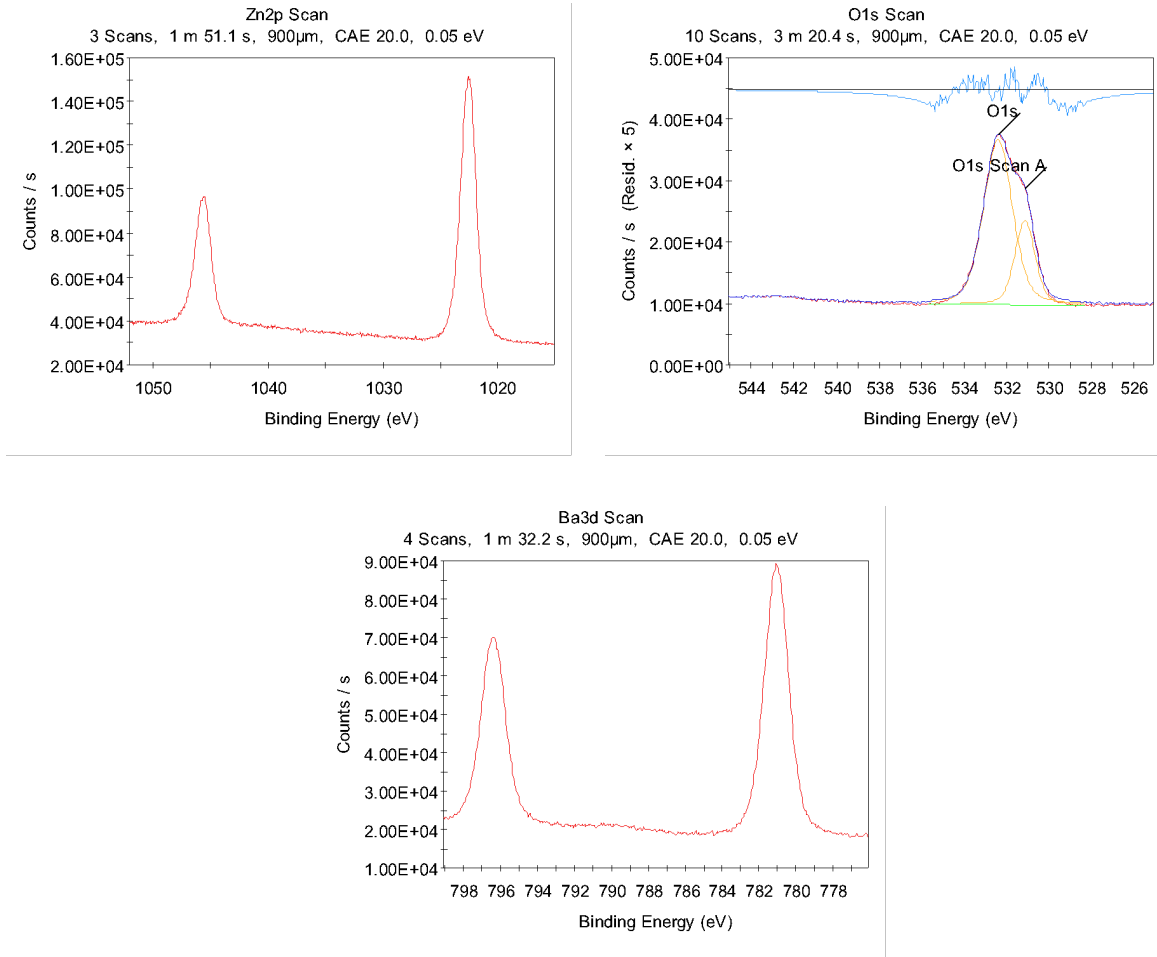


Figure 4.3: Zn2*p*, O1*s* and Ba3*d* XPS scans for ZnBaO.

significant effect on the overall Zn/O stoichiometry. In all films the O1*s* peak is very broad, with a pronounced fine structure indicating multiple oxygen environments leading to different chemical shifts. More emphasis on the importance of the O1*s* peak and the relevant contributions consisting it are further discussed in section 4.4.2 and used to explain changes in properties and also changes with UV exposure. The Si 2*p* contribution is due to the SiO₂/Si substrate. A brief description of the XPS technique is given in section 3.3.4. From this point on we will express ZnO doped films of intended 3% Sr or Ba dopant as Zn_{0.97}Sr_{0.03}O and Zn_{0.97}Ba_{0.03}O although the exact actual at.% may vary between different batches.

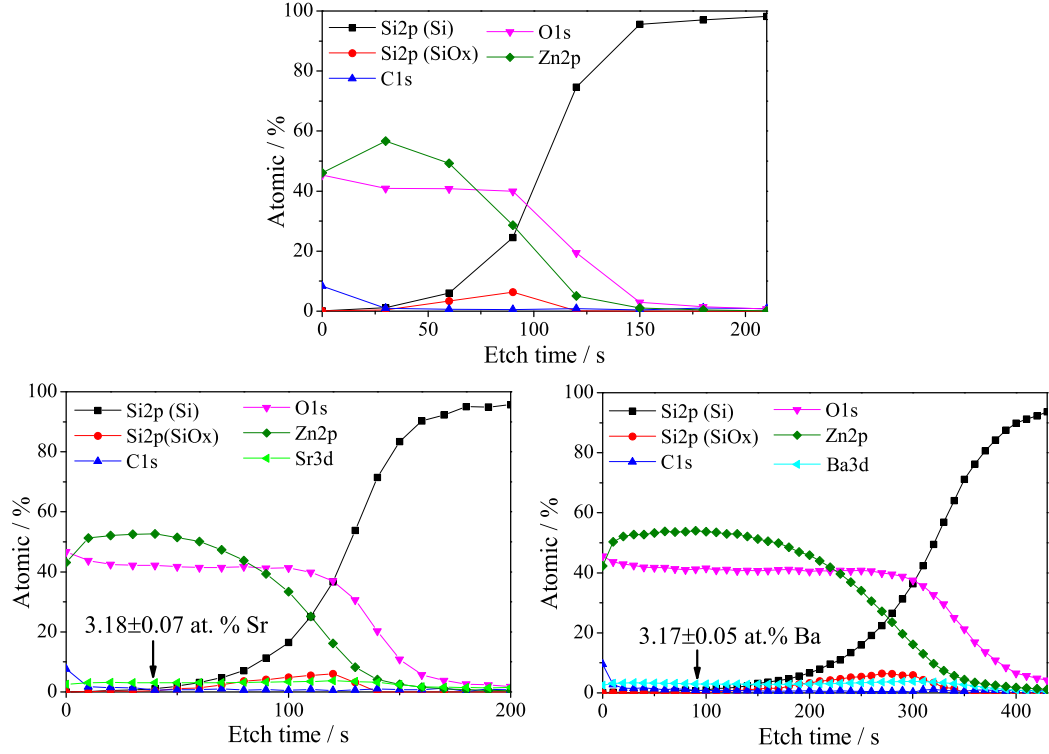


Figure 4.4: XPS depth profiles for ZnO (top), $\text{Zn}_{0.97}\text{Sr}_{0.03}\text{O}$ (bottom left) and $\text{Zn}_{0.97}\text{Ba}_{0.03}\text{O}$ (bottom right) films on Si substrate.

4.2.2 Surface and Bulk Microstructure

The morphology of the metal oxide films was further investigated by means of Atomic Force Microscopy (AFM), Scanning Electron Microscopy (SEM) and X-ray Diffraction (XRD) (see section 3.3.2). The XRD measurements summarised in figure 4.5 are characterised by a flat spectrum with no distinct peaks showing no evidence of crystalline character for all the films or suggesting very weak nano-crystalline regions which are not detectable by this technique. It is noted here that background noise was subtracted from the XRD measurements. Further experiments are therefore required to conclude on the crystalline character of the films. Perhaps by comparing XRD measurements of films prepared at different

sol-gel annealing temperatures (250°C , 300°C , 450°C) we could detect changes in the morphology of the films associated with crystalline and amorphous regions since the crystallisation process is aided at higher temperatures. Furthermore a higher resolution technique such as high resolution transmission electron microscopy (HRTEM) could be used to investigate any nano-crystalline regions.³⁰ AFM scans (figure 4.6) taken in contact mode, show a similar ~ 1 nm smooth root mean square (R_{rms}) surface roughness for all films and no distinctive crystalline domains. SEM pictures verify that there are no significant variations in thickness between the films which is consistently $\sim 24 \text{ nm} \pm 5 \text{ nm}$. From the results of this section we can conclude that at the doping levels used for this experiment there were no significant changes to the microstructure of the films detectable by XRD, AFM or SEM techniques and it is very unlikely that any changes in film properties or device performance discussed later on are caused by changes in morphology, surface roughness or thickness.

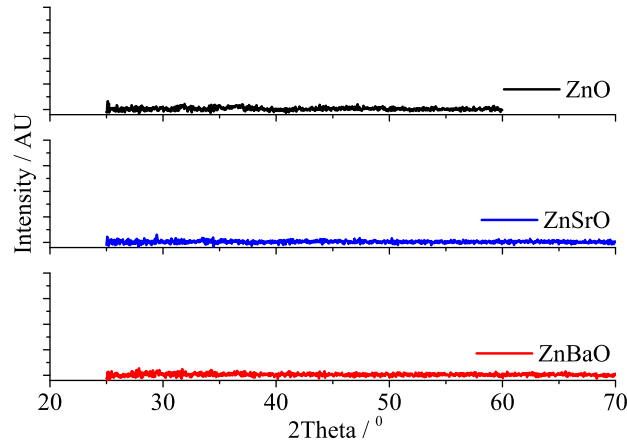


Figure 4.5: θ - 2θ X-ray diffractogram of ZnO, $\text{Zn}_{0.97}\text{Sr}_{0.03}\text{O}$ and $\text{Zn}_{0.97}\text{Ba}_{0.03}\text{O}$ films on glass, annealed at 300°C , showing no evidence of crystalline nature (background noise has been subtracted).

4.2 Metal Oxide Characterisation

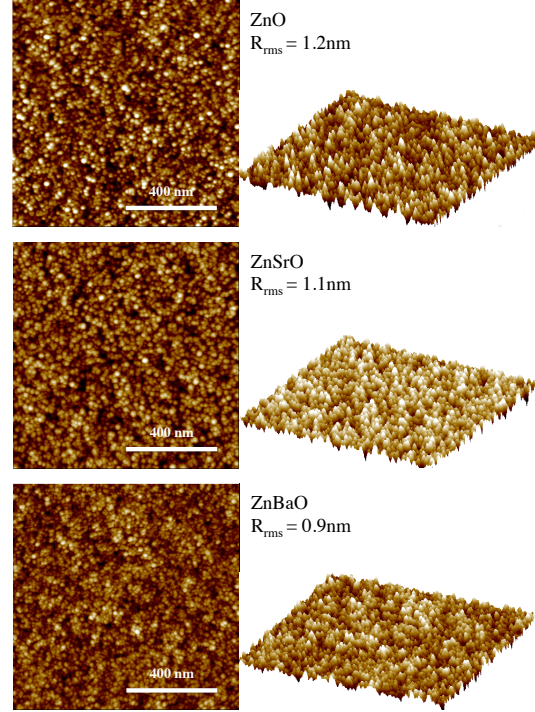


Figure 4.6: AFM surface morphology of ZnO (top), Zn_{0.97}Sr_{0.03}O (middle) and Zn_{0.97}Ba_{0.03}O (bottom) films on Si wafer, made at 300°C. All three films show similar root mean square surface roughness (R_{rms}) close to 1 nm.

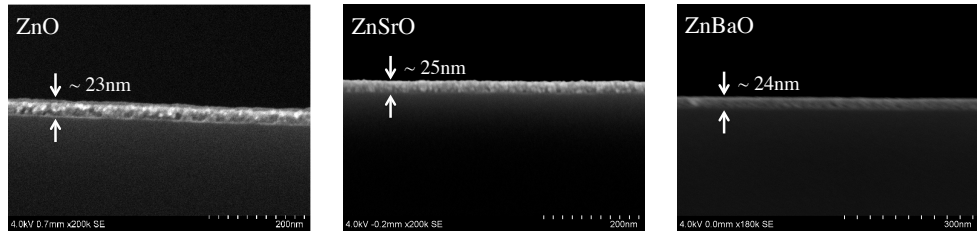


Figure 4.7: SEM cross-sections of cleaved ZnO (left), Zn_{0.97}Sr_{0.03}O (centre) and Zn_{0.97}Ba_{0.03}O (right) films on silicon substrates.

4.2.3 Optical Transmission

Thin films of oxide (25 - 30 nm) on quartz glass substrates were used for optical transmittance measurements to represent the actual transmittance through the

films used in solar cell devices. The transmittance spectra obtained by UV-Vis spectroscopy are shown in figure 4.8. All three films show good visible transparency, $> 95\%$ over the whole visible range 400 - 800 nm, therefore it is valid to assume later on that the factor contributing to the external quantum efficiency of the OPV related with the light intensity and the organic absorption efficiency should be similar for the three types of oxides. The shape of the spectra is similar for all three oxides and the bandgap that is estimated from the transmission edges is at 3.25 eV for ZnO and 3.3 eV for ZnSrO and ZnBaO. These values are used later on to estimate the position of the conduction band (table 4.2). From these results we concluded that there is no significant change in the oxides bandgap with Sr or Ba doping.

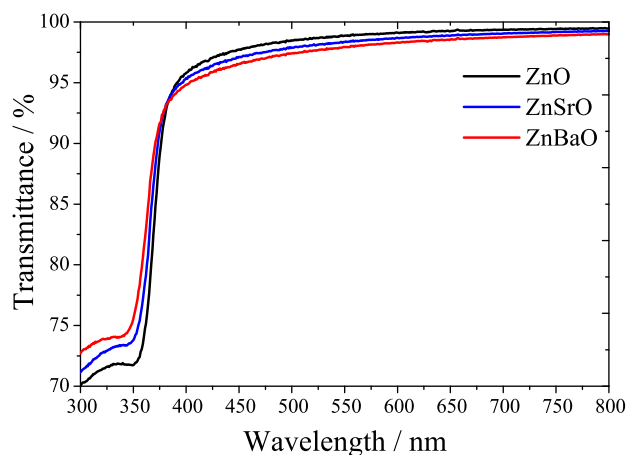


Figure 4.8: Transmittance spectra for ZnO, $\text{Zn}_{0.97}\text{Sr}_{0.03}\text{O}$ and $\text{Zn}_{0.97}\text{Ba}_{0.03}\text{O}$ thin films on quartz glass substrate.

4.2.4 Surface Potentials

As already discussed in section 2.1.2 knowledge of the oxides surface potentials (e.g. ionization potential and fermi level) provides important benchmarks for understanding the nature of doping in transparent conducting oxides. Changes in the ionization potential can be correlated to surface dipoles and hence provide information regarding the oxide surface states while any carrier doping can be identified by a shift in the fermi level. Since these oxides will be serving

as electron extraction layers in OPV the charge injection/extraction and hence performance and stability of the devices will be governed by the organic/oxide interface. Knowledge of the surface properties of the oxides will provide means of interpreting band alignment at the oxide/organic interfaces by understanding the nature of charge injection at the oxide/organic interface (ohmic or schottky) and identifying any injection barriers. In present work, the important surface potentials were measured on thin film specimens by Ultraviolet Photoemission Spectroscopy (UPS).

The obtained UPS spectra for ZnO, ZnSrO and ZnBaO films are shown in figure 4.9. From these spectra it is possible to estimate values for the workfunction (W_F) and the ionisation potential (I_P) (see section 3.3.4 for more detail on how these values can be estimated from the UPS spectra). It can be seen that there is no detectable change in the onset of absorption for the three oxides and hence the workfunction of both the undoped and doped films is equal to $3.6 \text{ eV} \pm 0.1 \text{ eV}$. In figure 4.9 the *valence band offset* at low binding energy (on the right) corresponds to $(E_F - E_{VBM})$ and provides a direct measure of the fermi level at the sample surface which is 3.2 eV for all three films. As a result the ionisation potential ($I_P = W_F + (E_F - E_{VBM})$) remains constant for all films and equal to 6.8 eV .

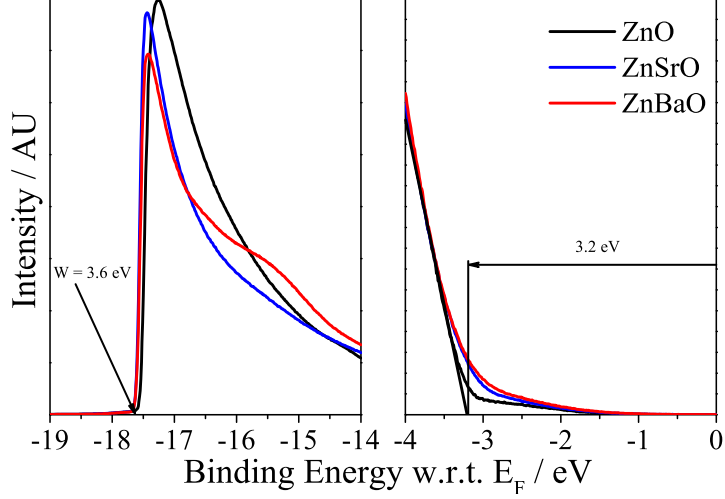


Figure 4.9: UPS spectra for ZnO, $\text{Zn}_{0.97}\text{Sr}_{0.03}\text{O}$ and $\text{Zn}_{0.97}\text{Ba}_{0.03}\text{O}$ thin films on Si substrate with annotated positioning of the onset (denoting the work function) and edge of absorption (denoting the valence band minimum).

Table 4.2 summarises the derived surface potentials and the optical bandgap, estimated from UV-Vis spectroscopy which are used to estimate the position of the conduction band. The conduction band in the case of ZnO coincides (within experimental error) with the position of its fermi level. This behaviour is consistent with the degenerate nature of n-type ZnO. The conduction band of both ZnSrO and ZnBaO is estimated to be 0.05 eV above that of ZnO and 0.1 eV above the fermi level. This shift of the Fermi level further away from the conduction band can be correlated to the small decrease in conductivity measured for the doped films.

Table 4.2: Summary of metal oxides surface potential key parameters.

Metal oxide	W_F / eV	I_P / eV	E_g / eV
ZnO	3.6 ± 0.1	6.8 ± 0.1	3.25 ± 0.05
$\text{Zn}_{0.97}\text{Sr}_{0.03}\text{O}$	3.6 ± 0.1	6.8 ± 0.1	3.30 ± 0.05
$\text{Zn}_{0.97}\text{Ba}_{0.03}\text{O}$	3.6 ± 0.1	6.8 ± 0.1	3.30 ± 0.05

4.2.5 Electrical Conductivity

The electrical conductivity of ZnO, ZnSrO and ZnBaO thin films was determined by means of two-point probe measurements between two planar aluminium electrodes (electrode width $W = 3$ mm, distance $L = 100$ μm) deposited on top of the oxide thin films as described in section 3.3.6. These measurements were performed in order to study any changes in electrical conductivity as well as instabilities with UV light exposure and N_2 annealing discussed earlier (see section 2.1.3) and verify the prediction of a more robust amorphous mixed metal oxide system.

Current-voltage (IV) curves (represented on a semi-log scale) for the three films are compared in figure 4.10, for films measured “as prepared” (annealed at 300°C for 1 hour and stored overnight in ambient air), films that were further annealed at 300°C in N_2 or further exposed to UV light (< 10 mWcm^{-2} , 365 nm). IV characteristics were linear in all cases and the data are represented on a semi-log current voltage scale for convenience. All measurements were carried out in the dark, in a glovebox atmosphere and immediately after UV light exposure or N_2 annealing. It can be seen that the current for all “as prepared” films is low

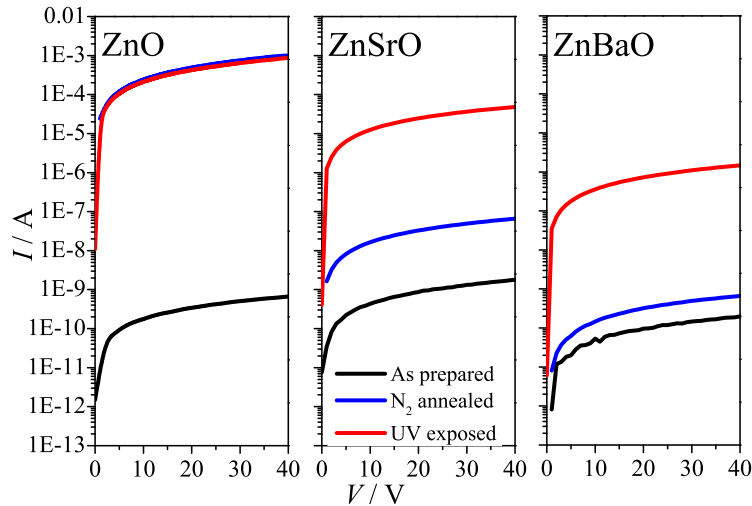


Figure 4.10: Electrical current voltage characteristics for as prepared, N_2 annealed and UV light exposed ZnO, $\text{Zn}_{0.97}\text{Sr}_{0.03}\text{O}$ and $\text{Zn}_{0.97}\text{Ba}_{0.03}\text{O}$ thin films on glass substrate with planar Al source-drain electrodes ($W=3\text{mm}$, $L=100\mu\text{m}$).

and similar within one order of magnitude meaning that the films are intrinsically similar. When the films are measured again after being treated however, the results differ significantly. When ZnO films are N₂ annealed or exposed to UV light the measured current at 40 V increases dramatically by six orders of magnitude. These measurements are in agreement with previous reports on conductivity increase with N₂ annealing or UV light illumination in solution processed ZnO and has been consistently attributed to the de-trapping of electrons induced by the desorption of molecular oxygen from the oxide surface introduced by annealing in a reducing environment or the presence of photogenerated charges.

Using the IV curves and the film thickness we can estimate conductivity values (see section 3.3.6). The conductivity of the ZnO films is significantly enhanced by six orders of magnitude, from ca. $2 \times 10^{-5} \text{ Sm}^{-1}$ to ca. $3 \times 10^{-1} \text{ Sm}^{-1}$ when the film is UV light exposed or post-annealed in N₂. In comparison the ZnSrO and ZnBaO films appear to be less sensitive to these treatments by showing instead an increase of only four and one orders of magnitude with UV light exposure and N₂ annealing respectively. The conductivity for ZnSrO and ZnBaO were estimated as ca. $1 \times 10^{-4} \text{ Sm}^{-1}$ and ca. $5 \times 10^{-6} \text{ Sm}^{-1}$ as prepared, ca. 2 Sm^{-1} and ca. $6 \times 10^{-2} \text{ Sm}^{-1}$ after UV light exposure and ca. $2 \times 10^{-3} \text{ Sm}^{-1}$ and ca. $2 \times 10^{-5} \text{ Sm}^{-1}$ after N₂ annealing respectively.

The effect with UV light was further studied and was observed to be time dependent and non-permanent. The conductivity increased with prolonged UV light exposure and decayed to the initial value on a time-scale dependant on the film composition, the UV exposure time as well as the surrounding environment, when the film was kept in the dark after treatment. This effect, which is referred to as *persistent photoconductivity* (PPC), is the basic mechanism behind sensor systems in the field of transparent conducting oxides. While the oxide is exposed to UV light, photogenerated charges lead to the de-trapping of the trapped electrons and the desorption of oxygen. Immediately after the light is turned off the freed electrons will continue to contribute to the film conductivity, resulting in an increased measured current which will decrease with time as the freed electrons will be trapped again with the re-adsorption of oxygen. Detailed analysis of the kinetics of PPC can provide information regarding the density of surface trap states or the mobility of bulk electrons to the surface. Although the detailed

analysis of PPC was not within the scopes of this experiment, we have carried out IV measurements (in the dark) as a function of time with prolonged UV light exposure as well as recovery in the dark in order to acquire empirical evidence regarding the time-scales and magnitudes of increase and decay in conductivity which were taken into account for later experiments.

The effect of the metal oxide conductivity on device performance was investigated by fabricating devices using metal oxides of varying conductivity by UV light exposing or N₂ annealing the metal oxide films prior to the organic deposition. No correlation was identified between metal oxide conductivity and device performance under short circuit conditions indicating that the bulk conductivity of the metal oxide films does not limit the performance of the OPV devices under these conditions as long as the conductivity is higher than that of the active material. However, the results of this section demonstrate the improved stability of the mixed metal oxide systems with regards to changes with UV light exposure or N₂ annealing as predicted. The origin of this improvement can not be identified at this point and it is discussed later on in section 4.4.

4.3 Device Performance

In this section the device performance of *inverted* OPV with ZnO, ZnSrO and Zn-BaO Electron Extraction Layers is summarized. The EEL is deposited on top of the Indium Tin Oxide (ITO) cathode in order to modify the extraction/injection properties of the cathode. The OPV structure is illustrated in 4.11 and is a typical *inverted* stack of layers where the active organic layer is “sandwiched” between two charge (electron/hole) extraction layers often being transparent conducting oxides. Photogenerated P3HT excitons can separate to charges once they reach a P3HT/PC₆₀BM heterojunction. The resulting free electron/hole is extracted further through the EEL/HEL (ZnO/WO₃). This architecture is well known for the benefit of improved operational stability it offers. Since the aim of this project was to perform a comparative study for the different types of metal oxide EEL (undoped and doped ZnO) it was essential to eliminate any variables arising from other layers. Hence a selection of appropriate materials with extensive pre-existing characterisation were used for the rest layers and their key properties

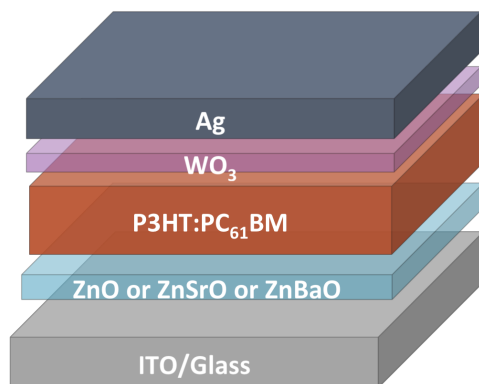


Figure 4.11: Schematic structure of an inverted organic photovoltaic device.

are discussed in see section 3.1 whereas the experimental details for deposition of the different layers are described in section 3.2.

4.3.1 Doping Level

First we optimised the device performance with respect to the doping level of Sr and Ba in the ZnO film to determine an optimum mixing ratio 30:1 ($\sim 3.33\%$ dopant precursor/vol.). In figure 4.12 there is a summary of this study showing the key parameters, obtained from the current density-voltage (J-V) characteristics, measured in ambient air, under 100 mWcm^{-2} AM 1.5G illumination, against volume % for each of the alkaline precursor solution used. For the purposes of this experiment $12 \text{ mm} \times 12 \text{ mm}$ glass substrates covered with ITO (7 mm strip) were used as substrates allowing for eight 4.5 mm^2 devices (pixels) per substrate. The error bars for these measurements were estimated from the standard deviation of measurements taken for 25 working devices out of a total of 32 devices (from four different substrates) for each type of device. It can be seen that there is a small yet notable improvement in power conversion efficiency (PCE) with small doping percentages (3% - 5%) and is mainly attributed to the improvement of the fill factor (FF). At higher doping levels the values for the short circuit (J_{SC}) drop, which is explained by the significant decrease in conductivity (not shown here) of the ZnSrO, ZnBaO films at these levels of doping. In all cases there is no significant change in the open circuit voltage (V_{OC}) with doping. The J-V curves

4.3 Device Performance

for the best performing devices are shown in figure 4.13 with power conversion efficiencies of 3.8%, 3.5% and 3.1% for ZnSrO, ZnBaO and undoped ZnO EELs respectively.

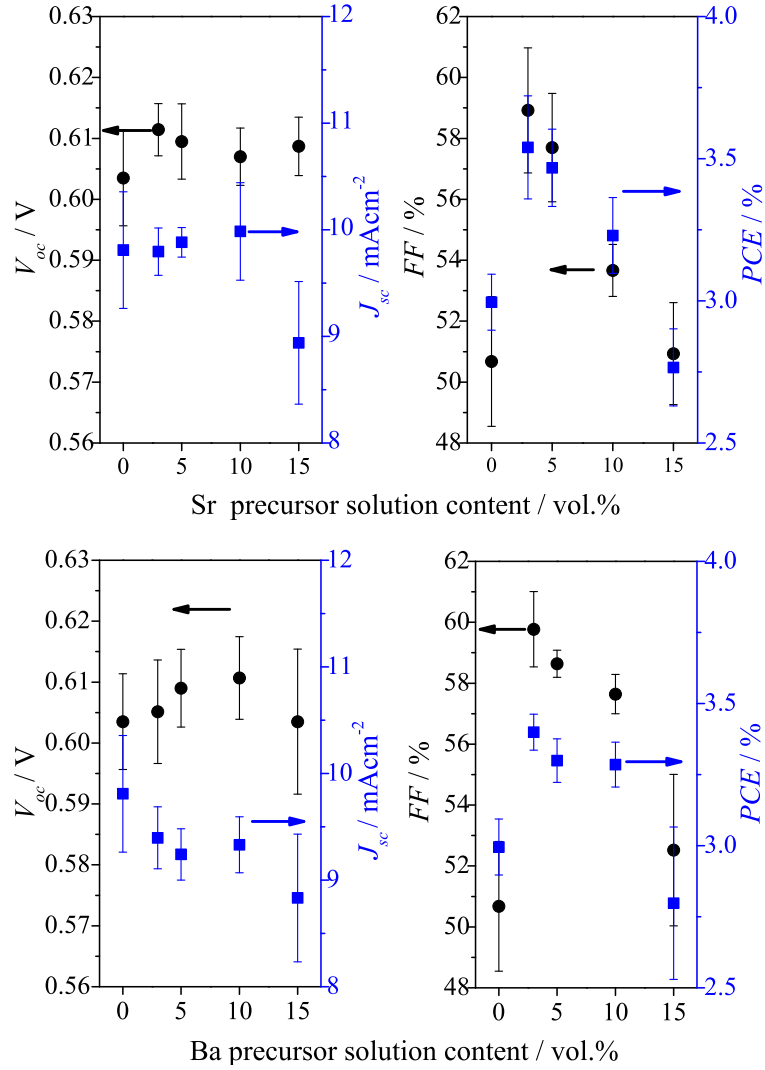


Figure 4.12: V_{OC} , J_{SC} , FF and power conversion efficiency (PCE), under 100 mWcm⁻² AM 1.5G solar simulator conditions, for P3HT:PC₆₀BM inverted OPV devices with a ZnMO EEL against doping % where M is Sr (top) and Ba (bottom). Results for undoped ZnO are obtained from a single batch of devices.

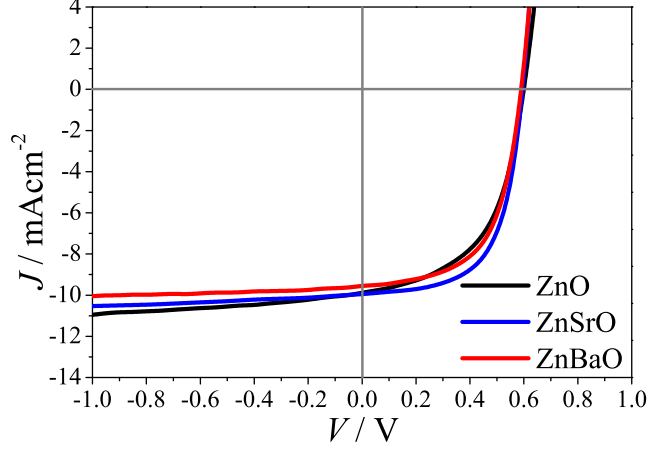


Figure 4.13: J-V curves for best performing devices measured under 100mWcm^{-2} AM 1.5G solar simulator conditions.

4.3.2 EQE Preliminary Measurements

Larger differences in performance and stability became apparent when performing external quantum efficiency (EQE) measurements of devices, performed at much lower light intensity. Given the sensitivity to light exposure and/or voltage bias of OPV devices with a solution processed ZnO EEL we had to establish an experimental procedure that would minimise any systematic errors and avoid the misinterpretation of changes in EQE. In order to do so we performed EQE preliminary measurements the results of which are shown in figure 4.14. In these measurements the (i) the UV monochromatic light used during an EQE spectrum scan and (ii) the forward DC bias applied during a IV measurement are shown to increase in both cases the EQE. Taking EQE measurements including wavelengths $< 400\text{ nm}$ and/or taking IV measurements where voltage $> +2\text{ V}$ is applied leads to an increase ($\sim \times 6$) in the EQE%. This is thought to be due to charge de-trapping effects happening with the introduction of photogenerated holes upon UV light absorption or at higher forward bias with hole injection. To eliminate these effects it was made sure that EQE spectra were taken above 500 nm and in-between IV measurements were taken by applying maximum 1 V forward.

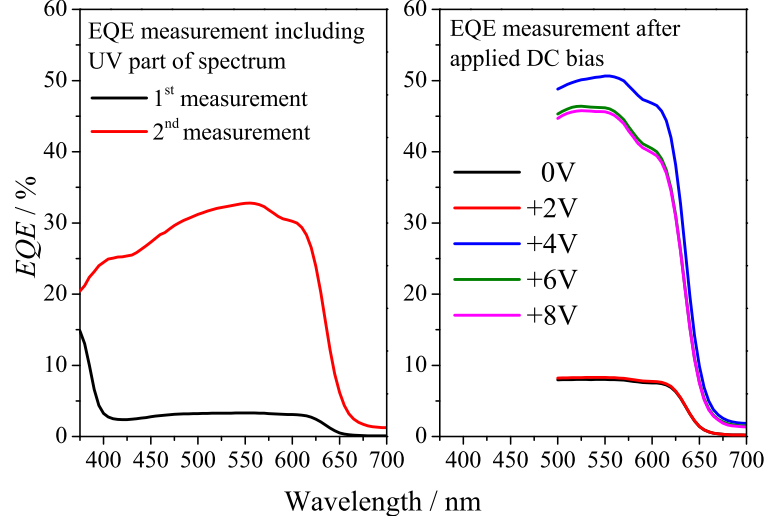


Figure 4.14: The effect of (left) UV monochromatic light during an EQE measurement and (right) forward bias on EQE measurements.

4.3.3 UV Light Exposure and Nitrogen Annealing

Here dependence of device performance and stability (EQE and IV characteristics) on different treatments such as light illumination and annealing in N_2 atmosphere is investigated. OPV where the oxide film was used “as prepared” or annealed in nitrogen just before the deposition of the organic film was carried out were fabricated. Some devices were post treated by exposing to light at a particular region of the solar simulator spectrum. In order to achieve this, two different filters were used: a long pass filter at 495 nm and a band pass UV filter at 275 nm - 375 nm. In figure 4.15 the dependence of the EQE of devices measured on light exposure (top) and annealing in N_2 atmosphere (bottom) is shown.

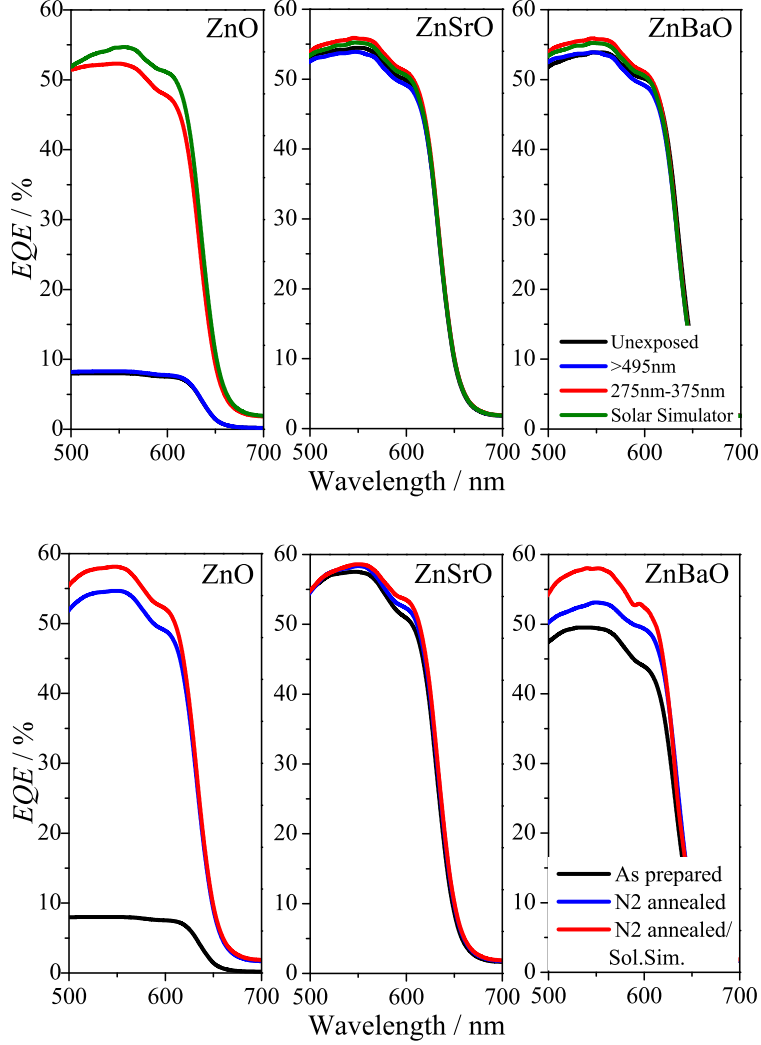


Figure 4.15: External quantum efficiency (EQE) characteristics before and after light exposure (top) and with annealing in N_2 atmosphere (bottom) of devices with ZnO, $Zn_{0.97}Sr_{0.03}O$ and $Zn_{0.97}Ba_{0.03}O$ EELs.

In figure 4.15 (top) results for devices measured : (i) before light exposure, (ii) after first being exposed to the visible part, (iii) then to the UV part and (iv) eventually to the full solar simulator spectrum are given. It can be seen that the performance for an unexposed pure ZnO device is extremely poor with maximum EQE as low as $\sim 10\%$. Only after UV illumination the device shows

4.3 Device Performance

a five-fold performance increase to an EQE of 50% - 55%. In contrast devices with ZnSrO or ZnBaO EEL show already maximum performance (EQE~ 55%) before any light treatment and exhibit only minor changes after light illumination. The behaviour is very similar when films are subjected to an additional 10 minute annealing step at 300⁰C in a glovebox nitrogen atmosphere (figure 4.15(bottom)). These measurements show clearly that by using alkaline earth doped EELs it is possible to overcome the need for light-soaking ZnO-based OPV before a high performance can be achieved.

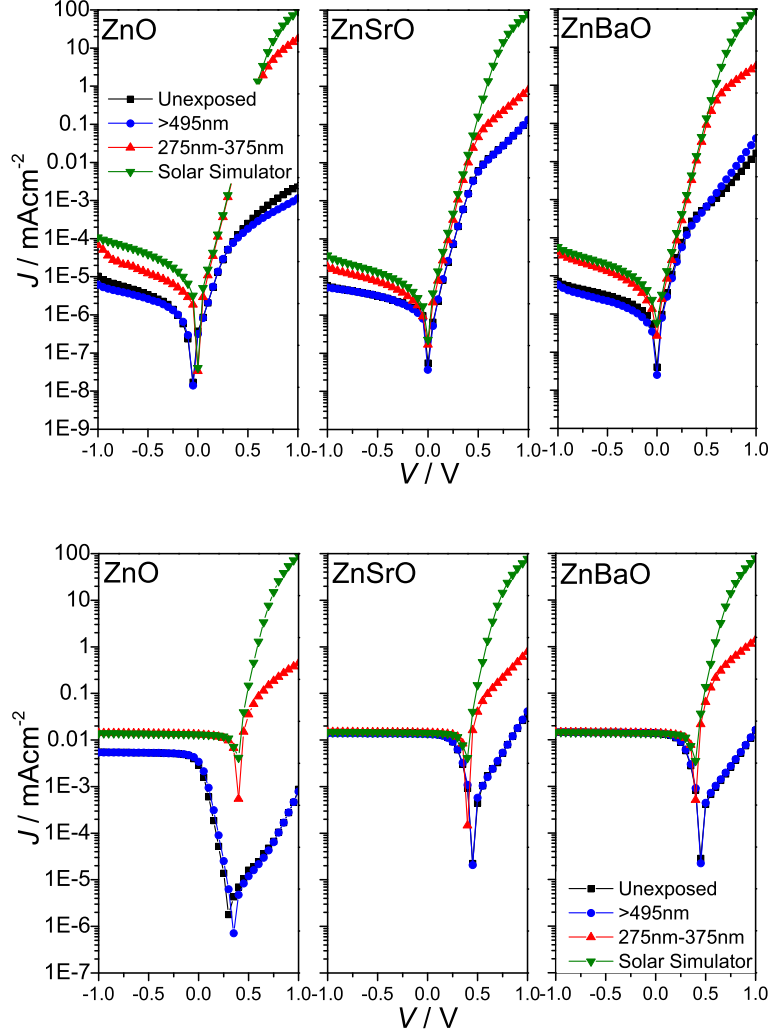


Figure 4.16: Current density - voltage characteristics in the dark (top) and under 580nm monochromatic illumination before and after light exposure of devices with ZnO, $\text{Zn}_{0.97}\text{Sr}_{0.03}\text{O}$ and $\text{Zn}_{0.97}\text{Ba}_{0.03}\text{O}$ EELs (corresponding to figure 4.15 top figure).

The current density-voltage (J-V) measurements in the dark and under monochromatic light exposure for films with different illumination histories are shown in figures 4.16(top) and (bottom) respectively. The unexposed ZnSrO and ZnBaO devices have better diode dark characteristics with higher rectification ratio by

two and one orders of magnitude respectively, in comparison to unexposed ZnO devices. The short circuit current (J_{SC}) for the unexposed ZnO device is measured as $\sim 0.003 \text{ mAcm}^{-2}$ whereas for exposed ZnO as well as unexposed/exposed ZnSrO, ZnBaO as $\sim 0.014 \text{ mAcm}^{-2}$ which corresponds to the five-fold increase observed in the EQE. Although the J_{SC} and current under reverse bias are independent of light illumination for the ZnSrO and ZnBaO devices the current under forward bias does improve upon UV light illumination. The reason for this could be that the current at higher carrier densities (i.e. current under forward bias) is either limited by the low conductivity of the metal oxide films before UV illumination and/or that there exists a finite injection barrier for the doped ZnO devices similar to the undoped ZnO devices that becomes limiting at higher carrier densities.

4.4 Improvement Mechanism

In this section we discuss more detailed investigations of the bulk and interfacial oxide electronic structure as well as device operation, before and after UV light exposure, in order to better understand the mechanism for the observed improved stability and performance of the doped films. The band alignment for the oxide/organic interface and the chemical composition of the films with UV light exposure are investigated by means of Ultraviolet and X-ray photoemission spectroscopy respectively. The effective OPV device built-in field is also taken into account and it is used to identify an interfacial dipole between the oxide and the organic which limits the performance for the undoped ZnO EEL OPV. The built in field is estimated by means of electroabsorption Spectroscopy and compared for the three types of oxides upon UV light exposure. Finally we present electrical hysteresis measurements, typically used for memristor devices, to discuss the effect doping has on the oxide surface trap states and how this leads to more stable OPV.

4.4.1 Interfacial Band Alignment

It is known that electron-injecting materials such as ZnO have the ability to decrease the electron-injection barrier at cathode/organic interfaces as a result of the oxide's ability to increase the molecule's electron-orbital binding energies, thus lowering the lowest unoccupied molecular orbital (LUMO). Ultraviolet pho-

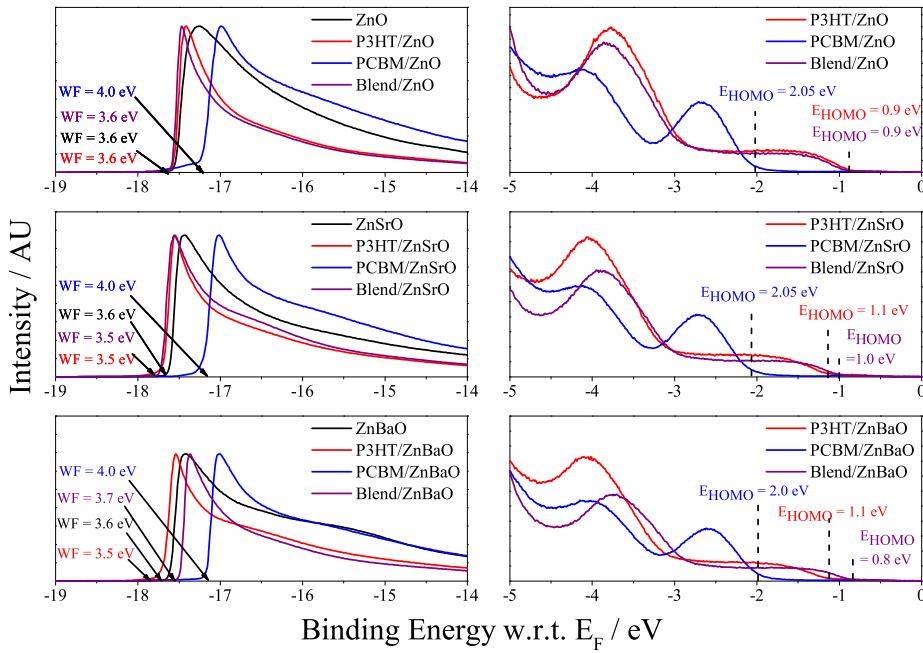


Figure 4.17: (top) UPS spectra for ZnO, ZnO/P3HT, ZnO/PC₆₀BM and ZnO/blend, (middle) UPS spectra for Zn_{0.97}Sr_{0.03}O, Zn_{0.97}Sr_{0.03}O/P3HT, Zn_{0.97}Sr_{0.03}O/PC₆₀BM and Zn_{0.97}Sr_{0.03}O/blend and (bottom) UPS spectra for Zn_{0.97}Ba_{0.03}O, Zn_{0.97}Ba_{0.03}O/P3HT, Zn_{0.97}Ba_{0.03}O/PC₆₀BM and Zn_{0.97}Ba_{0.03}O/blend where blend is P3HT:PC₆₀BM

toemission spectroscopy (UPS) was used to compare this ability for the three types of oxides and relate to the improvements in device performance before UV light exposure. UPS spectra were collected under ultra high vacuum (UHV) conditions, on oxide/organic bilayer samples: ZnMO/P3HT, ZnMO/PC₆₀BM and ZnMO/P3HT:PC₆₀BM, where M = nothing in the case of undoped ZnO, Sr or Ba and are summarized on figure 4.17. The relevant parameters of energy level

4.4 Improvement Mechanism

alignment, oxide workfunction (W_F) and organic ionisation energy (IE_{org}) extracted from UPS spectra are summarised in table 4.3 (see section 3.3.4 for detail on the UPS technique and parameter extraction). The results obtained for organic films prepared on undoped ZnO (figure 4.17(top)) are in good agreement with what has been previously measured for organics on electron injecting substrates. The WF of the bare ZnO substrate is 3.6 eV (results shown in section 4.2.4) and remains unchanged upon P3HT deposition. Therefore, vacuum level alignment (refer to figure in theory) was perceived at the ZnO/P3HT interface. Moreover the IE_{org} is around 4.5 eV, in agreement with the value of P3HT reported by Osikowicz *et al.*³¹ Upon PC₆₀BM deposition on the ZnO substrate the effective WF measured was 4.0 eV indicating fermi level pinning. The UPS spectrum for the case of the blend, ZnO/P3HT:PC₆₀BM is completely dominated by the P3HT features implying a $\sim 1 - 2$ nm P3HT rich layer near the top surface. This has been previously observed in the case of P3HT:PC₆₀BM films and is attributed to the lower surface energy of P3HT.^{32,33}

Table 4.3: Summary of metal oxide/organic interface band alignment key parameters.

Sample	WF / eV	IE_{org} / eV
P3HT/ZnO	3.6 ± 0.1	4.5 ± 0.1
P3HT/ZnSrO	3.5 ± 0.1	4.6 ± 0.1
P3HT/ZnBaO	3.5 ± 0.1	4.6 ± 0.1
PCBM/ZnO	4.0 ± 0.1	6.0 ± 0.1
PCBM/ZnSrO	4.0 ± 0.1	6.0 ± 0.1
PCBM/ZnBaO	4.0 ± 0.1	5.9 ± 0.1
P3HT:PCBM/ZnO	3.6 ± 0.1	4.5 ± 0.1
P3HT:PCBM/ZnSrO	3.5 ± 0.1	4.5 ± 0.1
P3HT:PCBM/ZnBaO	3.7 ± 0.1	4.5 ± 0.1

Comparing the results for undoped and doped ZnO there is no significant variation (within experimental error) in the UPS spectra shape and estimated values for WF and IE_{org} . This comes in line with the very similar energetics measured

earlier for the bare oxide films. We will find later on that this contradicts our findings of a different interfacial band-bending at the oxide/blend interface between the doped and undoped ZnO. This could be as result of the fact that UPS measurements were performed under unrealistic conditions for device operation and hence might not represent the “as prepared” films used in devices. UHV conditions along with UV light exposure during a UPS scan, might favour the desorption of oxygen from the oxide surface in a much more efficient way than what we have measured in atmospheric pressure conditions. Thus, from these results we can only conclude that under UHV conditions, undoped and doped ZnO and the interfaces they form with P3HT and PC₆₀BM are identical within experimental error of UPS (0.2 eV).

4.4.2 Chemical Composition Stability

The chemical composition of the metal oxides was monitored as a function of UV exposure by monitoring the chemical shift in the XPS O1s core level. UV light was shone on the sample in situ during the XPS measurements by shining UV light from near-UV emitter ($\sim 1 \text{ mWcm}^{-2}$, 375 nm - 405 nm LED) onto the sample through a viewport of the UHV chamber. In all films the O1s peak is a broad peak around 531 eV with pronounced fine structure indicating multiple oxygen environments as shown in figure 4.18. The peak was de-convoluted into two Gaussian components with variable full-widths at half maximum (FWHMs), intensities and positions centred around 530.4 eV and 532.2 eV reflecting two different oxygen environments. On the basis of reported binding energies³⁴ we attribute the peak at 530.4 eV to lattice oxygen atoms in a fully coordinated environment (Zn-O) and the peak at 532.2 eV to oxygen species bound to the surface in the form of adsorbed molecular O₂, H₂O or metal hydroxide species. In some cases the deconvolution to three peaks, including an additional peak attributed to oxygen atoms in the vicinity of an oxygen vacancy and centred at 531 eV, has been reported. Attempts to resolve the O1s peak with all three bands resulted in similar quality fits and in some cases poorer fits, for this reason we present the two band fit instead.

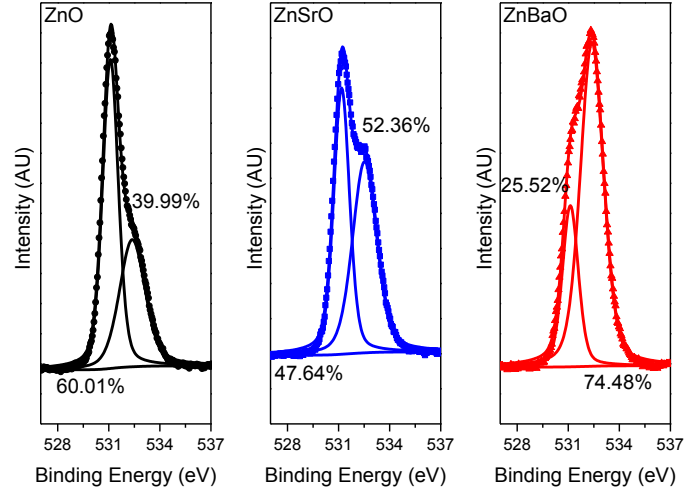


Figure 4.18: Comparison of O1s scan for ZnO, $\text{Zn}_{0.97}\text{Sr}_{0.03}\text{O}$ and $\text{Zn}_{0.97}\text{Ba}_{0.03}\text{O}$ thin films.

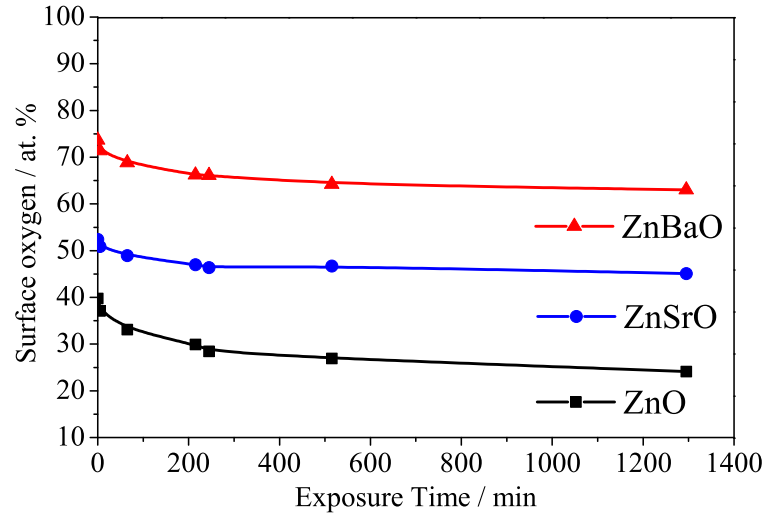


Figure 4.19: Surface oxygen % content with respect to the O1s XPS scans with prolonged UV light ($\sim 1 \text{ mWcm}^{-2}$, 375 - 405 nm) exposure time for ZnO, $\text{Zn}_{0.97}\text{Sr}_{0.03}\text{O}$ and $\text{Zn}_{0.97}\text{Ba}_{0.03}\text{O}$ thin films.

In figure 4.19 the atomic percentage of the surface oxygen contribution to the total O1s peak with UV light exposure time is given. The surface oxygen%

decreases with UV exposure time. This decrease can be considered as the superposition of two decay processes: a fast drop in the first 100 minutes and a slower decay for the next 1000 minutes reaching saturation. In order to identify in more precision (to overcome the ambiguity of the fitting peaks) the particular energy of the species the contribution of which is being affected by UV light we subtracted the normalised XPS spectra before and after exposure. An example of this differential spectrum which was of similar shape for all oxides is shown in figure 4.20 (ZnSrO only). The resulting spectrum was as expected a peak centred at 532 eV towards the high energy end of the spectrum, verifying the desorption of surface oxygen species with UV light exposure. It should be noted here that the dependence of the O1s peak composition with time in the absence of UV light has not been recorded for similar time-scales and the possibility of UHV aided desorption of oxygen species in the dark cannot be excluded. However from empirical evidence we know that there is no notable change in the O1s spectrum during two subsequent measurements in the absence of UV light. The course of a full scan usually ranges from 5 to 10 minutes. The fact that with UV light exposure there is already a $>5\%$ change in the first five minutes supports the interpretation based on UV assisted desorption.

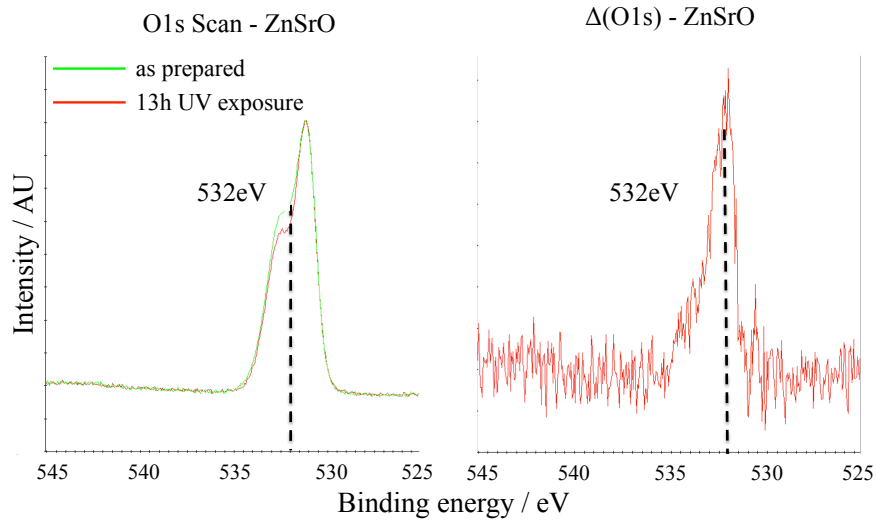


Figure 4.20: Change in O1s scan after 13h UV exposure for $\text{Zn}_{0.97}\text{Sr}_{0.03}\text{O}$ film.

Although the surface oxygen % is smaller for the unexposed ZnO film (40%) compared to unexposed ZnSrO (55%) and ZnBaO (75%) it shows a larger change in surface oxygen%, of 16% after a time exposure of 1300 minutes, compared to 7% and 10% for ZnSrO and ZnBaO respectively. The decrease in surface oxygen% with UV exposure is considered to be due to desorption of adsorbed molecular oxygen species on the oxide surface with the induction of positive photo-generated charges.^{35,36} This result is in agreement with electrical conductivity increase with UV light exposure since surface adsorbed molecular oxygen acts as an electron trap and its desorption donates an electron to the conduction band, hence increasing conductivity. The smaller change in surface oxygen% for the doped films can be correlated as well to their decreased sensitivity in electrical conductivity with UV.

4.4.3 Built-in Potential

Furthermore, we carried out electroabsorption (EA) spectroscopy measurements to characterise the built-in potential (V_{bi}) in the devices (see section 3.4.2 for more detail and preliminary measurements). In theory the V_{bi} in an OPV mainly originates from the difference of workfunction of the two electrodes³⁷. A reduced effective V_{bi} might result due to screening effects in the presence of interfacial dipoles (see section 2.3.2). Figure 4.21 shows the magnitude of the first harmonic EA response at 2.0 eV as a function of external bias for ZnO, ZnSrO and ZnBaO OPV devices before and after UV exposure. From 3 V to 1 V, the signal decreases linearly with dc offset, which is consistent with the classical EA theory, as indicated in equation ???. From the voltage axis intercept of the linear fit to the EA response in reverse bias we can determine the built-in field. The values of the built-in field for unexposed devices were estimated to be ~ 0.5 V for ZnO and ~ 1.5 V for ZnSrO or ZnBaO EELs; and 2 V, 2.3 V and 2.7 V respectively, after UV exposure. When further increasing the dc offset to the positive regime, the EA signal of all three devices deviates from the linear relationship. This is most likely due to charge injection from the Ag electrode in forward bias and the associated excited state bleaching and absorption (ESBA).³⁸ Brown *et al.* also observed a similar behaviour in P3HT devices in the high charge accumulation

region, which results from the polaronic charge carrier injected in the device.^{39,40}

Before UV illumination, for the pure ZnO, which is an n-type semiconductor due to doping by oxygen vacancies, it is generally accepted that mobile electrons can be trapped by gas molecules adsorbed on the surface.⁴¹ Particularly, in ambient atmosphere, both surface adsorbed water and oxygen molecules play a crucial role in the trapping of charges at the interface between ZnO and the active layer.⁴² This phenomenon has been observed previously and allows for a diversity of applications such as gas sensor,⁴³ resistive switching device⁴³ and ultra-fast UV detector.⁴⁴ The interfacial layer formed by the combination of gas molecule and trapped electrons introduces a depletion of mobile electrons in the ZnO and an upward band bending in the ZnO film towards the interface with the active layer.⁴⁴ The associated potential barrier decreases the built-in potential across the device (measured 0.5 V), which should be as large as the difference of workfunctions between ZnO and WO₃, i.e. around 2.0 eV. The negative trapped charge on the surface of the ZnO may also reduce the collection efficiency for electrons through ZnO to the ITO electrode and result in a reduced short circuit current. After UV illumination, the introduction of positive charges via creation

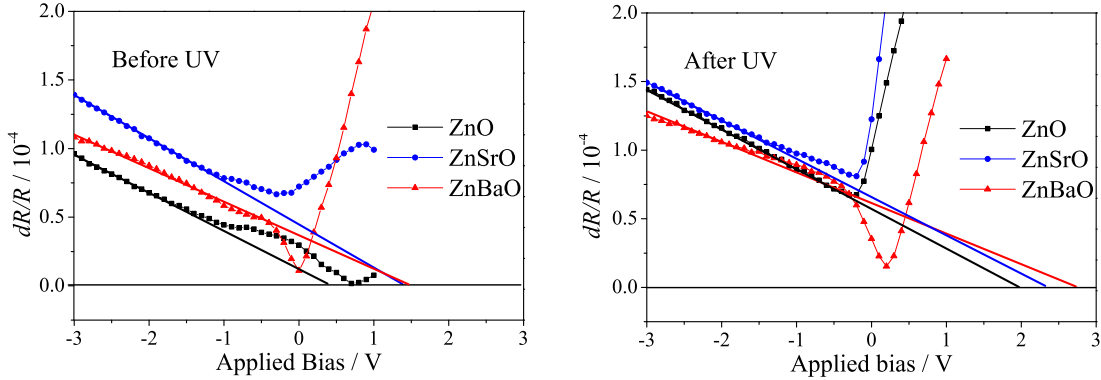


Figure 4.21: Electroabsorption (EA) response measurements of OPV with ZnO, Zn_{0.97}Sr_{0.03}O and Zn_{0.97}Ba_{0.03}O as EEL, before (left) and after (right) UV light exposure. The built-in potential V_{bi} is determined from the extrapolation of the linear regime in reverse bias (+ applied bias).

of electron hole pairs induces desorption of the gas molecules at the interface. This releases mobile electrons into the ZnO conduction band resulting in the observed

dramatic increase in conductivity and reduction of the band bending at the interface. Consequently, the effective internal field increases as observed and becomes more comparable to the pure work function difference between ZnO and WO₃ (measured 2.0 V). The performance of the device, including the J_{SC} , EQE as well as PCE improves due to the decrease of bi-molecular recombination in the high internal field. The internal field of devices with doped ZnSrO or ZnBaO is less influenced by the UV irradiation. Before UV exposure, the built-in voltage of 1.5 V is already close to the optimum value.

The atomistic mechanism, by which Sr and Ba incorporation brings about this improvement, remains speculative at present and requires more detailed investigations and theoretical simulations. Alkaline earth metals, such as Sr and Ba, have high affinity towards oxygen and may act similarly to Ga in InGaZnO as to reduce the concentration of oxygen vacancies in the films, which act as trap sites for adsorbed molecular oxygen on the surface. It is also possible that there are several types of oxygen vacancies, one of which is effectively prevented by alkaline earth doping. Finally, we note that after UV illumination the built-in fields of all three devices increase. The likely reason for this behaviour is that UV light generates a large concentration of mobile charge electrons in ZnO, which changes the Fermi level of the device towards the conduction band. Hence, the internal field, i.e. difference of work functions, increases.

4.4.4 Electrical Hysteresis

Further evidence for the improved electrical stability imparted by Sr/Ba doping was observed in electrical current-voltage experiment on OPV devices.

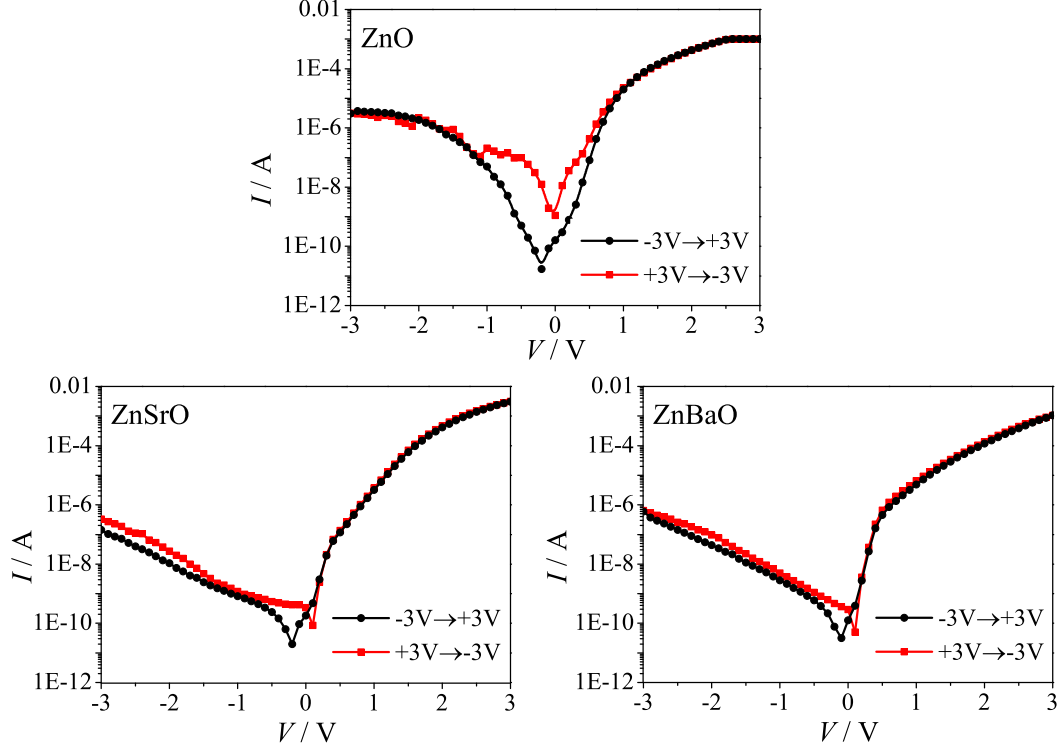


Figure 4.22: Dark current-voltage characteristics of OPV devices in air. First a sweep was carried out starting from reverse bias (-3 V to +3 V) and then a reverse scan was measured starting from forward bias (+3 V to -3 V).

In figure 4.22 dark current-voltage characteristics of OPV devices in which the direction of applied voltage sweep is varied are shown. It can be seen that the significant electrical hysteresis observed for ZnO EEL is reduced in the case of doped ZnO further demonstrating the improved electrical stability of the amorphous mixed metal oxides. The origin of the hysteresis in the device with a ZnO EEL can be attributed to a charge de-trapping process during the sweep. When the sweep is initially carried out from reverse bias, the device is at a high resistance mode in agreement with poor built-in potential and low EQE (for surface oxygen rich ZnO) measured earlier. On the second sweep from forward bias the device reaches a low resistance mode, in agreement with improved EQE with positive bias (figure 4.14) as surface oxygen is desorbed due to hole injection and the built-in potential is increased.

4.5 Conclusions

Ternary metal oxides, ZnSrO and ZnBaO, fabricated by sol-gel deposition using alkoxide molecular precursor solutions at relatively low temperature have been shown to provide stable, transparent electron extraction layers for inverted organic solar cells with higher performance and stability than pure ZnO. Using these materials the common problem of the need for light soaking before maximum external quantum efficiency is achieved is circumvented and the overall power conversion efficiency is improved. We attribute this to the incorporation of alkaline earth metals reducing electron trapping on the surface associated with oxygen adsorption, which in pure ZnO leads to band bending in the ZnO film towards the interface and an associated reduction in the built-in electric field. Alkaline earth doping reduces the interfacial band bending in the oxide and increases the built-in field. Our results suggest that like in TFT applications, where materials like InGaZnO are rapidly becoming an important technology, the use of amorphous, mixed metal oxides allows improving the performance and stability of interfacial charge extraction/ injection layers in organic photovoltaics and potentially organic light emitting diodes. Our metal alkoxide based sol-gel approach provides a convenient approach to realizing a wide range of ternary or even quaternary oxides and is also potentially compatible with processing on plastic substrates.

References

- [1] Jorgensen, M., Norrman, K., Gevorgyan, S.A., Tromholt, T., Andreasen, B., and Krebs, F.C. (2012) *Advanced Materials*, **24**, 580. 68
- [2] Gilot, J., Wienk, M.M., and Janssen, R.A.J. (2007) *Applied Physics Letters*, **90**, 143512. 68
- [3] Steim, R., Choulis, S.A., Schilinsky, P., and Brabec, C.J. (2008) *Applied Physics Letters*, **92**, 093303. 68
- [4] Kim, C.S., Lee, S.S., Gomez, E.D., B., K.J., and Loo, Y.L. (2009) *Applied Physics Letters*, **94**, 113302. 68

-
- [5] Sista, S., Park, M.H., Hong, Z., Wu, Y., Hou, J., Kwan, W.L., Li, G., and Yang, Y. (2010) *Advanced Materials*, **22**, 380. 68
- [6] Schmidt, H., Zilberberg, K., Schmale, S., Flügge, H., Riedl, T., and Kowalsky, W. (2010) *Applied Physics Letters*, **96**, 243 305. 68
- [7] Kim, J., Kim, G., Choi, Y., Lee, J., Heum Park, S., and Lee, K. (2012) *Journal of Applied Physics*, **111**, 114511. 68
- [8] Kyaw, A.K.K., Sun, X.W., Jiang, C.Y., Lo, G.Q., Zhao, d.W., and Kwong, D.L. (2008) *Applied Physics Letters*, **93** (221107). 68
- [9] Beek, W.J.E., Sloof, L.H., Wienk, M.M., Kroon, J.M., and Janssen, R.A.J. (2005) *Advanced Functional Materials*, **15**, 1703. 68
- [10] Hau, S.K., Yip, H.L., Baek, N.S., Zou, J., O'Malley, K., and Jen, A.K.Y. (2008) *Applied Physics Letters*, **92**, 253 301. 68
- [11] Hau, S.K., Yip, H.L., Ma, H., and Jen, A.K.Y. (2008) *Applied Physics Letters*, **93**, 233 304. 68
- [12] Manor, A., Katz, E.A., Tromholt, T., and Krebs, F.C. (2011) *Advanced Energy Materials*, **1**, 836. 68
- [13] Verbakel, F., Meskers, S.C.J., and Janssen, R.A.J. (2006) *Applied Physics Letters*, **89**, 102 103. 68
- [14] Verbakel, F., Meskers, S.C.J., and Janssen, R.A.J. (2007) *Journal of Applied Physics*, **102**, 083 701. 68
- [15] Wang, J., Sun, B., Gao, F., and Greenham, N.C. (2010) *Phys. Status Solidi A*, **207**, 484. 68
- [16] Kyaw, A.K.K., Wang, Y., Zhao, D.W., Huang, Z.H., Zeng, X.T., and Sun, X.W. (2011) *Phys. Status Solidi A*, **208**, 2635. 69
- [17] Banger, K.K., Yamashita, Y., Mori, K., Peterson, R.L., Leedham, T., Rickard, J., and Sirringhaus, H. (2011) *Nature Materials*, **10**, 45–50. 69

REFERENCES

- [18] Hung, L.S., Tang, C.W., and Mason, M.G. (1997) *Applied Physics Letters*, **70**, 152. 69
- [19] Fujikawa, H., Mori, T., Noda, K., Ishii, M., Tokito, S., and Taga, Y. (2000) *J. Lumin.*, **87-89**, 1177. 69
- [20] Yang, X., Mo, Y., Yang, W., Yu, G., and Cao, Y. (2001) *Applied Physics Letters*, **79**, 563. 69
- [21] Huang, J., Li, G., Wu, E., Xu, Q., and Yang, Y. (2006) *Advanced Materials*, **18**, 114. 69
- [22] Vaynzof, Y., Kabra, D., Chua, L.L., and Friend, R.H. (2011) *Applied Physics Letters*, **98**, 113 306. 69
- [23] Wakimoto, T., Fukuda, Y., Nagayama, K., Yokoi, A., Nakada, H., and Tsuchida, M. (1997) *IEEE Trans. Electron. Devices*, **44**, 1245. 69
- [24] Zhou, D.Y., Cai, S.D., Gu, W., Liao, L.S., and Lee, S.T. (2010) *Applied Physics Letters*, **97**, 223 302. 69
- [25] Lu, L.P., Kabra, D., and Friend, R.H. (2012) *Advanced Functional Materials*, **22**, 4165. 69
- [26] Banger, K.K., Peterson, R.L., Mori, K., Yamashita, Y., Leedham, T., and Sirringhaus, H. (2014) *Chem. Mater.*, **26**, 1195. xix, 70
- [27] Inamdar, A.I., Mujawar, S.H., Barman, S.R., Bhosale, P.N., and Patil, P.S. (2008) *Semicond. Sci. Technol.*, **23**, 085 013. 72
- [28] Young, V. and Otagawa, T. (1985) *Applications of Surface Science*, **20**, 228. 72
- [29] Ozensoy, E., Peden, C.H.F., and Szanyi, J. (2006) *Journal of Physical Chemistry B*, **110**, 17 009. 72
- [30] Sessolo, M., Bolink, H., Brine, H., Garcia, H.P., and Zaera, R.T. (2012) *J. Mater. Chem.*, **22**, 4916. 76

-
- [31] Osikowicz, W., de Jong, M.P., and Salaneck, W.R. (2007) *Advanced Materials*, **19**, 4213. 93
- [32] Campoy-Quiles, M., Ferenczi, T., Agostinelli, T., Etchegoin, P.G., Kim, Y., Anthopoulos, T.D., Stavrinou, P.N., Bradley, D.C., and Nelson, J. (2008) *Nature Materials*, **7**, 158. 93
- [33] McNeill, C.R., Halls, J.J.M., Wilson, R., Whiting, G.L., Berkebile, S., Ramsey, M.G., Friend, R.H., and Greenham, N.C. (2008) *Advanced Functional Materials*, **18**, 2309. 93
- [34] Fan, J.C.C. and Goodenough, J.B. (1977) *Journal of Applied Physics*, **48**, 3524. 94
- [35] Major, S., Kumar, S., Bhatnagar, M., and Chopra, K.L. (1986) *Applied Physics Letters*, **49**, 394. 97
- [36] Du Ahn, B., Hoon Oh, S., Hee Lee, C., Hee Kim, G., Jae Kim, H., and Yeol Lee, S. (2007) *J. Cryst. Growth*, **309**, 128. 97
- [37] Campbell, I.H., Hagler, T.W., Smith, D.L., and Ferraris, J.P. (1996) *Physical Review Letters*, **76**, 1900. 97
- [38] Brewer, P.J., Lane, P.A., deMello, A.J., Bradley, D.D.C., and deMello, J.C. (2004) *Advanced Functional Materials*, **14**, 562. 97
- [39] Brown, P.J., Sirringhaus, H., and Friend, R.H. (1999) *Synth. Met*, **101**, 557. 98
- [40] Sirringhaus, H., Brown, P.J., Friend, R.H., Nielsen, M.M., Bechgaard, K., Langeveld-Voss, B.M.W., Spiering, A.J.H., Janssen, R.A.J., Meijer, E.W., Herwig, P., and de Leeuw, D.M. (1999) *Nature*, **401**, 685. 98
- [41] Collins, R. and Thomas, D. (1958) *Physical Review*, **112**, 388. 98
- [42] de Leeuw, D.M., Simenon, M.M.J., Brown, A.R., and Einerhand, R.E.F. (1997) *Synth. Met*, **87**, 53. 98

REFERENCES

- [43] Wang, J.X., Sun, X.W., Yang, Y., Huang, H., Lee, Y.C., Tan, O.K., and Vayssieres, L. (2006) *Nanotechnology*, **17**, 4995. 98
- [44] Jin, Y., Wang, J., Sun, B., Blakesley, J.C., and Greenham, N.C. (2008) *Nano Letters*, **8**, 1649. 98

Chapter 5

Interfacial Modification for Oxide/Polymer Hybrid Photovoltaics

In chapter 4 we have demonstrated how the use of amorphous mixed metal oxides, ZnSrO and ZnBaO can lead to better performing OPV devices due to a more efficient oxide/organic interface¹. The question whether similar benefits could also be achieved in oxide/organic hybrid photovoltaic devices arises. Photoinduced charge separation at hybrid organic/inorganic interfaces is poorly understood and challenging to control. Here we investigate charge separation at a model system of ZnO/P3HT and employ Sr doping of ZnO and PCBA self-assembled modification to study and enhance the charge separation efficiency. We find that doping alone, lowers the efficiency of charge separation due to the introduction of defect states at the oxide surface. However, with the combination of doping and molecular modification, charge separation efficiency is significantly enhanced due to the passivation of interfacial traps and improved modifier coverage.¹

¹Part of work discussed in this chapter has been carried out in close collaboration with Dr. Yana Vaynzof and has been published in: “*Improved Performance of ZnO/Polymer Hybrid Photovoltaic Devices by Combining Metal Oxide Doping and Interfacial Modification*” O. Pachoumi, A.A. Bakulin, A. Sadhanala, H. Sirringhaus, R. H. Friend and Y. Vaynzof, *J. Phys. Chem. C* 118, 18945-18950 (2014)

5.1 Introduction

Hybrid organic-inorganic photovoltaic devices have drawn significant interest from the scientific community due to the possibility to utilise the advantages of both organic and inorganic materials. Typically, these devices consist of a conjugated polymer as a donor material and a metal oxide as the electron acceptor. The metal oxide acceptor can be easily processed and form a variety of nano structures.^{2,3,4,5} The organic counterpart can be then introduced to back fill a nano structure or to form a bilayer with a planar oxide layer. Upon photoexcitation, an exciton, created at the donor polymer chain diffuses to the organic-inorganic interface, where charge separation can occur. The hole will remain in the donor polymer forming a polaron and the electron will be transferred to the acceptor metal oxide. Photo-induced charge separation at hybrid organic-inorganic interfaces is poorly understood and challenging to control.

Recently, we have reported in our group that in the model ZnO/P3HT system, over half of the excitations result in bound charge pairs.⁶ These electron-hole pairs arise from trapping of the electron at a surface state of the metal oxide, which in turn Coulombically attracts the hole polaron on the polymer chain.⁷ Vaynzof *et al.* and others demonstrated that interfacial modifiers can be used to functionalise the oxide surface in order to enhance charge separation at the interface.^{8,9,10,11} Alternatively, doping of the metal oxide has also been reported as a possible means to improve photovoltaic device performance¹. In this chapter we combined these two approaches. We incorporate into the hybrid PV configuration; one of the novel mixed metal oxides introduced in chapter 4 ZnSrO, along with the interfacial modifier PCBA, introduced in section 3.1, in order to acquire better understanding of the ZnO Sr doping mechanism and control charge separation at hybrid organic-inorganic interfaces. ZnSrO was chosen over ZnBaO due to its overall superior performance. First, we examine the effect of Sr doping on the charge separation at the interface with P3HT and correlate it to the photovoltaic performance of the solar cells. Next, we demonstrate that by modifying the doped oxide films we can significantly enhance the efficiency of charge separation.

5.2 ZnSrO/P3HT Hybrid PV Devices

ZnSrO was used as an electron acceptor in model P3HT hybrid photovoltaic devices. First, the optimal doping concentration was determined by optimising device performance, in a similar fashion as before. The origin of an improvement in the open circuit voltage as well as a drop in short circuit current with doping are investigated. The device architecture, including a PCBA layer (used in the following section 5.3) is shown in figure 5.1. The device fabrication procedure is described in section 3.2.

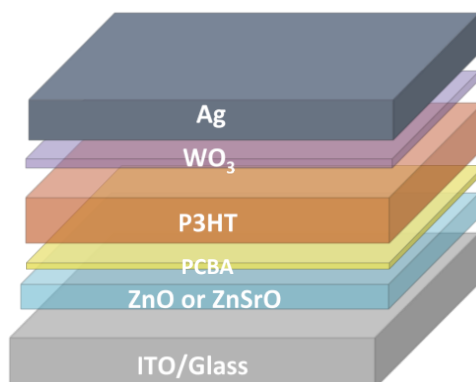


Figure 5.1: Schematic structure of a ZnO/organic hybrid photovoltaic device.

5.2.1 Doping Level and Device Performance

The photovoltaic performance key parameters of the hybrid PV devices are shown in figure 5.2. We observe a significant decrease in the short-circuit current densities compared to the ZnO/P3HT:PCBM BHJ devices from chapter 4. J_{SC} obtained for the hybrid devices is lower by almost two orders of magnitude (0.145 mA cm^{-2} cf. 10 mA cm^{-2}) as shown in figure 5.2(b).

In a bilayer hybrid device only excitons that are generated within the exciton diffusion length (few nanometers) from the polymer/metal oxide interface can contribute to the photocurrent; in contrast, the BHJ device makes use of photon absorption throughout the bulk in the intermixed layer.¹² Upon photoexcitation, only those excitons that are generated within the diffusion length of P3HT can reach the interface with the substrate. Taking into consideration the maximum

absorption coefficient of P3HT¹³, $2 \times 10^5 \text{ cm}^{-1}$ at wavelength 510 nm and assuming an exciton diffusion length of 6 nm as reported by Sim et al.¹⁴ we estimate that at most 10% of light is absorbed within the exciton diffusion length range.⁸ Therefore we would expect the PCE of a hybrid device to fall at about a tenth of the BHJ PCE assuming that the only limiting factor here is the exciton diffusion. A power conversion efficiency of the order of 0.3 - 0.4 % for a hybrid ZnSrO/P3HT is expected given the 3.8% power conversion efficiency obtained for the ZnSrO/P3HT:PCBM device. From figure 5.2(d) we see that the PCEs for the hybrid devices lie in the range of 0.02 - 0.03 % ; this indicates that the process of charge separation is not efficient and that the device performance is limited by an additional recombination mechanism. Electron-hole pairs at the polymer/ZnO interface can form bound charge pair (BCP) states and undergo geminate recombination rather than separate into free charge carriers. This is discussed in more detail in section 5.3 where we show that losses associated with back recombination are resolved with PCBA SAM modification.

The photovoltaic performance of ZnO/P3HT solar cells with varying degrees of Sr doping are summarised in figure 5.2. The doping level is represented by the volume % of the dopant precursor solution contribution to the total blend solution used for depositing the metal oxide film. Figure 5.2(a) shows that the open circuit voltage (V_{OC}) of the devices increases with increasing doping % from an average of 0.36 V for undoped-ZnO/P3HT solar cell, to 0.58 V for 8% doping. Figure 5.2(b) shows that the Sr doping lowers the short circuit current (J_{SC}) of the devices by approximately 20%, suggesting that the long-range charge separation at the ZnSrO/P3HT interface is inferior to that at ZnO/P3HT interface. Figure 5.2(c) shows no specific trend in the fill factor (FF) of the devices as their FF remains largely comparable to that of undoped ZnO/P3HT devices, with only a small increase. The power conversion efficiency (PCE) is presented in figure 5.2(d) and shows that the overall efficiency can be increased by nearly 50% and its maximum value is achieved for 6% Sr doping. The remainder of the study is performed using this optimal doping concentration.

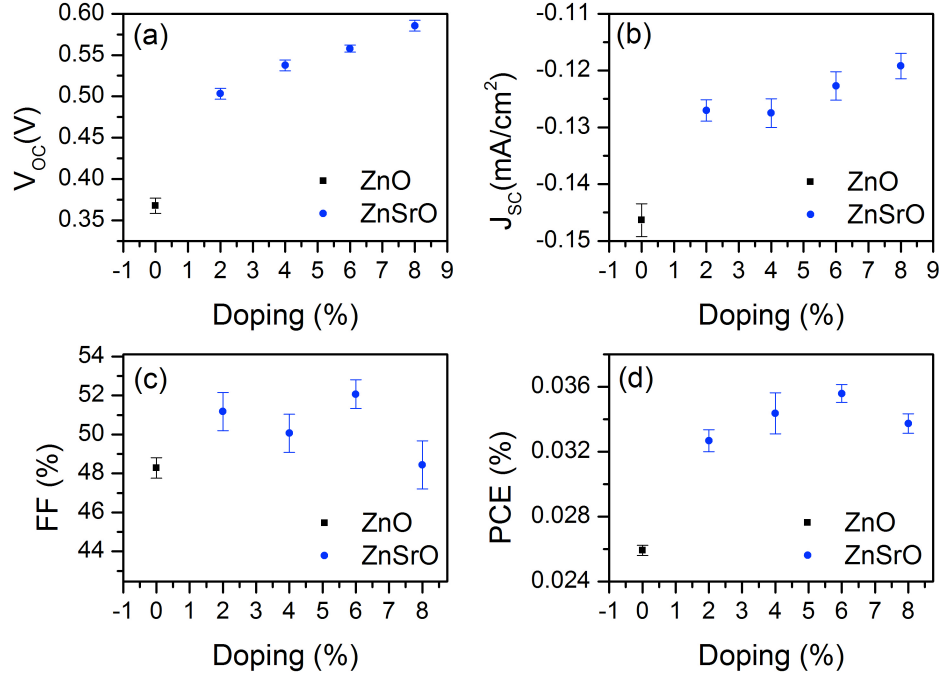


Figure 5.2: (a) V_{OC} , (b) J_{SC} , (c) FF and (d) PCE of ZnSrO/P3HT photovoltaic devices with varying % of Sr doping. Measurements carried out by Dr Vaynzof.

5.2.2 Open-circuit Voltage Improvement Discussion

An enhancement of the open-circuit voltage in doped ZnO/polymer solar cells can arise from several reasons. For example, an upward shift of the conduction band upon doping will result in an increased energetic difference between the HOMO of the donor and the conduction band of the oxide, and thus, increased V_{OC} . This approach was demonstrated for Mg doped ZnO by Olson *et al.*, where the authors achieved a 0.4 V increase in the V_{OC} through the engineering of the conjunction band offset.¹⁵ Another possible cause for enhanced V_{OC} is a decrease in the dark current of the device which may arise from a decrease in conductivity of the metal oxide with doping.¹⁶ To investigate if the origin of the improved V_{OC} in the case of Sr doping arises from shifts in the conduction band of the metal oxide, we performed UPS measurements, which in conjunction with UV-

Vis measurements of the optical gap of the doped and undoped metal oxides, can be used to reconstruct the energy level alignment between the metal oxide and the P3HT polymer (figure 5.4(a)). We find that the work function of both the undoped and Sr doped ZnO films is equal to 3.6 eV and the valence band position is found to be 3.2 eV below the fermi level for both films. UV-Vis measurements reveal that the optical gap of ZnO and ZnSrO are 3.25 eV and 3.3 eV, respectively (figure 5.3).

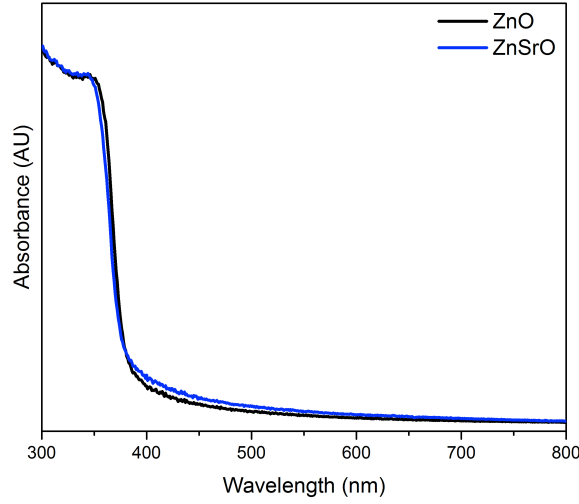


Figure 5.3: UV-Vis absorption spectra for ZnO and ZnSrO.

These values are used to estimate the position of the conduction band, which in the case of ZnO coincides (within the experimental error) with the position of its fermi level. Such behaviour is consistent with the degenerate n-type nature of ZnO. The conduction band of ZnSrO is estimated to be only 0.05 eV above that of ZnO and 0.1 eV above the fermi level. However, since the measured increase in V_{OC} for 6% Sr doping of ZnO is 0.2 V, we find that the small shift in the position of the conduction band cannot be the main reason for the increased V_{OC} .

Next, we investigated if the increased V_{OC} is a result of reduced conductivity of ZnSrO. Figure 5.4(b) shows two-point probe IV measurements for ZnO and ZnSrO thin films. The IV characteristics were linear in all cases and the data are represented on a semi-log current voltage scale for convenience. The measured

current at 40V for the doped films is almost 2 orders of magnitude lower compared to the pure ZnO films. This suggests two orders of magnitude difference between the ZnO and the Sr doped ZnO film conductivities¹ accounting for the significant reduction of the dark current, as shown in figure 5.4(c). Thus, we conclude that the origin of the improved V_{OC} is a reduction in the device dark current due to decreased metal oxide conductivity.

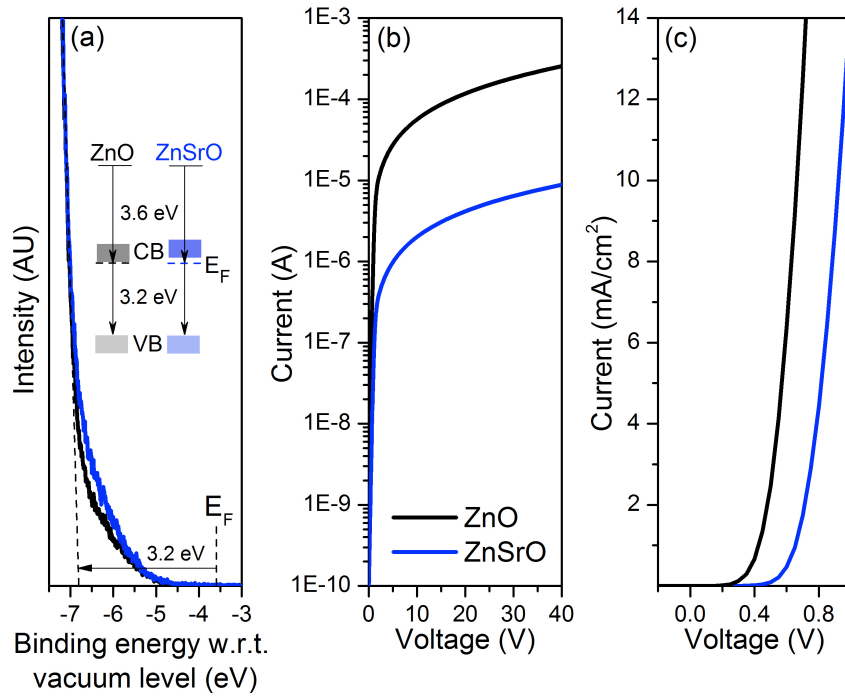


Figure 5.4: (a) UPS spectra of the valence band of ZnO and ZnSrO (energy level diagrams are shown in the inset) (b) IV characteristics for ZnO and ZnSrO thin films, (c) dark IV measurements of ZnO/P3HT and ZnSrO/P3HT photovoltaic devices.

5.2.3 Interfacial Charge Separation

In order to investigate the origin of the reduction in J_{SC} , we performed pump-push photocurrent (PPPC) measurements and compare the relative amount and recombination dynamics of bound charge pair (BCP) states at the ZnSrO/P3HT

interface to that of ZnO/P3HT (figure 5.5(a)). This technique optically activates and probes in real time the formation and recombination of BCPs which, as we proposed previously, are related to the existence of defect states on the surface of the metal oxide. We find that the lifetime of the BCP states is almost the same for ZnSrO and ZnO acceptors. This indicates the molecular origin of the trapping sites is the same and Sr does not introduce qualitatively a new type of interfacial defects. At the same time, the relative amount of BCP states over free charges is higher at the ZnSrO/P3HT interface. This indicates that the density of those trapping states responsible for the creation of BCP states increases, resulting in less efficient charge separation at that interface.

To compare the amount of sub-bandgap states in ZnO and ZnSrO we employ photothermal deflection spectroscopy (PDS) which is an ultra-sensitive absorption measurement technique. PDS measurements reveal that the sub bandgap absorption in the range of 1.6 eV to 3.0 eV is higher for ZnSrO than that of ZnO (figure 5.5). We further investigated the surfaces of ZnO and ZnSrO by means of XPS which is able to reveal compositional changes at the surface of the oxide. Figures 5.5(c) and 5.5(d) show the O1s spectra for ZnO and ZnSrO thin films, respectively. The spectra show that the high binding energy peak at 532.4 eV, assigned to surface oxygen species, is significantly higher for ZnSrO than for ZnO. We can assume that it is these groups that act as trap sites for electrons and hamper charge separation at the interface of both oxide systems. To conclude, the increased amount of surface local low-energy states at the ZnSrO surface results in an increased amount of bound charge pairs at the interface and a decrease in short circuit current.

5.3 Interfacial Modification Using PCBA

Recently, it was demonstrated that self-assembled monolayers (SAMs) can be used to modify the oxide surface and significantly improve charge separation at the interface.^{8,11} This is achieved through the multiple beneficial effects of the SAM, such as: control of energy level alignment, trap passivation, increase electron-hole separation and more. We utilize PCBA as a surface modifier, which we previously demonstrated can halve the amount of bound charge pairs at

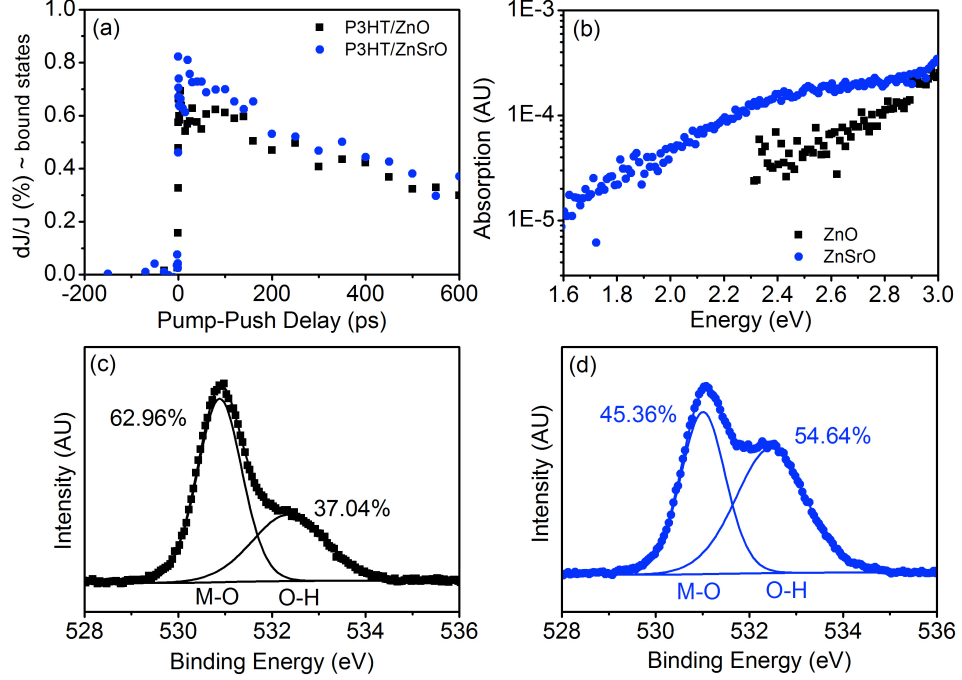


Figure 5.5: (a) PPPc measurements on ZnO/P3HT and ZnSrO/P3HT photovoltaic devices (b) PDS measurements on ZnO and ZnSrO thin films, XPS O1s spectra of (c) ZnO and (d) ZnSrO.

the organic-inorganic interface. This significantly increases the J_{SC} of the Zn-SrO/P3HT devices.

5.3.1 Device Performance

Figure 5.6 compares the photovoltaic performance of unmodified and PCBA modified devices. Although the V_{OC} of the devices is slightly reduced upon modification, the value for ZnSrO/PCBA/P3HT/PCBA devices is still significantly improved as compared to ZnO/PCBA/P3HT. This further confirms that this improvement originates from the reduced conductivity of ZnSrO and not from the interfacial energetics, which in this case is largely determined by the PCBA monolayer. The J_{SC} of the PCBA modified devices is significantly improved

(figure 5.6(b)), consistent with previous reports. Surprisingly, the J_{SC} of the ZnSrO/PCBA/P3HT/PCBA is 30% higher than that of ZnO/PCBA/P3HT devices. Although the use of ZnSrO instead of ZnO itself leads to a decrease in the J_{SC} , these results show that when ZnSrO is combined with PCBA the obtained device is superior to all the rest. This is nicely illustrated in figure 5.6(d): the overall PCE is tripled for the PCBA modified ZnO devices whereas there is an impressive 6-fold increase for the ZnSrO modifies devices with the best device showing PCE of 0.4%. From the extensive characterisation of the two types of oxides performed previously and presented in section 4.2 the possibility that these changes in J_{SC} originate from changes in the absorption efficiency of the organic material (due to changes in roughness of the oxide films and hence interfacial surface area or transparency) are eliminated since the two films are very similar with these respects. Additionally, increased surface area in ZnSrO would have resulted in increased J_{SC} for unmodified devices, which as discussed above is instead decreased. We know from the previous section 5.2 that the surface properties vary significantly for the two films and could account for different charge separation efficiencies at the oxide/organic interface. The fact that the value for the PCE of the PCBA modified ZnSrO device is now in good agreement with what was expected based on the exciton diffusion limitation, suggests that the formation of BCP is no longer limiting the performance of the device. This is in good agreement with PPPc spectroscopy results presented in the following section where the relative amount of BCP states for the PCBA modified ZnSrO device is almost negligible.

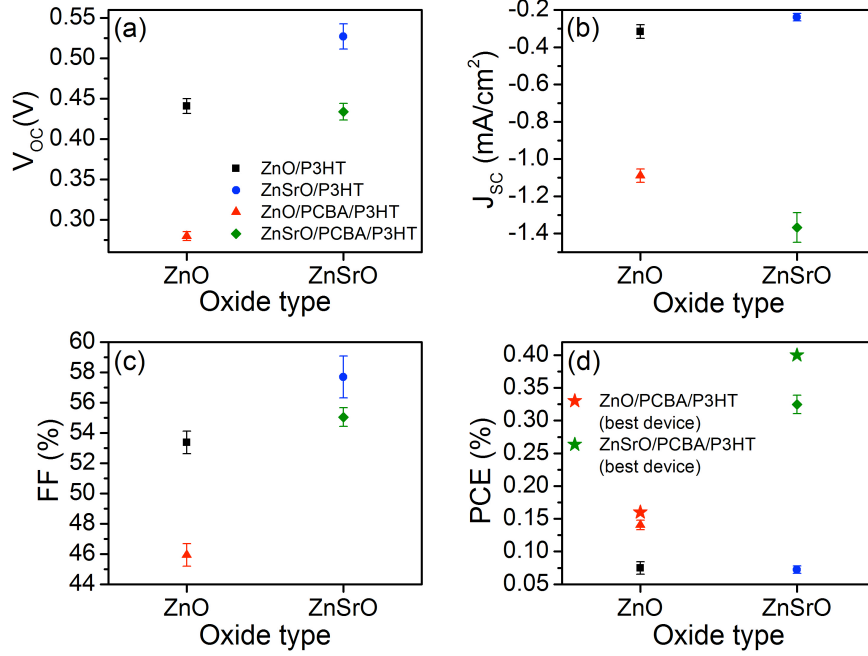


Figure 5.6: (a) Open circuit voltage (V_{OC}), (b) short circuit current (J_{SC}), (c) fill factor (FF) and (d) power conversion efficiency (PCE) of hybrid photovoltaic devices with and without PCBA modifier. Measurements carried out by Dr Vaynzof.

5.3.2 Charge Separation Efficiency

From these results, it appears that upon modification the efficiency of charge separation at the ZnSrO surface was improved more than for ZnO. We performed PPPc on PCBA modified devices, which are shown in figure 5.7(a) together for the previously measured unmodified devices for comparison. In the case of ZnO, the relative amount of BCP states is significantly reduced by the introduction of the PCBA monolayer, consistent with previous results. In the case of ZnSrO, the amount of BCP states is almost negligible, confirming that the charge separation at this interface is indeed very efficient. The origin of this improvement could be an improved coverage of the PCBA monolayer on ZnSrO. PDS measurements

revealed increased absorption from ZnSrO/PCBA as compared to ZnO/PCBA (figure 5.7(b)). UPS measurements also show a slight increase in the PCBA valence band features (Figure 5.7(c)). This suggests that PCBA forms a more complete monolayer on ZnSrO than on ZnO. It is possible that this is achieved due to the increased amount of defect groups on the oxide surface or could be related to the amount of strain caused with the adsorption of a bulky PCBA species.

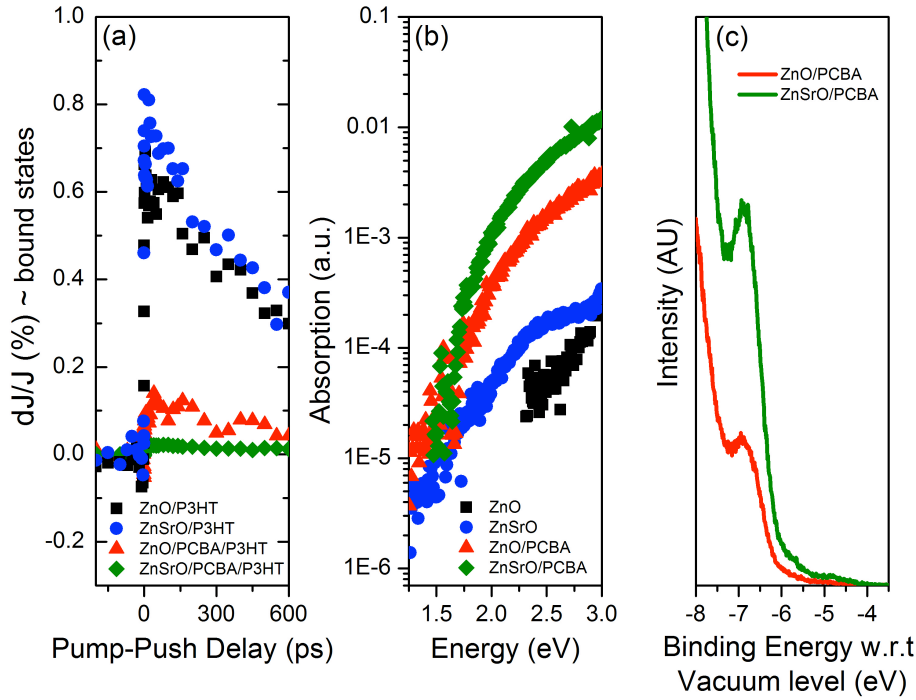


Figure 5.7: (a) Pump-push photocurrent spectroscopy measurements on ZnO/P3HT and ZnSrO/P3HT photovoltaic devices with and without PCBA modifier (b) photothermal deflection spectroscopy measurements on ZnO and ZnSrO with and without PCBA modifier, (c) Ultraviolet photoemission spectra of ZnO/PCBA and ZnSrO/PCBA.

To confirm that increased coverage of another monolayer can be achieved on ZnSrO, we chose to investigate N719 dye, which is similar in size to PCBA

and binds to the oxide surface with the same functional group (COOH). As the absorption of N719 is significantly stronger than that of PCBA we measured UV-Vis spectra to compare the coverage of ZnO versus ZnSrO (see figure 5.8). We find a slight increase in the absorption features of N719 when formed on ZnSrO, consistent with our PDS results for PCBA. It is interesting that the increase amount of the oxygen species at the oxide surface which hampered the charge separation at the ZnSrO/P3HT, is likely to be responsible for the improved PCBA surface coverage of the oxide, which makes its charge separation efficiency to be superior to that of ZnO. This shows that interfacial modifiers can be used to control and tame disordered interfaces and turn their unfavourable properties to an advantage.

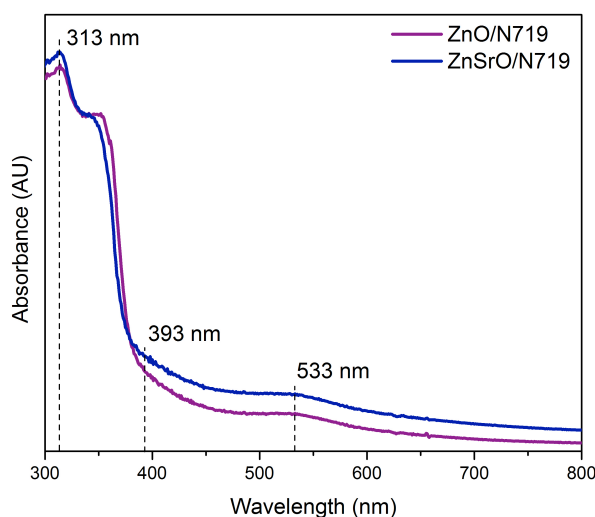


Figure 5.8: Uv-vis absorption spectra of ZnO/N719 and ZnSrO/N719.

5.4 Conclusions

To summarise, we demonstrate that with a combined approach of metal oxide doping and surface modification, it is possible to control and enhance the photoinduced charge separation properties of a metal oxide/conjugated polymer interface. We report a promising power conversion efficiency of 0.4% for a bilayer configuration of ZnO/P3HT. This approach could be extended to nanostructured

metal oxide systems and used to further increase the efficiency of hybrid photovoltaic devices.

References

- [1] Pachoumi, O., Li, C., Vaynzof, Y., Banger, K.K., and Sirringhaus, H. (2013) *Adv. Energy Mater.*, **11**, 1428. 107, 108, 113
- [2] Olson, D.C., Lee, Y.J., White, M., Kopidakis, N., Shaheen, S.E., Ginley, D.S., Voigt, J.A., and Hsu, J.W.P. (2007) *Journal of Physical Chemistry C*, **111**, 16 640. 108
- [3] Kuo, C.Y., Tang, W.C., Gau, C., Guo, T.F., and Jeng, D.Z. (2008) *Applied Physics Letters*, p. 033307. 108
- [4] Qiu, J., Guo, M., and Wang, X. (2011) *ACS Appl. Mater. Interfaces*, **3**, 2358. 108
- [5] Kim, E., Vaynzof, Y., Sepe, A., Guldin, S., Scherer, M., Cunha, P., Roth, S.V., and Steiner, U. (2014) *Adv. Funct. Mater.*, **24**, 863. 108
- [6] Vaynzof, Y., Bakulin, A., Gelinas, S., and Friend, R.H. (2012) *Phys. Rev. Lett.*, **108**, 246 605. 108
- [7] Nemec, H., Rochford, J., Taratula, O., Galoppini, E., Kuzel, P., Polivka, T., Yartsev, A., and Sundstrom, V. (2010) *Phys. Rev. Lett.*, **104**, 197 401. 108
- [8] Vaynzof, Y., Kabra, D., Zhao, L., Ho, P.K.H., Wee, A.T.S., and Friend, R.H. (2010) *Applied Physics Letters*, **97**, 033 309. 108, 110, 114
- [9] Goh, C., Scully, S.R., and Mcgehee, M.D. (2007) *J. Appl. Phys.*, **101**, 114 503. 108
- [10] Lin, Y.Y., Lee, Y.Y., Chang, J.J., Wu, L., and Chen, C.W. (2009) *Appl. Phys. Lett.*, **94**, 063 308. 108
- [11] Weickert, J., Auras, F., Bein, T., and Schmidt-Mende, L. (2011) *J. Phys. Chem.*, **115**, 15 081. 108, 114

REFERENCES

- [12] Halls, J.J.M., Pichler, K., Friend, R.H., Moratti, S.C., and Holmes, A.B. (1996) *Appl. Phys. Lett.*, **68**, 3120. 109
- [13] Kim, Y., Cook, S., Tuladhar, S.M., Choulis, S.A., Nelson, J., Durrant, J.R., Bradley, D.D.C., Giles, M., McCulloch, I., Ha, C.S., and Ree, M. (2006) *Nat. Mater.*, **5**, 197. 110
- [14] Sim, M., Shin, J., Shim, C., Kim, M., Jo, S.B., Kim, J.H., and Cho, K. (2014) *J. Phys. Chem. C*, **118**, 760. 110
- [15] Olson, D.C., Shaheen, S.E., White, M., Mitchell, W.J., van Hest, M.F.A.M., Collins, R.T., and Ginley, D.S. (2007) *Adv. Funct. Mater.. Mater.*, **17**, 264. 111
- [16] Lee, Y.J., Davis, R.J., Lloyd, M.T., Provencio, P.P., Prasankumar, R.P., and Hsu, J.W.P. (2010) *IEEE J. Sel. Topics Quantum Electron.*, **16**, 1587. 111

Chapter 6

Charge Accumulation Spectroscopy for Organic Photovoltaics

In this chapter an experimental technique allowing for in-situ, high resolution optical spectroscopy and electrical measurements for an organic solar cell device is discussed. The main challenges regarding sample suitability and the development of the experimental setup are the focus of this chapter whereas in the chapter to follow preliminary measurements are presented. Optical spectroscopy, without the use of any modulation techniques, is used to detect trapped charge and charge transport information in OPV for long time-scales similar to the Charge Accumulation Spectroscopy technique developed recently in our group for organic field effect transistors. By tracking changes in transmission due to charge accumulation in an OPV device we can acquire direct spectroscopic evidence associated with degradation and efficiency loss pathways.

6.1 Introduction

As it has already been mentioned in chapter 4, understanding and improving the stability of organic photovoltaic devices is currently an important challenge. Extensive research addressing operational stability and sensitivity to some of the atmospheric components has led to a remarkable improvement in device lifetimes from seconds and minutes to many thousands of hours when operated in air.¹ Even so OPV devices are still considerably outperformed by crystalline silicon PVs in terms of operational stability. Substantial understanding of the physical chemistry behind degradation issues is the key towards improving device stability by driving an educated synthesis of optimized materials and the optimisation of device architecture.

A very common approach to study OPV degradation is exposing a device to various experimental conditions and monitoring the photovoltaic properties (J_{SC} , V_{OC} , FF and PCE) as a function of time. This approach itself is empirical and indirect, however when used alongside with a variety of analytical techniques it can provide significant insight into degradation processes taking place in materials and devices. A broad suite of analytical techniques, including current voltage characteristics and photocurrent measurements and a range of physical and chemical probes such as many microscopy techniques and photoelectron spectroscopy is often used in order to gain as much information as possible.^{2,3}

Spectroscopic techniques are amongst the most powerful techniques that allow to investigate the fundamental photophysical and dynamical processes governing charge generation, recombination and extraction in organic and polymer semiconductors and correlate them to electrical properties and device performance of functional devices. Electromodulation spectroscopy and electroabsorption spectroscopy techniques have been successfully applied to investigate charge injection and built-in field properties in diode configurations. Time-resolved optical spectroscopy, photoinduced absorption and magnetic spectroscopy techniques provide significant means in identifying loss mechanisms hindering performance by studying the dynamics of charge transfer states, sub-bandgap absorption as well as the kinetics of interfacial electron transfer processes.^{4,5,6,7,8} These techniques were further extended to gain understanding of photo-degradation processes such as

radical scavenging and the importance of tuning the electron affinities of the electron acceptor compound in order to inhibit the photodegradation of the photovoltaic compound.^{9,10} Steady-state UV-Vis-NIR optical spectroscopy is often used to demonstrate the photooxidation of polymers by measuring a significant decrease in the absorption known as photo-bleaching or changes in the morphology occurring during degradation such as PCBM and C60 dimerization.^{11,12}

Since OPV devices consist of a stack of layers it is important to be able to study both individual materials, as well as the complete, or even partial device. Studying individual materials is by far more straightforward and hence a broader range of analytical probes are available. Studying individual materials however excludes a wide range of degradation phenomena related to interlayer and interface processes which could contribute significantly towards the overall device degradation, both inert and photo-induced. The significant role interface physics play in the device macroscopic behaviour in terms of performance and stability has already been discussed and investigated in chapters 4 and 5. Furthermore, performing measurements on a complete device allows to probe changes at different charge carrier concentration conditions by applying an external bias (voltage or light exposure). However, to the best of our knowledge there is no reported literature on optical spectroscopy measurements performed on whole cells to investigate the device stability by probing related sub-bandgap, charge induced absorption features in time. Optical degradation measurements are often performed on thin films of the photo-active polymers or the donor-acceptor organic blends and later correlated to device performance neglecting the possible contribution to degradation from interfacial effects and any related trap states. Accelerated aging experiments are often performed in order to trigger a more pronounced change in the absorption of the device, hence clouding intermediate features by more dominant final stage degradation effects such as polymer photo-bleaching and electrode oxidation.

Charge modulation spectroscopy (CMS) is a technique already used in our group and has been successfully employed to study charge transport in fully functional organic field effect transistors.^{13,14,15} Recently, a new optical spectroscopy characterisation technique, charge accumulation spectroscopy (CAS), was developed in our group allowing to directly detect charged species in a polymer film

as part of an OFET and probe them as a function of time under certain stress conditions.^{16,17} The advantage offered by CAS in contrast to CMS is that there is no modulation in the voltage bias applied and hence is sensitive to both mobile and trapped charges. The experimental setup established for the CAS measurements allowed for simultaneous electrical and high resolution optical transmission measurements to be performed in-situ, under controlled environment conditions. In this chapter we describe how this setup was modified in order to be used to perform degradation studies on organic solar cell, allowing for application of an external light bias (to replicate degradation caused by solar light). The two key challenges of this work were to optimise the signal to noise ratio and overcome artifacts. Although our efforts to measure the photo-induced absorption using a white light source have been unsuccessful, the polaron induced absorption measured on OPV devices demonstrated successful operation of the setup and the potential of using this setup to further study OPV stability is discussed.

6.2 Optical Transmittance

When performing an optical spectroscopy experiment the efficiency of light absorption at a particular energy λ by an absorbing material can be characterised by the transmittance,

$$T(\lambda) = \frac{I_{\lambda}}{I_{\lambda}^0}, \quad (6.1)$$

where I_{λ}^0 and I_{λ} are the light intensities of the beams entering and leaving the absorbing material, respectively. According to the Beer-Lambert Law,

$$T(\lambda) = e^{-\sigma(\lambda)nd}, \quad (6.2)$$

where $\sigma(\lambda)$ is the absorption cross-section of the material for photons of wavelength λ ; and n is the molecule density per unit volume. The absorption cross-section is equivalent to the absorption coefficient divided by the number of molecules per unit volume along the light path. As we have already discussed in chapter 2.2.2 light absorption by a molecule can be described by considering the molecule as an oscillating dipole. For organic semiconductors the absorption coefficient

$\alpha(\lambda)$ is characteristic of a particular transition and it is defined by the relevant transition dipole moment (see equation 2.13). A quantity called the *oscillator strength* is often used to express the probability of absorption or emission in transitions between energy levels of a molecule and it is proportional to the square of the transition dipole moment (see equation 2.11).

When performing optical spectroscopy transmittance measurements neutral molecules and charged molecules will be characterised by different oscillator strengths and absorption cross-section and will give rise to different spectra. We can model the transmittance spectrum, $T(\lambda)$, for a semiconducting device as the result of transmittance coefficient contributions from a series of i consecutive absorbing layers, each with a characteristic absorption cross-section $\sigma_i(\lambda)$, thickness t_i and n_i density of unit absorbing species,¹⁸

$$T(\lambda) = \prod_i e^{-\sigma_i(\lambda)t_i n_i} \quad (6.3)$$

We can use the above model to relate the experimentally detected charges in transmittance with the accumulation of charge anywhere in the semiconductor layer. Consider the polymer semiconductor layer in its **neutral state** with $\sigma_p(\lambda)$ absorption cross section of the neutral absorption, n_p polymer units density and thickness t_p . The resulting transmittance spectrum T_N can be expressed by:

$$T_N = \left(\prod_{i \neq p} e^{-\sigma_i(\lambda)t_i n_i} \right) e^{-\sigma_p(\lambda)t_p n_p} \quad (6.4)$$

where the suffix p represents the neutral polymer layer. Now considering the polymer semiconductor layer in the case of charge accumulation, which we will refer to as **charged state**, with $\sigma_p^*(\lambda)$ absorption cross section of the neutral polymer in, n_p^* neutral polymer units density and thickness t_p^* ; and with $\sigma_c(\lambda)$ absorption cross section of the charged units, n_c charged layer density and thickness t_c . The resulting transmittance spectrum T_C can be expressed by:

$$T_C = \left(\prod_{i \neq p^*, c} e^{-\sigma_i(\lambda)t_i n_i} \right) e^{-\sigma_p^*(\lambda)t_p^* n_p^*} e^{-\sigma_c(\lambda)t_c n_c} \quad (6.5)$$

where the suffix p^* represents the neutral polymer layer in the charged state and c the layer of charged units. Assuming: (i) that the absorption cross section for the neutral polymer absorption remains unchanged in the presence of charge accumulation ($\sigma_p(\lambda) = \sigma_p^*(\lambda)$), (ii) that each charged unit will spread over ξ polymer units ($n_p^* = n_p - \xi n_c$) and (iii) that the charges are evenly spread throughout the polymer layer ($t_c = t_p^* = t_p$), equation 6.5 can be rewritten as:

$$T_C = \left(\prod_{i \neq p, c} e^{-\sigma_i(\lambda) t_i n_i} \right) e^{-\sigma_p(\lambda) t_p (n_p - \xi n_c)} e^{-\sigma_c(\lambda) t_p n_c} \quad (6.6)$$

We can now combined equations 6.4 and 6.5 to get an expression for the differential transmittance spectrum:

$$\begin{aligned} \frac{\Delta T}{T} &= \frac{T_C - T_N}{T_N} = e^{[\xi \sigma_p(\lambda) - \sigma_c(\lambda)] t_p n_c} - 1 \\ &= [\xi \sigma_p(\lambda) - \sigma_c(\lambda)] t_p n_c, \quad \text{for } \frac{\Delta T}{T} \ll 1, \end{aligned} \quad (6.7)$$

The above equation shows that the change in transmittance is proportional to the density of charged species in the semiconducting film. This method was previously used in our lab to extract the amount of charge accumulated on an OFET device directly from the optical signal and to estimate the cross-section of the neutral and charged absorption by measuring the transmission coefficient of a film of known thickness and polymer unit density.^{19,18}

6.3 High Sensitivity Optical Spectroscopy Setup

The spectroscopic setup used for the purposes of this experiment was designed and built for the purposes of Charge Accumulation Spectroscopy investigations by Riccardo Di Piedro.¹⁸ The setup was intended for studying long time scale degradation studies and charge trapping mechanisms under controlled environments. Therefore it was designed such that it satisfied the following essential prerequisites. First it offers detection sensitivity of the order of $\Delta T/T \approx 10^{-4}$ without using any direct modulation technique. As an example, this resolution allows to detect charge density accumulation of the order of 10^{12} cm^{-2} for po-

6.3 High Sensitivity Optical Spectroscopy Setup

larons in organic semiconductors of absorption cross-section in the range of 10^{16} cm^2 . Moreover, the system is stable enough to allow for consistent measurements over a long period of time (constant operation in the order of days) meaning that spectra taken with a time delay of a number of days could be directly correlated and would not involve any systematic errors. Finally, it covers a wide spectral range covering the UV-Vis-NIR (200 nm - 1800 nm) regions allowing for simultaneous detection of the neutral absorptions for organic materials as well as sub-bandgap absorption coming from charged or excited species.

The setup mainly consists of a commercially available spectrophotometer, Varian (now Agilent) Cary 6000i, and an Oxford Instruments CF-V cryostat insterted with a custom made sample holder and it is illustrated in figure 6.1. The experimental apparatus (Cary 6000i, Keithley 2612A and Oxford Instruments ITC503) communicate with the control personal computer through the GPIB bus and a *Graphical User Interface*.¹⁸ The Varian Cary 6000i spectrophotometer operation

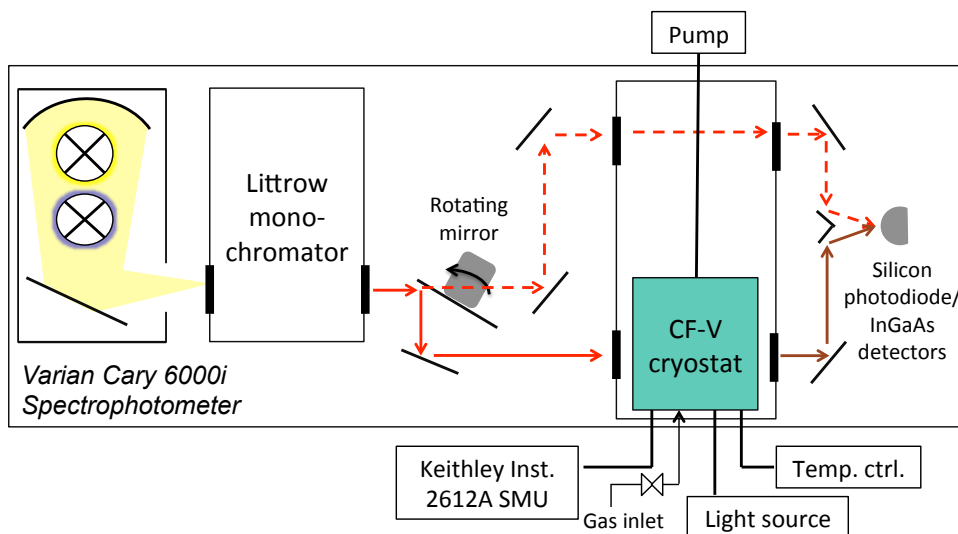


Figure 6.1: Diagram of the experimental setup, showing the main components of the optical system and the additional modifications needed for OPV optical spectroscopy measurements.

is based on transmission mode. A tungsten and a deuterium lamps are used for covering the visible/near infra-red and the UV part of the spectrum respectively. A double Littrow monochromator is used for providing the monochromatic light

and a rotating mirror positioned right after the monochromator exit slit switches the monochromated light beam between a front and reference path. The two beams after passing through the sample compartment are collimated back on the same photodetector. A silicon and an InGaAs photodiodes are used as photodetectors for UV-Vis and NIR detection respectively. The basic operation of the spectrophotometer is based on constantly detecting the difference in intensity between the two beams, compensating for any systematic errors arising from fluctuations of the system (temperature, lamp intensity, stray light). The custom made sample holder fitted in the CF-V cryostat allows for electrical connection to be made on the sample (to a Keithley 2612A), stable alignment of the sample with the spectrophotometer beam path, connection to a Oxford Instrument ITC503 temperature controller. The modified version of the cryostat in this experiment has one of the side windows replaced by a custom made window (fabricated by our lab technician R.Beadle), as shown in figures 6.2(a) and (b), allowing for an external light source as well as gas flow while at the same time offering good vacuum ($\approx 10^{-6}$ mbar) seal when using a rotary pump.

6.4 External Light Source

As mentioned above an external light source was installed in the above setup. The purpose of this additional light source was to be used to replicate conditions under operation for the organic solar cell under investigation. This give us the potential of studying the long-term operational stability of the sample. In addition it gives the potential of studying the optical characteristics of the device under excitation and hence detecting the photo-induced absorption (PIA). We discuss later on how the task of operating the spectrophotometer with the external light source on simultaneously was a challenge.

The requirements we set in choosing the external light source was that it should replicate realistic conditions by covering significant part of the solar light spectrum and have comparable intensity. It should also be able to operate for a few hundreds of hours without overheating, so it should have a suitable cooling system. In addition minimizing stray light was a key in order to perform PIA measurements and therefore being able to apply the light through an optic fibre

6.4 External Light Source

would be advantageous. The light source we decided that was reasonably suitable for this experiment was the High Intensity Fibre (white) Light Source OSL1 obtained from Thorlabs. The fibre bundle chosen was BF20HSMA01 with 2 mm diameter for maximum intensity and high OH content for best operation in the UV-Vis region. The emission spectrum of the lamp used is shown in figure 6.2(c). A reflective collimator was attached to the fibre bundle exit in order to focus the white light beam on the sample, maximizing intensity of incident light on the sample and minimizing the stray light. A 3D model of the setup was designed using computer-aided design software and the final version, to scale, is illustrated in figure 6.2(b). The collimator was chosen such that it suitable for collimating broadband light (450 nm - 20 μm) and hence the selection of a reflective collimator with protected silver coating rather than a lens collimator. Its effective focal length (EFL) should also be comparable to the distance of the collimator aperture to the sample and the size of the beam bigger than the size of the sample, therefore the RC08APC-P01 (8.5 mm diameter, 33 mm EFL) model was chosen (provided by Thorlabs).

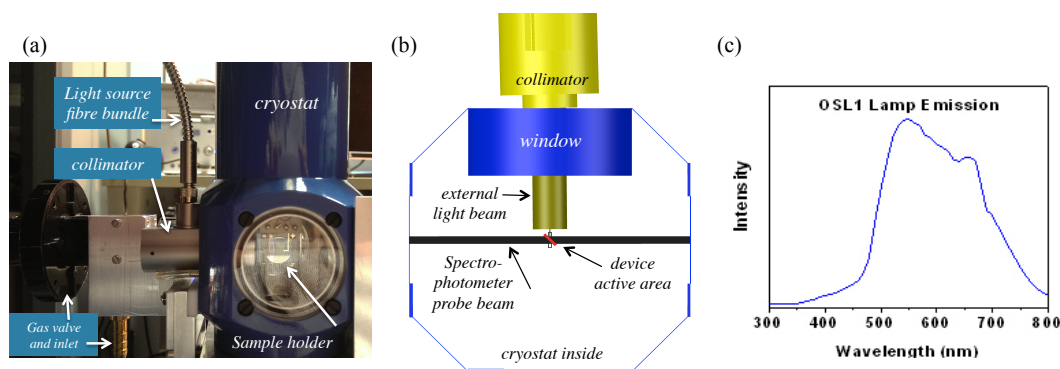


Figure 6.2: (a) Cryostat modification allowing for external light exposure and gas flow through side window, (b) cryostat top-view showing external light beam in comparison to sample active area (red) placed at an angle and spectrophotometer probe beam (black), (c) absorption spectrum of external white light source.

The possibility of performing PIA measurements, i.e. taking optical spectra whilst the external light source is on was investigated. Figures 6.3(a) and (b) show transmittance spectra, without a sample loaded, in the dark (black) and

with the external light source on at different intensities. Ideally in order to be able to perform PIA measurements using the ELS the transmittance spectrum should be insensitive to the irradiation of the sample with the ELS i.e. spectra recorded with the ELS on or off should be identical given than all other parameters remain unchanged. In this case it can be seen that the spectra vary significantly and are not reproducible. The transmittance appears to be decreased over the whole spectral range. This is attributed to the effect of stray light reaching the spectrophotometer photodetectors, however it is different from what we expected which is an increase in transmittance in the spectral range matching the one of the ELS, due to the additional stray light. This suggests that the performance of the photodetectors is unreliable under such high intensity stray light conditions.

Although we tried many ways to reduce the amount of stray light it was impossible to reduce it beyond the sensitivity of the photodetectors. Since there is no modulation technique involved in this setup there is no other way of excluding contribution from an asymmetrically applied external light than by eliminating it. Since the ELS was designed such that light is focused on the sample placed in the way of the front beam, in the presence of significant stray light background illumination is no longer the same for light reaching the detectors from the two paths (front and reference) and hence the result is not true. For example we tried inserting a slit, just about bigger in size than the spectrophotometer light beam (6 mm x 2 mm), close to the detectors compartment aperture. The resulting spectra are shown in figure 6.3(b), they now resemble more the spectrum in the dark however they are far from being error free.

We have also tried minimising stray light by using a monochromated light source. A high intensity (<5 mW) laser diode was chosen at a particular wavelength of 650 nm in order to photoexcite the photoabsorbing polymer which would later be used in an organic solar cell device. The results from the monochromated light source are shown in figure 6.3(c). Although the spectra now resemble each other, especially in the NIR region, there are increased levels of noise in the UV-Vis regions of the spectrum. From the results of this section we come to the conclusion that this setup is unsuitable for performing PIA measurements as it is and careful design alterations could potentially improve its performance; however we did not pursue this any further in this project.

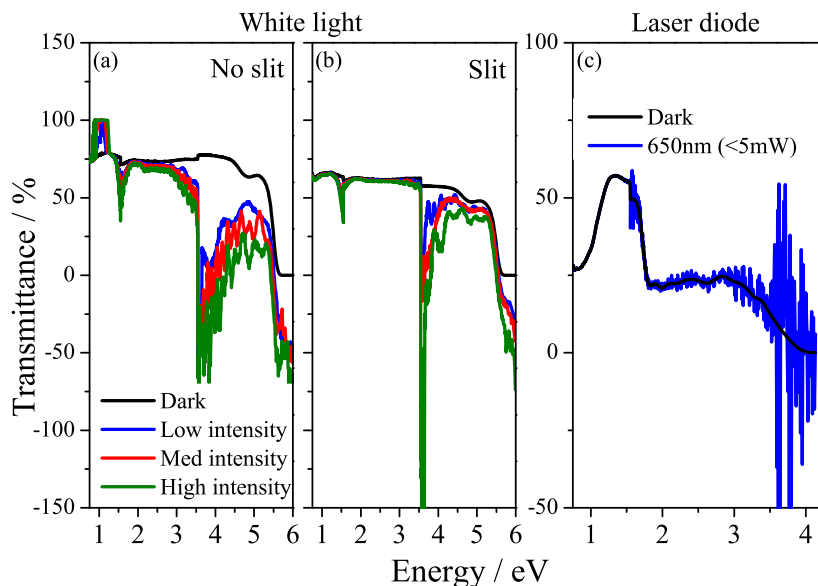


Figure 6.3: Non reproducible transmittance spectra taken in the dark and with (a)(b) white and (c) monochromatic external light on.

6.5 Device Architecture Optimisation

Here we discuss the organic solar cell device architecture, material selection and fabrication process. We give particular emphasis on the constraints set of large active device area and high transparency. The architecture of the device is shown in figure 6.4. We have used the inverted structure, one of the currently best performing architectures in terms of stability. This was done in order to be able to identify new degradation paths by detecting features which would otherwise be clouded by well known dominant effects such as low-workfunction top electrode oxidation, poor barrier effect or PEDOT:PSS etching of the ITO interface. A detailed device fabrication procedure is given in section 3.2. ITO was sputter coated on Spectrosil 2000 substrates to ensure good transparency over the whole UV-Vis-NIR. We used the novel mixed metal oxide, ZnSrO as an EEL, which showed to improve both performance and stability of devices²⁰ discussed in chapter 4. Instabilities originating from the metal oxide/organic interface have previously been reported and are not fully understood. However there is no di-

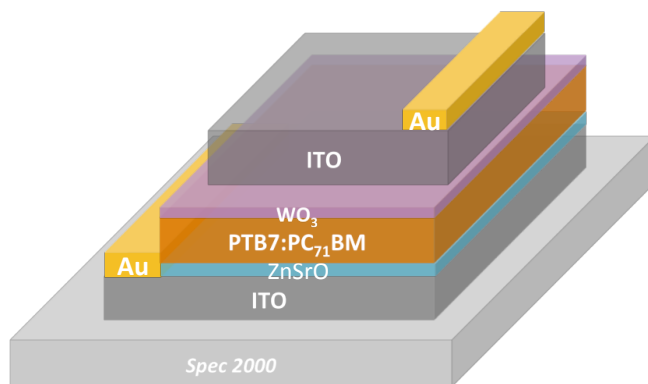


Figure 6.4: Device architecture diagram for inverted organic photovoltaic devices used for optical spectroscopy measurements.

rect spectroscopic evidence of this instability reported and one of the aims of this project was to investigate this (see chapter 7).

PTB7:PC₇₀BM is the active layer blend system of choice. PTB7 is a low band-gap polymer which is attracting extensive current interest in OPV applications. The optimisation of blend morphology with PC₇₀BM fullerene acceptor and device architectures has led to efficiencies over 9%. However PTB7, and similar low-bandgap donor polymers have been reported to be rather unstable under operation in the presence of oxygen. The exact mechanism behind this instability however is under dispute. Soon *et al*²¹ have suggested a mechanism involving singlet oxygen generation from triplet excitons whereas Grancini *et al* have shown that the triplet state has no role in the degradation process.⁷ Thermally evaporated tungsten trioxide, WO₃ is used as a Hole Transport Layer (HTL). P-type oxides, such as WO₃ are commonly used in inverted organic solar cells due to their electron blocking properties and improved stability compared to the otherwise popular alternative PEDOT:PSS. We can see from Figure 6.4 that ITO is the top electrode. More discussion on the top electrode selection follows. In cases where transparency was not relevant a non-transparent 50 nm Ag electrode was thermally evaporated instead.

6.5.1 Device Active Area

One of the constraints for device fabrication was that the size of the device active area should be bigger than the size of the spectrophotometer probe beam to avoid any errors due to variations in the probing area. From previous investigations carried out by R. Di Pietro the minimum size of the beam size satisfying essential signal to noise ratio requirements (with a $\sim 60\%$ transparent sample in place) was found to be $6\text{ mm} \times 2\text{ mm}$. We therefore decided to use the same beam size and hence designed a $7\text{ mm} \times 4\text{ mm}$ (28 mm^2) active area device. This is an area at least five times bigger than most lab devices which are of the order of a few mm^2 . The performance of organic solar cells is well known to decrease significantly with increase in area mainly due to the poor sheet conductivity of the transparent electrode.^{22,23} In addition, a large active area could mean significant average roughness values for each of the layers (depending on deposition method) that could result in pinholes and hence shunts. The formation of pinholes could be an explanation to the repeatedly short-circuited devices we obtained before applying a series of improvements to the procedure used for small area devices.

In order to fabricating a functional large area device we had to apply small, yet detrimental, improvements to the established small area procedure. The main challenge was proven to be pinholes over the large area which would result in a shorted device. To overcome this problem we ensured that the organic layer was very smooth over a large area. The organic layer was spin-coated immediately after the ZnSrO deposition, from a chlorobenzene:1,8-diiodooctane solution. 1,8-Diiodooctane is a solvent additive that has been reported to result in significant morphology and device performance improvements.²⁴ In addition the solution was stirred at 70°C for over 48 hours continuously using a stirring magnet bar and was filtered through a hydrophobic PTFE $0.45\text{ }\mu\text{m}$ filter right before deposition.

In figure 6.5(a) a comparison of the J-V characteristics, measured under 100 mWcm^{-2} AM 1.5G solar simulator conditions, for small area (4.5 mm^2) and large area (28 mm^2) non-transparent (40 nm Ag top electrode) devices, is shown. Detailed device fabrication methods can be found in section 3.2. In figure 6.5(b) the external quantum efficiency corresponding to the small area device is shown for reference. The small area device is superior to the large device area as expected

with a power conversion efficiency of $\sim 7.5\%$ compared to $\sim 5\%$. The poorer performance of the large area device is mainly due to a drop in the short circuit current density (J_{SC}) and the fill factor (FF) whereas the open circuit voltage (V_{OC}) stays unchanged at 0.66V. There is a drop of $\sim 3 \text{ mAcm}^{-2}$ in the J_{SC} and a drop of 14% in the EQE value. Similar losses have previously been attributed to unfavourable charge extraction at the organic/metal interface for large area metal electrodes.

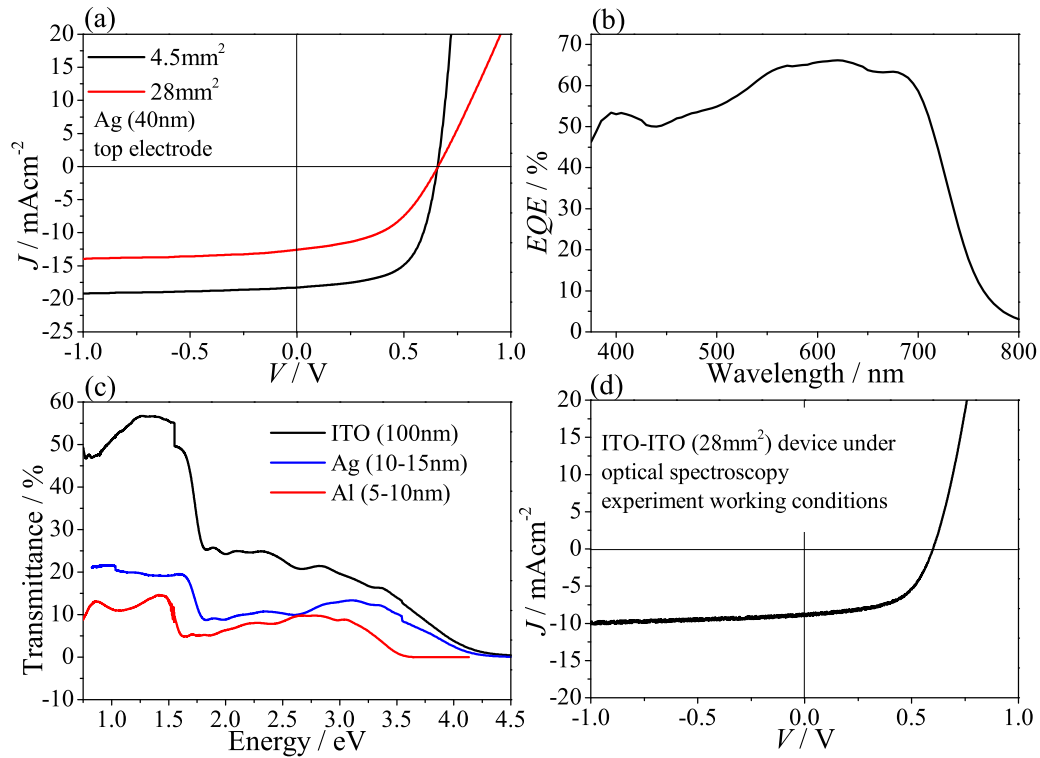


Figure 6.5: (a) J-V characteristics for small and large area devices measured under 100 mWcm^{-2} AM 1.5G solar simulator conditions, (b) EQE for small area reference device, (c) device optical transmittance with three types of top electrodes, (d) J-V characteristics for large area, transparent device measured under the ELS.

6.5.2 Transparent Top Electrode

Since the spectrophotometer we use is operating in transmission mode we had to make sure that the transmission of the whole device was as high as possible to minimise signal to noise ratio. The main challenge towards achieving a functional, transparent device comes from the two electrodes. Low resistivity Indium Tin Oxide (ITO) is often the choice of the most for bottom transparent electrode, to allow for light to reach the photo-active layer (PAL) of the device. As a top electrode a non-transparent metal is usually used such as aluminium, silver or gold depending on the device architecture. An aluminium capping layer is additionally used as a reflective layer to further increase the light collection at the PAL. Here our choice of a top electrode material should provide good transmittance whereas at the same time be conductive enough to ensure ohmic contact with the WO_3 HTL. Indium Tin Oxide sputtered on glass is the standard transparent (bottom) electrode providing excellent light transmission. Conductive polymers such as PEDOT:PSS²⁵ or silver nanowires²⁶ are also employed successfully as transparent bottom electrodes, however the deposition is damaging for the organic layer if they are to be deposited on top. Carbon nano-tubes and or graphene are expensive and difficult to deposit alternatives.^{27,28} The deposition of ultra-thin metal layers by thermal evaporation is an alternative and recently the use of dielectric/metal/dielectric systems is gaining popularity as an improved alternative.^{29,30,31} For the purposes of this experiment we have tried the options of sputter coated ITO and ultra-thin layers of Ag and Al due to their simplicity and availability. In figure 6.5(c) the transmittance spectra for devices with ITO (100 nm), Ag (10 - 15 nm) or Al (10 - 15 nm) as top electrodes are shown. The particular thickness for each of the three top electrodes were chosen such that the resulting film sheet resistance was lying in the range of 50 - 300 Ω/sq . The optical transmittance % for the ITO top electrode device is higher than that for either of the two metals for the complete measured spectrum. Sputter coated ITO was the top-electrode of choice because of the high transparency and at the same time good electrical conductivity. More details on the ITO deposition procedure can be found in the experimental chapter 3.2.4. The J-V characteristics for the resulting optimised large area, transparent device measured under light exposure

conditions described in the previous section are shown in figure 6.5(d) indicating a functional device.

6.6 Charge Induced Absorption in PTB7 Devices

After optimising the device architecture we performed an experiment to test and demonstrate the potential and reliability of the setup. All optical spectroscopy measurements were performed with a fixed slit bandwidth of 0.6 nm, with a resolution of 0.5 nm in the 1800 - 800 nm range, and a 0.1 nm resolution in the 800 - 300 nm range. All measurements are performed at room temperature. We aimed at detecting the PTB7 polaron induced absorption signal by running measurements on a PTB7:PCBM organic solar cell device and compare that to results obtained from the well established Charge Accumulation Spectroscopy technique on PTB7 organic field effect transistors using the same setup.¹⁸ CAS spectra are obtained by calculating the difference between the two scans, normalizing by the reference-scan and smoothing using a third order Savitzky-Golay algorithm (51 points window).

6.6.1 PTB7 Field Effect Transistor

The devices used for this study are bottom-contact, top-gate transistors, made on low-alkali content, borosilicate glass. The measurement technique and device fabrication, are based on previous work done by R.Di Pietro and were carried out by Iyad Nasrallah.¹⁸ High molecular weight electronic grade poly(methyl-methacrylate) (PMMA) provided from Polymer Source Inc. was used as a dielectric. A schematic diagram of the device is shown in figure 6.6. Devices were loaded on the sample holder in the cryostat inside a glovebox to minimise oxygen and humidity absorption by the sample. The samples were evacuated down to $\sim 10^{-5}$ mbar before they were annealed overnight (16 hours) at 353K in order to get rid of any solvent residue or water traces and ensure complete stability of the device in vacuum.

6.6 Charge Induced Absorption in PTB7 Devices

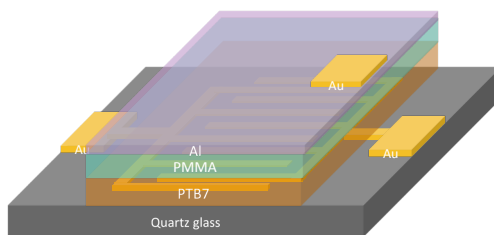


Figure 6.6: Diagram of the bottom-contact top-gate PTB7 field effect transistor.

The transfer curves from a pristine device taken in the linear and saturation regimes are shown in figure 6.7. The small current ratio between positive and negative gate voltage bias implies both hole and electron conductivity and hence possible ambipolar nature.³² The CAS spectrum of both the positive (hole) /

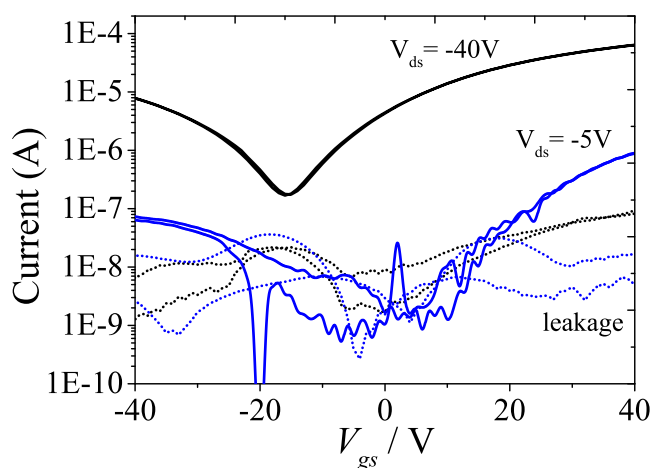


Figure 6.7: Transfer characteristics of a working PTB7 p-type OFET in linear (blue) and saturation (black) regimes. Dashed lines indicate the corresponding leakage current.

negative (electron) polarons in the OFET accumulation layer can be obtained by calculating the difference between an optical scan with the gate grounded and a consecutive optical scan with a negative / positive bias applied. Polaronic charges in organic semiconductors exhibit characteristic charge induced optical absorptions different from those of the neutral molecule and are associated with bleaching of the neutral absorption. The calculated CAS spectra for different neg-

active and positive gate voltages are summarised in figure 6.8. The measurement obtained with the device grounded was used as a reference. The CAS spectra for

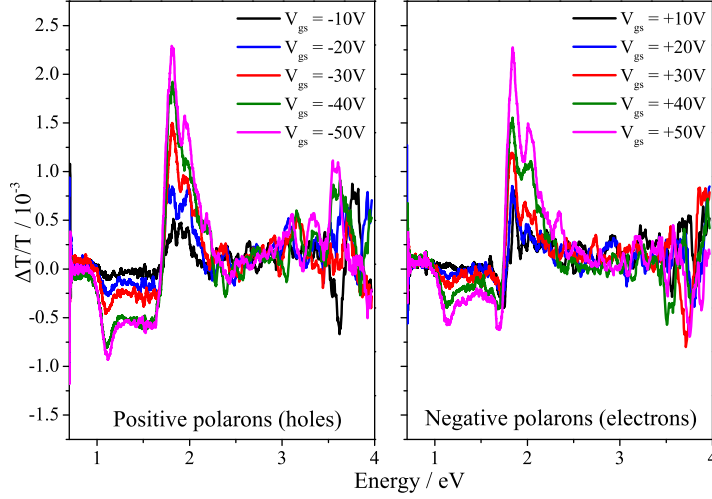


Figure 6.8: CAS spectra for a PTB7 transistor measured at different negative and positive voltages.

both negative and positive bias show a broad induced absorption ($\Delta T/T < 0$) feature at 1 eV - 1.5 eV and a broad bleaching feature ($\Delta T/T > 0$) feature at 1.8 eV - 2.2 eV. The induced absorption and bleaching signals are attributed to the characteristic charge induced absorption from polarons in PTB7 and the associated bleaching of the neutral $\pi - \pi^*$ transition. For a negative / positive gate bias the accumulation layer is positively / negatively charged and hence the detected charge-induced absorption represents the positive / negative polaron. The features are already detectable at $V_{gs} = -10$ V (or $+10$ V) and increase with increasing gate voltage. Both negative and positive features increase with increasing gate bias. By measuring the gate dielectric capacitance $C(V)$ as a function of gate voltage (not shown here) we can calculate the areal charge density n_c in the channel as a function of gate voltage according to:

$$n_c(V_{gs}) = \int_0^{V_{gs}} \frac{C(V)}{Ae} dV, \quad (6.8)$$

where A is the gate electrode area and e the electron charge. We can therefore plot

6.6 Charge Induced Absorption in PTB7 Devices

a graph of the charge density dependence of the amplitude of the polaron induced absorption by extracting the amplitude of the polaron induced absorption peak for each V_{gs} . This amplitude is found to be linearly proportional to the areal charge density down to 10 V for holes and 30 V for electrons as shown in figure

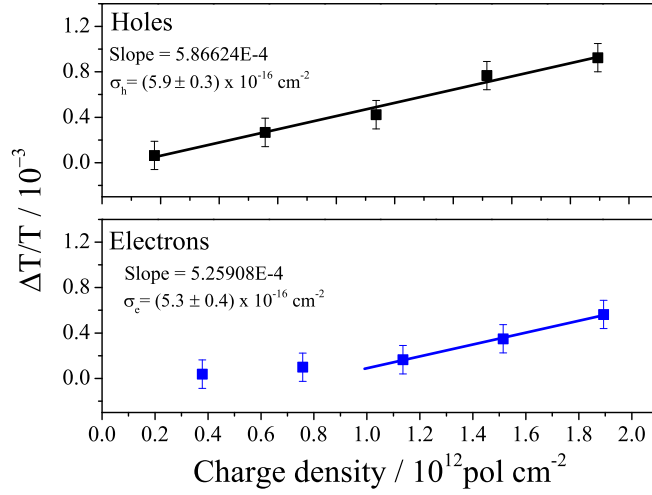


Figure 6.9: Charge density dependence of the amplitude of the positive polarons (holes) and negative polarons (electrons) induced absorption. The absorption cross sections in each case are extracted from the slop of the linear fit.

This demonstrates the sensitivity of the CAS measurement down to the respective gate voltages in each case. According to equation 6.7 from the slope of each plot we can extract the polaron absorption cross section, assuming that all accumulated charge is contributing to the polaron induced absorption and that there is no other species absorbing at that energy (i.e. σ_p is negligible) and ξ and t_p are taken into account when calculating the areal charge density of polarons. There is some evidence that the absorption cross section for the holes $\sigma_h = (5.9 \pm 0.3) \times 10^{-16} \text{ cm}^{-2}$ is greater than the absorption cross section for the electrons $\sigma_e = (5.3 \pm 0.4) \times 10^{-16} \text{ cm}^{-2}$. However within experimental error the two values are comparable and it is suggested that more points are required to derive more accurate estimates of the cross section values. However this was not within the scopes of this project and was not pursued further.

The positive polaron and negative polaron induced absorption are compared

in figure 6.10. Both spectra show the PTB7 bleaching feature in the visible range with the main peak located at 1.8 eV for the positive (hole) polaron and at 1.84 eV for the negative (electron) polaron whereas the main absorption peak for the PTB7 ground state has been identified before at 1.82 eV. There is a sharp absorption peak at 1.1 eV and 1.14 eV associated with the charge induced absorption broad feature appearing for the positive polaron and negative polaron respectively. Furthermore, what is a noticeable difference beyond the 0.04 eV shift between the two spectra is a sharp negative peak at 1.7 eV present only in the negative polaron spectrum. As we will see later on this peak is present in spectra which are affected by electroabsorption effects.

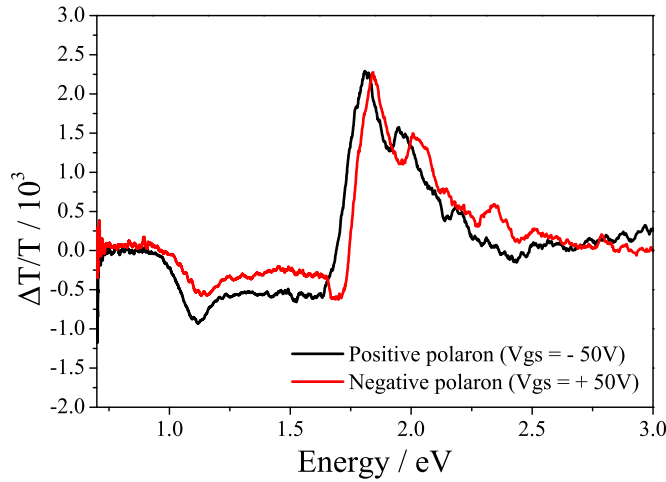


Figure 6.10: CAS spectra for a PTB7 transistor measured at -50 V and +50 V applied V_{gs} showing the positive polaron and negative polaron induced absorption respectively.

6.6.2 PTB7:PCBM Solar Cell

It is common in electromodulation spectroscopy to detect the charge induced absorption, induced by charge injection at forward voltage bias, in organic light emitting diodes. Here we are aiming to detect the charge induced absorption by calculating the difference between the solar cell optical transmission measured at short circuit conditions and the one measured at a voltage bias higher than the

6.6 Charge Induced Absorption in PTB7 Devices

open circuit voltage (to ensure efficient charge injection). Devices were loaded on the sample holder in the same manner as for OFET devices. As already mentioned the organic layer was spin-coated from blend of chlorobenzene and 1,8-diiodooctane solution to improve morphology and efficiency. 1,8-Diiodooctane has high boiling point and it's been argued in instances that significant residue remains in the film after deposition and drying. To make sure that measurements are not sensitive to changes in the organic films associated with 1,8-diiodooctane we performed optical spectroscopy measurements on thin films of just the organic layer. The annealing conditions were determined such that the films were stable i.e. there were no detectable changes in the spectra over long time-scales (hundreds of hours) that could be originating from thickness or morphology changes.

Initial attempts of CAS spectra ($\Delta T/T$) on OPV devices obtained by measuring transmittance (under dark conditions) while applying a voltage bias $T_{V_{bias}}$ and comparing to the transmittance in short circuit conditions ($T_{V=0}$):

$$\frac{\Delta T}{T} = \frac{T_{V_{bias}} - T_{V=0}}{T_{V=0}} \quad (6.9)$$

are summarised in figure 6.11. None of these spectra are recognisable CAS spectra i.e. showing an induced absorption along with a absorption bleaching signal. A spectrum with no familiar bleaching (neutral absorption) and sub-bandgap absorption features could be the result of other dominating effects originating from: (i) changes in the device thickness with applied electric field known as Electrostriction (ES), (ii) shift in the absorption of the semiconductor with electric field due to the Stark effect known as Electroabsorption (EA) and (iii) reflection and interference effects such as a standing wave.^{33,32} To identify which of the above effects is dominating the CAS signal and be able to overcome it we performed a number of control experiments. The results of two such experiments are shown in figures 6.11(b) and (c). Figure 6.11(b) shows CAS spectra at a +3 V applied voltage bias measured when the sample was oriented at different angles with respect to the spectrophotometer probe beam; and figure 6.11(c) when different ITO top-electrode thickness was used at +4 V. Any features due to reflection or interference should change once the device is rotated or its thickness is changed. We tried to identify any interference effects correlated with the ITO

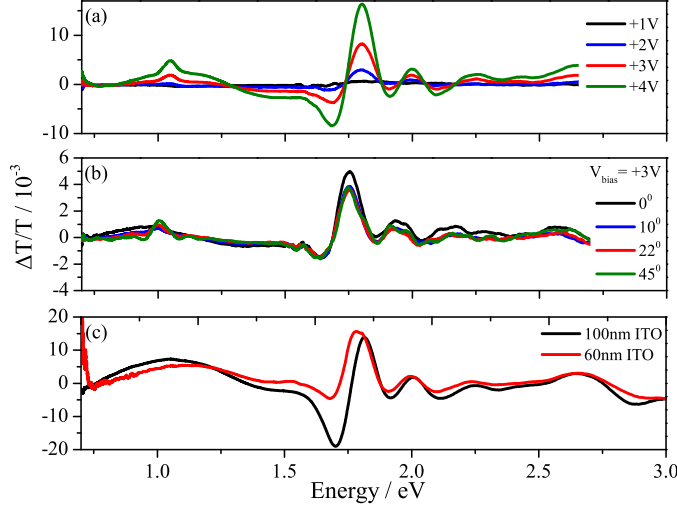


Figure 6.11: CAS spectra for PTB7/PCBM OPV devices measured (a) at different forward voltage bias, (b) at +3 V and different sample orientation with respect to the probing beam and (c) for different ITO top-electrode thickness.

top-electrode layer, due to the poor match of its refractive index with the air refractive index.³³ However this does not appear to be the case here, since all spectra are very similar. The negative peak at 1.7 eV is similar to the peak identified in the previous section for CAS measurements performed on PTB7 FET suggesting further that this feature is a result of artefacts. There is also a distinct positive peak at 1.1 eV. Since this is a positive peak it cannot be correlated to the polaron induced absorption identified earlier at 1.1 eV. The same peak is also sensitive to the sample angle and thickness of ITO which further suggest that it is a result of artefacts and it should not be mistaken with the polaron induced absorption signature. After realising that the features obtained should be due to electrostriction and/or electroabsorption effects we put more emphasis in controlling the strength of the applied electric bias. Whenever there is an absorption change, there is also a refractive index change through the Kramers-Kronig relations. The refractive index change due to EA has a quadratic dependence on the applied electric field. We decided that the best method to eliminate ES/EA effects would be by obtaining a significant detectable signal ($>$ noise signal) at the lowest possible voltage bias. Indeed by applying this practice we managed

6.6 Charge Induced Absorption in PTB7 Devices

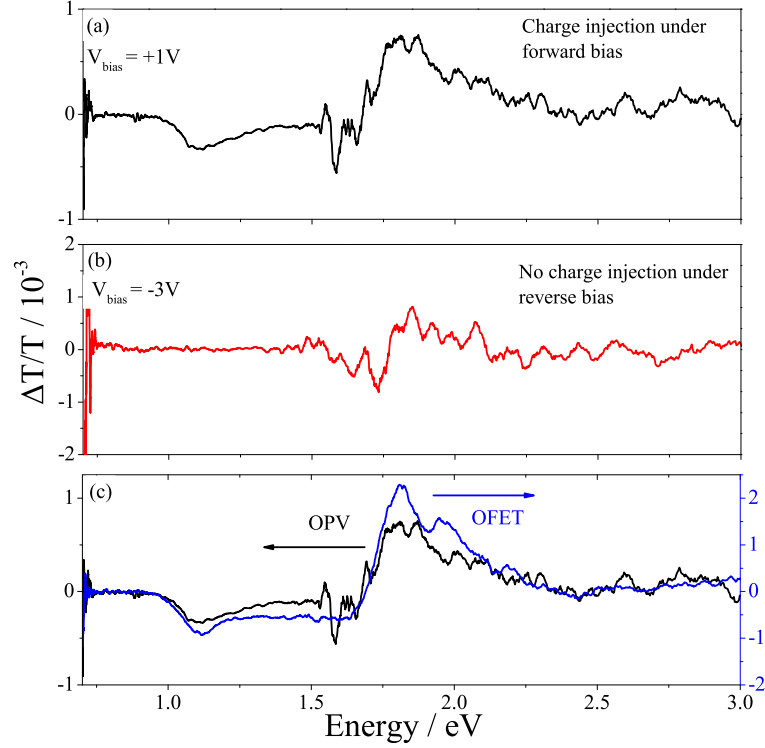


Figure 6.12: CAS spectra for (a) PTB7/PCBM OPV under forward voltage bias (charge injection) and (b) reverse voltage bias; and (c) for an OPV device (+1V) compared to a PTB7 OFET device ($V_{gs} = -50V$).

to obtain spectra at a +1 V bias, showing the characteristic charge induced absorption at 1 eV - 1.5 eV and the corresponding broad bleaching signal of the PTB7 $\pi - \pi^*$ neutral absorption at 1.8 eV - 2.2 eV (figure 6.12(a)). To further confirm the validity of this result we measured the CAS spectrum a reverse bias. For an ideal organic solar cell there should be no charge injection under reverse bias. Dark current - voltage measurements confirmed that although the current in reverse bias is not zero it is 3 - 4 orders of magnitude smaller than in the same forward bias (this is known at the rectification ratio of the device). At reverse voltage bias there was no detectable change for voltages below -3 V and the spectrum obtained for this voltage is shown in figure 6.12(b). As expected there is no charge induced absorption signal since there is no charge injection under reverse bias. The very weak signal obtained is similar to the spectra obtained at high for-

ward voltage bias possibly originating from ES/EA effects which are independent of the injected charge. A comparison of the positive polaron signature obtained using a PTB7:PCBM OPV device and a PTB7 OFET device (previous section) is shown in figure 6.12(c). The two polaron signatures are in good agreement, however the distinct peak at 1.1 eV is more pronounced for the OFET device. The broadening of the sharp 1.1 eV peak for the OPV device could be due to the fact that PTB7 is found in a blend configuration with PCBM in this case rather than pure PTB7.

Using the (positive) polaron induced absorption charge density dependence estimated from the FET CAS measurements (figure 6.9) and the polaron induced absorption features measured in the OPV CAS signal (figure 6.12) we can now estimate the induced charge density in the diode device. The polaron induced absorption feature $-\Delta T/T \approx 0.3 \times 10^{-3}$ corresponds to $\sim 10^{12}$ pol cm⁻² areal density. Since this is a diode device the polarons are distributed through the bulk of the organic layer which has a thickness of 100 nm and therefore space charge density of $\sim 10^{17}$ cm⁻³ charge density. For a unipolar space charge limited device (without traps), the maximum charge injected into the polymer is described by Child's law and equals

$$Q = \frac{3}{2}CV = \frac{3\epsilon\epsilon_0AV}{2d} \quad (6.10)$$

where $C = \epsilon\epsilon_0 A/d$ is the geometric capacitance of a device of area A and thickness d ; V is the applied bias (minus the device built-in voltage); and ϵ_0 and ϵ are the permittivity of free space and the relative permittivity of the polymer respectively. According to this model the maximum stationary concentration of charge carriers $n = C/Aq$, where q is the elementary charge, for a 100 nm thick PTB7 layer ($\epsilon = 3$) at a voltage bias of +1V is estimated at $\sim 10^{16}$ cm⁻³. The much higher charge carrier density obtained in the test OPV device $\sim 10^{17}$ cm⁻³ can be explained by considering bipolar character in the organic layer. With the introduction of second species, potentially electrons in PCBM: (a) the space-charge limit is lifted due to cancellation of the space-charge, (b) the electric field distribution can be altered and (c) the recombination of electrons and holes provides an alternative sink to charge extraction at the counter electrode.

6.7 Conclusions

The results in this chapter show how it is possible to use optical spectroscopy to study charge induced absorption in organic solar cell devices. We showed that the PTB7 polaron species identified by applying a forward voltage bias on an organic solar cell device is in good agreement with polaron absorption measurements carried out on a PTB7 transistor. However the sharp negative peak at 1.1 eV observed in the PTB7 transistor appears to be broadened in the case of the PTB7:PCBM solar cells, potentially as a result of the PCBM presence in the solar cell device. Our setup offers the advantage of performing measurements on a whole OPV device, in addition to OFETs and single or multilayer specimens without electrodes, which gives the great advantage of studying and unveiling less known instability mechanisms originating from interfaces between two materials that are not obvious on a thin film of the material itself. So far there are not direct UV-VIS-NIR optical spectroscopy evidence performed in-situ to support stability and degradation studies on organic solar cell.

We have established an experimental technique that allows simultaneous optical spectroscopy and electrical measurements over long time-scales with the option of different environmental conditions (vacuum, inert, O₂ or H₂O rich) and illumination from an external light source. This technique should provide means for studying device stability by probing the optical and electrical properties of a single device with time at different stress conditions, such as degradation in the dark or under prolonged exposure, in inert or oxygen rich and controlled humidity environments. The potential of a variety of experiments to provide extensive information on the device charge transport properties is given. The properties of the device under short circuit or open circuit conditions can be tracked in time. Furthermore it is possible by optimising further the setup to track the properties of the device under operation, i.e. under constant light illumination. In the following chapter this setup is used to study the stability of a PTB7/PCBM inverted organic solar cell.

References

- [1] Krebs, F.C. (2012) *Stability and Degradation of Organic and Polymer solar cells*, Wiley. 124
- [2] Jørgensen, M., Norrman, K., and Krebs, F.C. (2008) *Sol. En. Mater. and Solar Cells*, **92**, 686. 124
- [3] Grossiord, N., Kroon, J.M., Andriessen, R., and Blom, P. (2012) *Organic Electronics*, **13**, 432. 124
- [4] Bakulin, A., Dimitrov, S., Rao, A., Chow, P., Nielsen, C., Schroeder, B., McCulloch, I., Bakker, H., Durrant, J.R., and Friend, R.H. (2013) *J. Phys. Chem. Lett.*, **4**, 209. 124
- [5] Clarke, T.M., Lungenschmie, C., Peet, J., Drolet, N., Sunahara, K., Furube, A., and Mozer, A.J. (2013) *Adv. Energy Mater.*, **3**, 1473. 124
- [6] Wu, B., Wu, X., Guan, C., Tai, K., Yeow, E., Fan, H., Mathews, N., and Sum, T.C. (2013) *Nat. Commun.*, **4**. 124
- [7] Grancini, G., De Bastiani, M., Martino, N., Fazzi, D., Egelhaaf, H.J., Sauermann, T., Antognazza, M., Lanzani, G., Caironi, M., Franco, L., and Petrozza, A. (2014) *Phys. Chem. Chem. Phys.*, **16**, 8294. 124, 134
- [8] Presselt, M., Herrmann, F., Shokhovets, S., Hoppe, H., Runge, E., and Gobsch, G. (2012) *Chem. Phys. Lett.*, **542**, 70. 124
- [9] Hoke, E., Sachs-Quintana, I.T., Lloyd, M., Kauvar, I., Mateker, W., Nardes, A., Peters, C., Kopidakis, N., and McGehee, M.D. (2012) *Adv. Energy Mater.*, **2**, 1351. 125
- [10] Distler, A., Kutka, P., Sauermann, T., Egelhaaf, H.J., Guldi, D., Di Nuzzo, D., Meskers, S., and Janssen, R.A.J. (2012) *Chem. Mater.*, **24**, 4397. 125
- [11] Wang, N., Tong, X., Burlingame, Q., Yu, J., and Forrest, S. (2014) *Sol. En. Mater. and Solar Cells*, **125**, 170. 125

REFERENCES

- [12] Distler, A., Sauermann, T., Egelhaaf, H.J., Rodman, S., Waller, D., Cheon, K.S., Lee, M., and Guldi, D. (2014) *Adv. Energy Mater.*, **4**, 1300 693. 125
- [13] Brown, P.J. and Sirringhaus, H. (2001) *Phys. Rev. B*, **63**, 125 204. 125
- [14] Lang, D., Chi, X., Siegrist, T., Sergent, A., and Ramirez, A. (2004) *Phys. Rev. Lett.*, **93**, 076 601. 125
- [15] Sakanoue, T. and Sirringhaus, H. (2010) *Nat. Mater.*, **9**, 736. 125
- [16] Di Pietro, R. and Sirringhaus, H. (2012) *Adv. Mater.*, **24**, 3367. 126
- [17] Di Pietro, R., Fazzi, D., Kehoe, T., and Sirringhaus, H. (2012) *J. Am. Chem. Soc.*, **134**, 14 877. 126
- [18] Di Pietro, R. (2012) *Charge Accumulation Spectroscopy of Organic Semiconductors*, Ph.D. thesis, University of Cambridge. 127, 128, 129, 138
- [19] Di Pietro, R. and Sirringhaus, H. (2012) *Adv. Mater.*, **24**, 3367. 128
- [20] Pachoumi, O., Li, C., Vaynzof, Y., Banger, K.K., and Sirringhaus, H. (2013) *Adv. Energy Mater.*, **11**, 1428. 133
- [21] Soon, Y.W., Cho, H., Low, J., Bronstein, H., McCulloch, I., and Durrant, J.R. (2013) *Chem. Commun.*, **49**, 1291–1293. 134
- [22] Gupta, D., Bag, M., and Narayan, K.S. (2008) *Appl. Phys. Lett.*, **93**, 163 301. 135
- [23] Pandey, A. and Nunzi, J.M. (2011) *Appl. Phys. Lett.*, **99**, 09 309. 135
- [24] Collins, B.A., Li, Z., Tumbleston, J.R., Gann, E., McNeill, C.R., and Ade, H. (2013) *Advanced Energy Materials*, **3** (1), 65–74. 135
- [25] Kim, Y.H., Sachse, C., Machala, M.L., May, C., Müller-Meskamp, L., and Leo, K. (2011) *Adv. Funct. Mater.*, **21**, 1076. 137
- [26] Lee, J.Y., Connor, S.T., Cui, Y., and Peumans, P. (2008) *Nano. Lett.*, **8**, 689. 137

-
- [27] Hecht, D.S., Hu, L., and Irvin, G. (2011) *Adv. Mater.*, **23**, 1482. 137
- [28] Kim, Y.H., Müller-Meskamp, L., Zakhidov, A.A., Sachse, C., Meiss, J., Bikova, J., Cook, A., Zakhidov, A., and Leo, K. (2012) *Sol. Energy Mater. Sol. Cells*, **96**, 244. 137
- [29] Cao, W., Zheng, Y., Li, Z., Wrzesniewski, E., Hammond, W.T., and Xue, J. (2012) *Org. Electron.*, **13**, 2221. 137
- [30] Fahland, M., Karlsson, P., and Charton, C. (2001) *Thin Solid Films*, **392**, 334. 137
- [31] Guillén, C. and Herrero, J. (2011) *Thin Solid Films*, **520**, 1. 137
- [32] Bird, M. (2010) *Optoelectronic processes in polyfluorene ambipolar transistors*, Ph.D. thesis, University of Cambridge. 139, 143
- [33] Tkachenko, N.V. (2006) *Optical Spectroscopy: Methods and Instrumentations*, Elsevier. 143, 144

Chapter 7

Inverted Organic Photovoltaic Device Stability Investigations

In this chapter we have performed in-situ optical spectroscopy and electrical measurements on inverted OPV devices with a ZnSrO EEL to investigate their stability in the dark and under constant illumination under different environmental conditions. We show direct spectroscopic evidence of an instability with light exposure in vacuum for an ITO/ZnSrO/PTB7:PCBM/WO₃/ITO device originating from an electron transfer mechanism from the ZnSrO layer to the PCBM. The degraded EEL/acceptor interface results in high leakage currents, poor open circuit voltage and reduced fill factor. A charge transfer between the ZnSrO and PCBM is further confirmed by suppression of persistent photo-conductivity for a PCBM covered ZnSrO film compared to a bare oxide film. In addition, we present spectroscopic evidence for degradation caused by air for bare PAL films and whole devices. Finally we discuss whether overall device performance or degradation is affected by this n-type doping of the PCBM from the metal oxide EEL.

7.1 Introduction

In this chapter the optical spectroscopy experimental technique described in chapter 6 was used to study the stability of inverted organic solar cells. Semiconductor metal oxides are popular buffer layers widely used between the organic and electrode layers to improve the extrinsic stability of inverted OPV. Many studies focus on investigating the mechanisms behind the benefits in stability with metal oxides, such as reducing the diffusion rate of oxygen from air to PAL.^{1,2} Sensitivity of these materials to different conditions such as UV light illumination on the other hand is an unwanted feature. In chapter 4 we showed how the widely observed light soaking step before a good solar cell performance is achieved in an inverted OPV device comprising solution processed ZnO as ETL, can be circumvented using amorphous mixed metal oxide systems. We attributed this improvement to more efficient charge extraction at the metal oxide/organic interface. It is reasonable to wonder whether similar instabilities in the metal oxide/organic interface could affect the long term stability of the devices.

Tromholt *et al* have used the technique of concentrated light to accelerate the device degradation and reported the reversible degradation of inverted organic solar cells with a ZnO EEL.³ They attributed the degradation in the device rectification properties to an increased hole conductivity of the ZnO layer with photo-activated desorption of surface oxygen. Liu *et al* have also reported UV-assisted ageing of devices dependent on the choice of metal oxide EEL.⁴ It is common to compare device stability of devices with different EEL layers, however the mechanism behind the dependence of device stability on the choice of the EEL metal oxide material is not fully understood.⁵

In most cases the current-voltage characteristics of devices are used alone to draw a conclusion or in other cases correlated to properties of the bare materials. These methods are sometimes relevant in obtaining some understanding of the degradation mechanism paths, however they may not always give a truthful image of what really takes place in the complete device. The metal oxide layer could strongly influence polymer degradation mechanisms and kinetics. Furthermore instabilities arising under an inert atmosphere draw less attention since they might initially seem negligible or not representative of the OPV working

conditions. However we believe that studying instabilities under inert conditions could reveal underlying mechanisms associated with overall degradation. While these features might also be occurring in non-inert conditions they might not be detectable due to screening from more dominant features.

We have performed in-situ optical spectroscopy and electrical measurements on inverted OPV devices with a ZnSrO ETL to investigate the stability in the dark and under constant illumination in different environmental conditions. A charge induced absorption detected under short circuit conditions has been correlated to bleaching of the PCBM absorption and the increase in the dark reverse current suggesting a doping mechanism. Control spectroscopy, conductivity and UPS experiments indicated electron transfer from ZnSrO to PCBM resulting to an increase in PCBM anion density when the device is exposed to broadband light illumination under vacuum. Previous studies have shown the formation of a pronounced interface dipole resulting from electron transfer between the low work-function aluminium cathode and the high electron affinity C₆₀ leaving positive and negative charges on Al and C₆₀ respectively.⁶ This is the first time however that a similar electron transfer mechanism is shown to occur between the metal oxide EEL layer in an OPV device. Finally we address the issue whether an increased PCBM anion density, caused by doping from the EEL layer, might have an impact on the overall device degradation mechanisms and kinetics.

7.2 Operational Stability in Vacuum

The experimental setup and the organic solar cell devices optimised for optical spectroscopy measurements described in chapter 6 were used for the purposes of this experiment. To acquire a good understanding of the stability of the device in test and be able to identify the origin of different instabilities measured we performed experiments under different conditions by varying a number of parameters. The parameters we varied were: (i) environmental conditions: (a) Vacuum $\sim 10^{-6}$ mbar, (b) N₂/dry, (c) N₂/H₂O of controlled RH% and (d) ambient air conditions monitored by a thermometer and humidity controller and (ii) device operation: (a) dark to represent conditions when device is not in operation and (b) illumination to represent operational conditions. The temperature of the

device was monitored at all times using a temperature controller and changes in temperature due to long illumination times were of the order or $\pm 2^\circ\text{C}$. The experiments under different environmental conditions were executed in a particular order, that being from the least severe for device degradation to the most. According to literature that would be in the same series as the conditions are described above. For each environment a reference was first established for the device kept in the dark followed by operational conditions.

Optical spectroscopy results are represented as differential spectra $\Delta T/T$.

$$\frac{\Delta T}{T} = \frac{T(\tau) - T(0)}{T(0)}, \quad (7.1)$$

where $T(\tau)$ is the spectrum obtained for a sample in the dark and short circuit conditions (0 V bias), after τ time of constant light exposure and $T(0)$ is the initial reference spectrum of the sample. A device instability was described when significant changes ($>$ errors) in the optical transmittance spectra and/or the electrical measurements were recorded, over a time period of 80 hours. The error for the optical spectroscopy measurements depends on the spectrophotometer specifications and the absolute transmittance of the test sample (signal to noise ratio) and was defined empirically by the width of the $\Delta T/T$ spectrum baseline. Here we present the results obtained under vacuum/light exposure conditions which showed the most distinct features. Although not all results of the control experiments are shown we will discuss about them and use them to draw conclusions.

7.2.1 Charge Induced Absorption

In figure 7.1(a) the differential spectra obtained for an OPV device over a time period of 80 hours light exposure under vacuum ($< 10^{-6}\text{mbar}$) are shown. We can identify two distinct features, a reduced absorption ($\Delta T/T > 0$) feature in the visible/near UV region at 2.0 eV - 3.5 eV and an induced absorption ($\Delta T/T < 0$) feature in the NIR region at 0.94 eV which are both increasing with longer exposure times. We attribute the positive feature to the bleaching of the neutral PCBM absorption and the negative feature to charge induced absorption

7.2 Operational Stability in Vacuum

originating from the negatively charged PCBM radical ion. The PC₇₀BM radical anion has been measured before at ~ 0.9 eV which is in very good agreement with our estimate of 0.94 eV.^{7,8}

On a first look the two, positive and negative, features appear to correlate, however to verify the correlation we compared the evolution of the areas beneath each of the features. We know from the quantum mechanical description of the interaction of light with matter, the Beer-Lambert law and its adaptation for light absorption in semiconducting polymers that the change in transmittance, $\Delta T/T$ is proportional to the absorption cross-section (σ) of the corresponding absorbing species and the number density of the absorbing units (n) for $\Delta T/T \ll 1$ (see section 6.2 and equation 6.7). The kinetics for the two features are shown in figure 7.1(b) and they are in really good agreement, suggesting good correlation. The dark current-voltage characteristics taken in parallel are shown in figure 7.1(c). There is two orders of magnitude increase in the reverse current after 80 hours of exposure. The shunt current in forward bias is also increased meaning a decrease in the shunt resistance and resulting in a poor rectifying device with prolonged light exposure. The current obtained at a voltage greater than the turn on voltage (0.5 V) though remains unchanged (except for the first 5 hours). A similar loss in the rectification properties of a similar ZnO EEL device with concentrated light exposure has previously been attributed to hole shunts in ZnO with oxygen desorption.³ We have shown before improvement in rectification with UV light exposure over shorter time-scales for similar devices.⁹ A direct conclusion cannot be drawn from just current-voltage characteristics however the increase in shunt current, at very low voltage, could be correlated to an increased n-type conductivity in the photoactive layer.

To explore the possibility that the increase in reverse (and shunt) current and the observed charge induced absorption originate from the same induced charge species we studied the kinetics of the two changes. figure 7.1(d) shows (i) the dark current measured at -1 V bias and (ii) the transmittance % at 0.94 eV (CIA peak) over the 80 hour exposure period. The fact that the two graphs show very similar behaviour suggests a correlation between the two. The CIA could originate from an induced negatively charged species leading to strong decrease in the shunt resistance and increase in leakage current. We attribute the feature in the Vis/UV

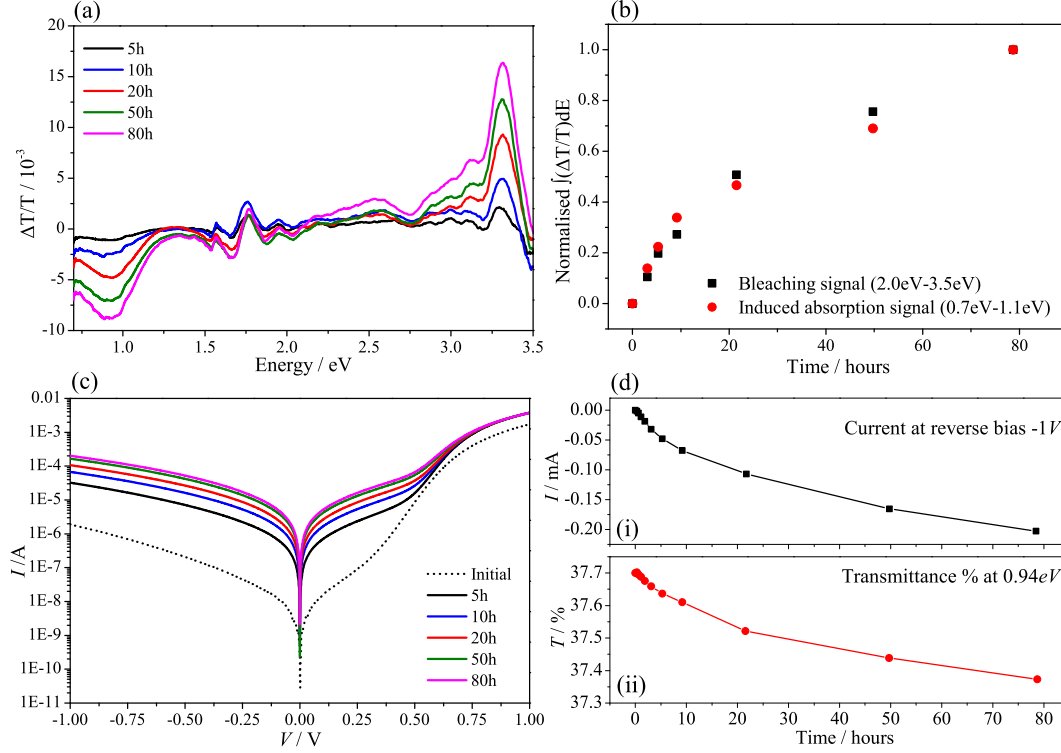


Figure 7.1: (a) Differential optical transmittance spectra for OPV device after prolonged light exposure, (b) Normalised area evolution over time under bleaching and CIA signals corresponding to spectra shown in (a), (c) corresponding dark current-voltage characteristics, (d) comparison between kinetics of (i) reverse current increase and (ii) CIA peak transmittance decrease.

region due to bleaching of the PCBM $\pi - \pi^*$ neutral absorption. Figure 7.2(a) shows a good agreement between the ground state PCBM absorption (measured for a thin film) and the bleaching feature. The bleaching feature shows the typical 2.5 eV main absorption peak of PCBM and further extends in the near UV region 2.6 eV - 3.3 eV following the vibronic structure of PCBM absorption, although the bleaching signal is significantly broadened. Near the UV region the signal is dominated by features originating from the ZnSrO layer discussed later on. We already know from the spectrum obtained for the bare PTB7:PCBM film under same conditions (50 hours of light exposure in vacuum), that the PAL itself is stable under these conditions since there was no detectable change as shown in

figure 7.2(c), and we conclude that the bleaching of PCBM in a device must be a result of an interfacial effect. The latter assumption is further supported by the spectrum obtained for a ZnSrO/PTB7:PCBM bilayer sample (under same conditions). The spectrum for the ZnSrO/PTB7:PCBM as shown in 7.2(b) is

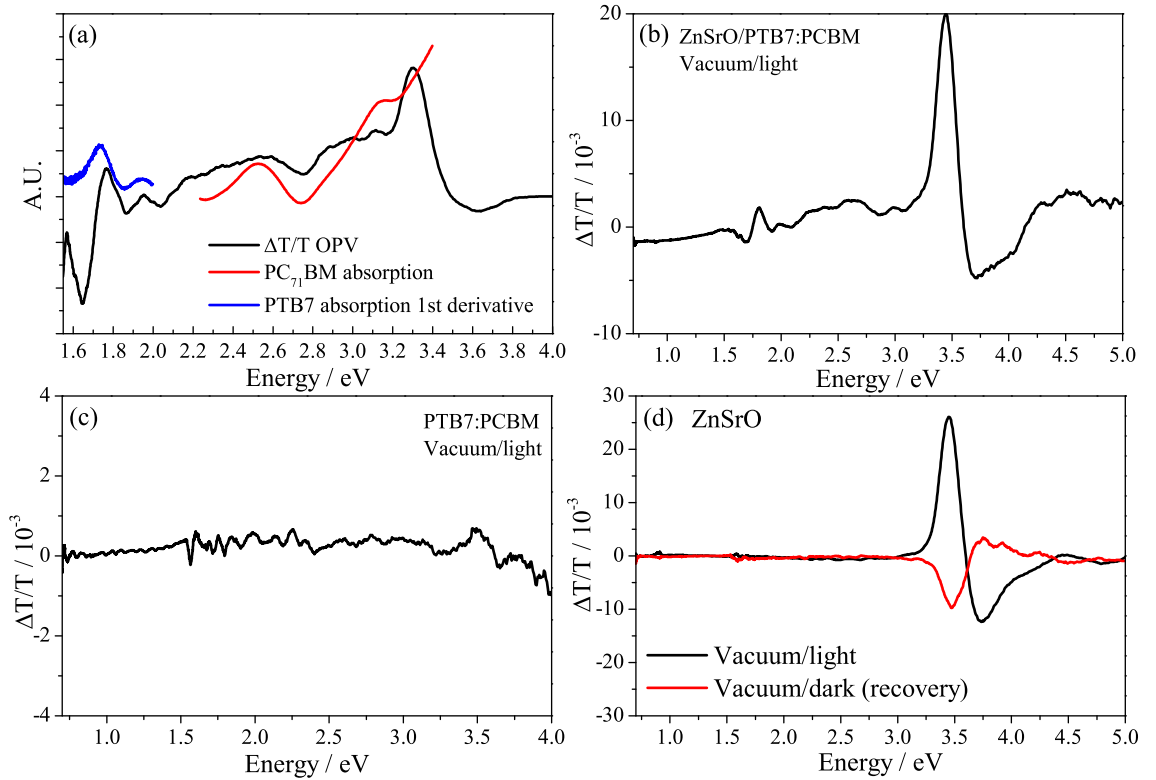


Figure 7.2: (a) Differential spectrum of the transmission in the Vis/UV region, compared with absorption spectrum of a bare PCBM film and the first derivative of the PTB7 bare film absorption, changes in transmission of a (b) ZnSrO/PTB7:PCBM multilayer sample, (c) PTB7:PCBM sample and (d) ZnSrO sample after 50 hours of light exposure in vacuum.

very similar to the OPV device spectrum. It consists of a positive peak in the PCBM absorption region and the 2.5 eV peak as well as a negative feature in the NIR region. However both these features seem to be a lot less pronounced and the spectrum is dominated by the ZnSrO features in the 3.0 eV - 4.5 eV region. The signature of the features originating only from the ZnSrO layer is obtained by performing the same measurement for a bare ZnSrO film and it is shown

in figure 7.2(d). The resulting spectrum for ZnSrO shows reduced absorption coming from the low energy (just below E_g) transitions and increased absorption from higher energy transitions (just above E_g). This can be explained by de-trapping of electrons with oxygen desorption. The previously trapped charges contributing towards the sub-band gap absorption are now contributing to above E_g absorption. This effect is reversible when the film is relaxed in the dark, coming in line with the surface oxygen adsorption/desorption theory. The fact that there is not feature in the NIR region for the bare ZnSrO or film but is present for the ZnSrO/PTB7:PCBM film and OPV device, accompanied with a bleaching of the 2.5 eV PCBM absorption, further supports the theory that the peak at 0.94 eV is due to the PCBM anion. The small feature at 1.6 eV - 1.8 eV does not resemble the PTB7 neutral absorption bleaching (see section 6.6.2), instead it seems to replicate the first derivative of the PTB7 absorption (measured for a thin film) and therefore could be due to a shift in the PTB7 absorption as a result of electroabsorption effects.

We can use the CAS spectrum (figure 7.1(a)) for the degraded device in combination with the absorption spectrum for a PCBM film of known thickness (not shown here) to estimate the fraction of PCBM molecules that become anions. We will assume that the amount of PCBM that become anions is equal to the amount of PCBM molecules that have been bleached. Using Beer-Lambert's law (see equation 6.3) we can estimate the fractional change in "thickness" t_i associated with the change in transmission of the characteristic 2.5 eV PCBM absorption peak. Assuming an even density throughout the PCBM film this corresponds to the molecular fraction. Substituting the transmission value of $\sim 30\%$ and film thickness $t_0 = 90$ nm we estimate the absorption coefficient $\alpha = \sigma n$ for the 2.5 eV PCBM absorption as $\sim 13 \times 10^6 \text{ m}^{-1}$. From figure 7.1(a) the change in transmittance corresponding to the 2.5 eV bleaching signal after 80 hours is equal to $\frac{\Delta T}{T} = 2.5 \times 10^{-3}$. We solve the following equation to estimate the thickness t_{deg} corresponding to the degraded film.

$$\begin{aligned} \frac{\Delta T}{T} &= \frac{T_{deg} - T_0}{T_0} \\ &= \frac{e^{-\alpha t_{deg}} - e^{-\alpha t_0}}{e^{-\alpha t_0}} \end{aligned} \quad (7.2)$$

The fraction of PCBM molecules that have become anion is found to be $\sim 0.2\%$.

7.2.2 Device Performance

In figure 7.3 we present the corresponding current-voltage characteristics measured under light conditions and the key performance parameters (V_{OC} , J_{SC} and FF) are calculated. The PCE values were not calculated since the intensity of the light source at the point of illumination on the sample was not calibrated. There is a decrease in the values of all the parameters with light exposure in vacuum. Significant losses in V_{OC} and FF can be assigned to the decrease in the shunt resistance and increase in dark current mentioned earlier. In order to investigate the dependence of the open circuit voltage changes to the increase in dark current we use equation 2.17 which relates V_{OC} to J_{SC} and J_0 (dark saturation current).

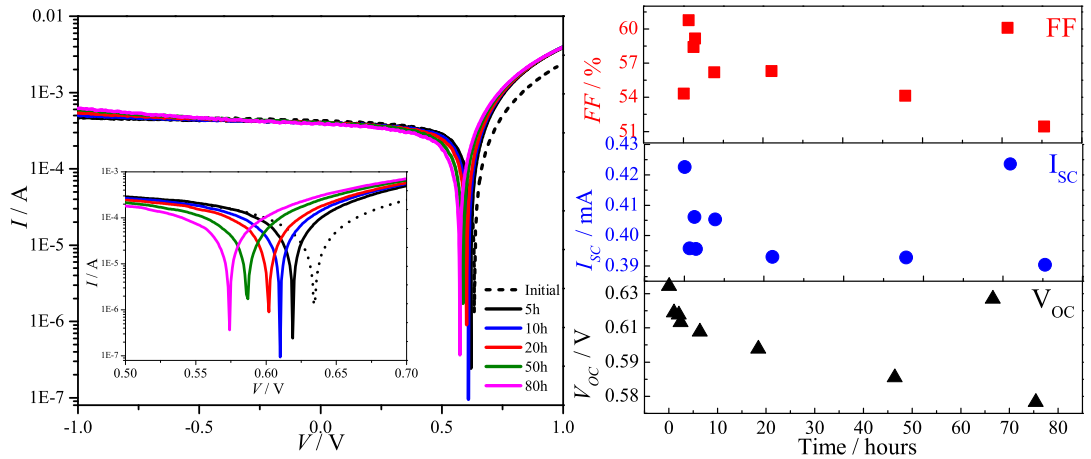


Figure 7.3: Light current-voltage characteristics after different times of light exposure under vacuum (left) and respective key performance parameters (V_{OC} , J_{SC} and FF)(right).

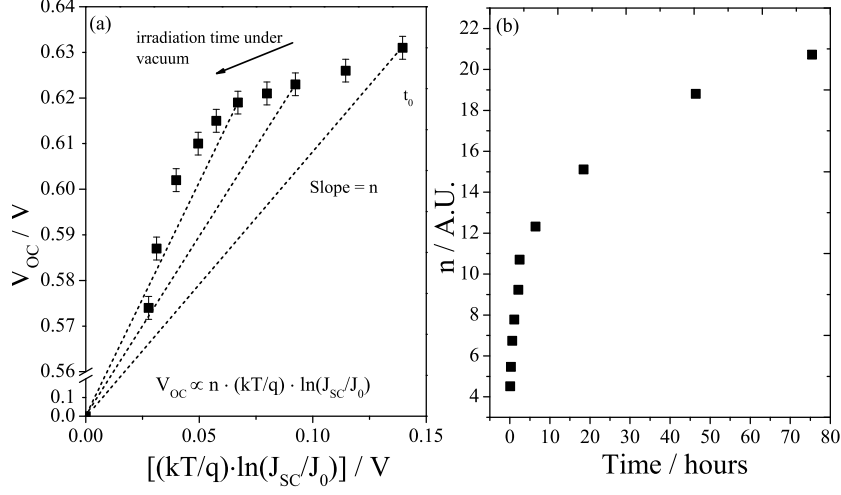


Figure 7.4: (a) V_{OC} against $\ln(J_{SC}/J_0)$ for prolonged light exposure under vacuum conditions. V_{OC} and J_{SC} parameters were extracted from results shown in figure 7.3 and J_0 from the dark IV measurements shown in figure 7.1 (b) Ideality factor, n , as derived from slope against light exposure time.

In figure 7.4(a) we have plotted V_{OC} against $\ln(J_{SC}/J_0)$ measured for devices irradiated in vacuum. All parameters were extracted from results obtained from the same one device. V_{OC} and J_{SC} parameters were extracted from results shown in figure 7.3 and J_0 from the dark IV measurements shown in figure 7.1. In figure 7.4(b) the evolution of the ideality factor n as derived from the slope of the extrapolated line to the origin, with light exposure times is shown. An increase in the value of n has been correlated before with a dominant loss mechanism originating from trap-assisted recombination. It is possible that after long exposure times and increased concentration of PCBM anions the charge separation at the PTB7/PCBM interface is degraded due to recombination aided by trapped electrons at the interface. The decreased J_{SC} can be related to the decreased absorption of PCBM and hence photogenerated charges or due to less efficient charge separation that could be caused by the changes in the PCBM properties.

7.2.3 Suggested Mechanism

So far we have identified a degradation mechanism taking place with light exposure under vacuum conditions, associated with the accumulation of PCBM anions in the PAL and potentially originating from charge transfer at the PCBM/ZnSrO interface. We know from previous research and results discussed in chapter 4 that the surface properties of ZnSrO and hence device performance is sensitive to surface oxygen desorption that can occur with UV illumination. In this section we have performed experiments focusing on the doping of ZnSrO with UV exposure in vacuum and the persistent photo-conductivity effect in ZnSrO in order to identify the origin of the accumulation of PCBM anions.

ZnO n-type Doping

ZnO conductivity increases with UV light exposure due to electron de-trapping with surface oxygen desorption aided by photo-generated charges. It has also been reported that surface oxygen desorption and an increase in the conductivity can occur by annealing ZnO at high temperatures in a reducing or inert atmosphere (e.g. N₂ or Vacuum) (see section 4.2.5). This is attributed to an increase in the electrons lying in the conduction band due to n-type doping with the de-trapping of surface electrons. In figure 7.5(left) the UPS spectra for an as prepared ZnSrO thin film compared to one that has been subjected to an additional 1 hour annealing step at 300⁰C in nitrogen atmosphere are shown. Both values for the workfunction and the positioning of the fermi level from the valence band minimum are increased for the nitrogen annealed film. The bandgap remains unaffected by this additional annealing step as verified by UV-Vis absorption measurements (not shown here). The corresponding energy level diagrams are shown in the inset. We can see that the fermi level for the annealed film is positioned deeper in the conduction band and is in agreement with the increased film conductivity and the suggested n-type doping mechanism. The increase in workfunction indicates a more electronegative surface and an associated induced dipole moment with nitrogen annealing. Exposure of ZnO films to normal atmospheric conditions leads to surface contamination by hydrocarbon and hydroxyl species and the presence of these chemisorbed and physisorbed groups leads to changes to

the electronic properties of the surface such as WF and sheet resistance. However, the specific mechanisms that are responsible for the changes in surface WF of metal oxide films remain highly debated.^{10,11} The dominant hypothesis is that electronegative adsorbates will in general increase the work-function of a surface, whereas electropositive adsorbates lead to a decrease, however there is evidence to suggest that the workfunction changes are not always governed by the sign and quantity of adsorbate.¹²

Based on the assumption that surface oxygen is desorbed with nitrogen annealing we would expect a respective decrease in the workfunction value, however there might be other factors contributing to an increased dipole in the opposite direction. It has been reported before that the WF is increased with removing of surface carbon contaminants as well as with small changes in the stoichiometry with different annealing temperatures and conditions. It is possible that the stoichiometry at the film surface is affected during the additional annealing step by either reducing surface carbon contaminants (see figure 4.4) and increasing overall lattice oxygen contribution despite the desorption of surface oxygen.^{11,10,13} Although the UPS measurements shown here are not representative of the effect happening with UV light exposure we believe the increase in conductivity is a result of the n-type doping mechanism with surface oxygen desorption in both cases and that the shift of the fermi level deeper in the conduction band is true for both cases. Surface oxygen desorption should in principle be more favourable in the absence of oxygen and therefore we would expect significant doping of Zn-SrO with light exposure in vacuum. Next we investigated whether this significant doping of ZnSrO might be the origin of the PCBM/ZnSrO instability by means of persistent photoconductivity measurements.

Persistent Photoconductivity

In the field of metal oxide UV photo-detectors it is common that the measured photoconductivity for a film shows a persistence rather than immediately returning to a base level of current once the light is off. This effect is referred to as Persistent Photoconductivity (PPC). The photocurrent relaxation is characterised by a two-step process, consisting of an initial sharp drop in photoconductivity followed by a slow decline in current. The initial sharp drop is understood

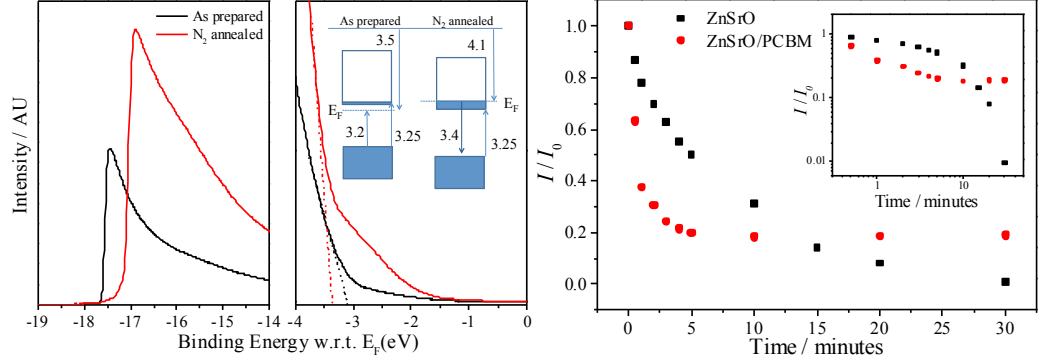


Figure 7.5: (Left) UPS spectra for an as prepared ZnSrO thin film compared to one that has been subjected to an additional 1 hour annealing step at 300°C in Nitrogen atmosphere. The absorption onset shows an increased WF and the edge of absorption shows an increase in the VBM and hence n-type doping. The inset shows corresponding energy level diagrams. (Right) PPC decay for a bare ZnSrO film and a PCBM covered ZnSrO film. Insert is the same in a double logarithmic scale.

by the immediate relaxation of the majority of photogenerated charges. The slow decline and hence the persistence effect is attributed to the rates of various excitation-recombination mechanisms. After photo-excitation, surface oxygen is desorbed, and trapped electrons move to the conduction appearing as persistent photo-conductivity. However, with increasing time, the re-adsorption of oxygen at the surface and/or electron trapping in the depletion region leads to a decrease in the measured current. There is a significant debate in the literature about the underlying processes governing the persistence conductivity observed in ZnO. Usually, the PPC decay is described either by the Gaussian distribution of capture barriers,¹⁴ or using the Kohlrausch function, so-called “stretched exponential” function.^{15,16,17}

Figure 7.5(a) shows the current relaxation post UV light illumination for a ZnSrO film and a ZnSrO/PCBM bilayer sample on glass. Current measurements were performed by means of two-point probe conductivity measurements as. We can see that the kinetics for the two films are very different with the relaxation process for the ZnO films which is covered by an ultra thin ($\sim 5 - 10$ nm) PCBM layer being overall faster. The inset shows the same results in a log-log scale.

The resulting plot for ZnSrO film shows typical behaviour observed in the field of photodetectors.^{15,18} The deviation of the PPC kinetics for the PCBM covered ZnSrO film from that of the bare ZnSrO film suggests the involvement of a different energy transfer mechanisms.^{19,20} We therefore suggest that at high doping levels of ZnSrO, a result of prolonged light exposure in vacuum, there is an electron transfer from the oxide to the PCBM layer in order for the fermi levels of the two materials to align, which quenches the PPC. This additional charge in the PCBM results in the bleaching of the neutral absorption and an increase in the absorption of the PCBM anion species. This mechanism is in good agreement with the spectroscopy results discussed earlier. The charge induced absorption at 0.94 eV is attributed to the PC₇₀BM anion and is in good agreement with what has been measured before.^{7,8} Similar spectra showing a CIA and PCBM bleaching were obtained for prolonged light exposure experiments carrier out in dry/nitrogen and (controlled RH% H₂O/nitrogen atmospheres (not shown here). However for the same time-scales the signal was much less, further suggesting that the instability originates from the oxide surface oxygen desorption mechanism. In addition, there was no detectable change when devices were kept in the dark in inert atmosphere.

7.3 Operational Stability in Ambient Air

In this section we present results obtained for degradation of devices under illumination in ambient air conditions. During the course of the experiment the room temperature and relative humidity were monitored to lie in the range of 20°C - 23°C and 30% - 50% at all times. The presence of oxygen under illumination conditions is considered to be the primary and most damaging source of degradation for an organic solar cell due to photooxidation of the conjugated polymer. Photooxidative degradation of active OPV materials is also refer to as photo-bleaching because the process leads to loss of conjugation destroying the chromophores responsible for the color.

We have recorded the photo-bleaching effect for a device with a PTB7:PCBM PAL (figure 7.6(left)) as well as the bare PAL itself (figure 7.6(right)). The graphs are offset for clarity. Both features show a bleaching of the PTB7 absorption

similar to the bleaching signal from PTB7 transistor CAS measurements shown in the figure inset. The high sensitivity of the setup allows us to directly compare the values of the changes in transmittance, $\Delta T/T$. For example after 20 hours of light exposure in air the amount of PTB7 bleaching for the device is ($\sim 4 \times 10^{-3}$) two orders of magnitude smaller than in the case of a bare blend film ($\sim 400 \times 10^{-3}$). This technique could provide means for comparing the barrier effect achieved in a particular device architecture configuration.

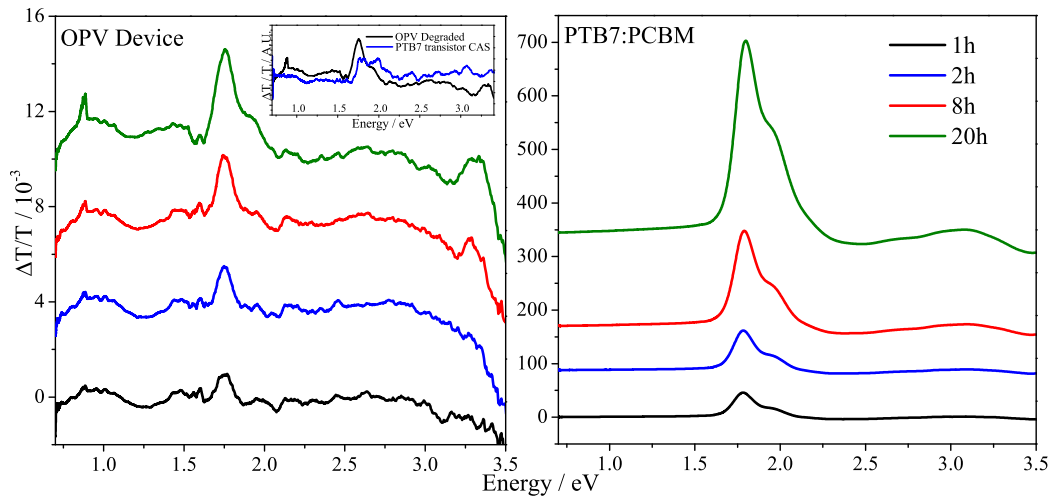


Figure 7.6: Change in transmission with constant illumination in air for OPV PTB7:PCBM device (left) and a PTB7:PCBM bare film (right). Graphs are offset for clarity.

7.4 Conclusions

We have shown that charge transport in an organic solar cell device can be investigated by means of high resolution optical spectroscopy and electrical measurements. We show direct spectroscopic evidence of an instability with light exposure in vacuum for an ITO/ZnSrO/PTB7:PCBM/ WO_3 /ITO device. The bleaching of the neutral PC_{70}BM absorption is associated with a charge induced absorption which we assign to the PC_{70}BM anion due to an electron transfer process from the highly doped ZnSrO to the PCBM HOMO. The resulting degradation

of the ZnSrO/PCBM interface manifests itself in electrical characteristics by a decreased shunt resistance and high leakage dark current which lead to a drop in the open circuit voltage and fill factor for operation under illumination. It is possible that the change in the open circuit voltage might also be associated to a change in the PCBM HOMO with doping, however this needs to be further investigated.

The role of the Donor/Acceptor (polymer/fullerene) interface and the interfacial charge transfer state in the degradation process caused by air has previously shown to be critical.^{21,22,23} Furthermore, Trukhanov *et al*²⁴ and Gregg *et al*.²⁵ suggest by numerical modeling that doping of the organic materials by majority carriers (i.e. n doping for the acceptor and p doping for the donor) increases all the solar cell parameters (V_{OC} , J_{SC} , FF and PCE) as a result of an increased interfacial electric field at the donor/acceptor interface leading to an increased dissociation rate of bound electron hole pairs. There are still relatively few reports of controlled doping in organic semiconductors^{26,25} and fullerenes in specific.^{27,28}

Despite the poor operation of devices after prolonged light exposure in vacuum, the question whether overall device performance or degradation is affected by this n -type doping of the PCBM from the metal oxide ETL. Further investigation of the device performance with PCBM doping is recommended. An experiment comparing the photooxidative degradation for an as prepared device to a vacuum/light degraded device by means of optical spectroscopy and electrical measurements could reveal whether a highly doped fullerene is significant in the degradation process and whether it inhibits or leads to new degradation pathways. We realise that the current setup offers a versatility of measurements. Probing changes for a device while at open circuit voltage bias could give information on mechanisms that depend on charge carrier concentration and while at external light bias could give information on trap states associated with photo-generated charges. In addition, pump push photocurrent measurements on devices with a n doped PCBM and an as prepared PCBM could give information on the efficiency of bound charge pairs.

References

- [1] Cao, H., , He, W., Mao, Y., Linc, X., Ishikawa, K., Dickersone, J.H., and Hess, W. (2014) *Journal of Power Sources*, **264**, 168. 152
- [2] Li, J., Kim, S., Edington, S., Nedy, J., Cho, S., Lee, K., Heeger, A.J., Gupta, M., and Yates Jr, J. (2011) *Sol. En. Mater. and Solar Cells*, **95**, 1123. 152
- [3] Tromholt, T., Manor, A., Katz, E.A., and Krebs, F.C. (2011) *Nanotechnology*, **22**, 225 401. 152, 155
- [4] Liu, H., Wu, Z., Hu, J., Song, Q., Wu, B., Tam, H.L., Yang, Q., Choi, W.H., and Zhu, F. (2014) *Appl. Phys. Lett.*, **104**, 103 901. 152
- [5] Hänsel, H., Zettl, H., Krausch, G., Schmitz, C., Kisselev, R., Thelakkat, M., and Schmidt, H.W. (2002) *Appl. Phys. Lett.*, **81**, 2106. 152
- [6] Matz, D.L., Ratcliff, E.L., Meyer, J., Kahn, A., and Pemberton, J.E. (2013) *ACS Appl. Mater. Interfaces*, **5**, 6001. 153
- [7] Liedtke, M., Sperlich, A., Kraus, H., Deibel, C., Dyakonov, V., Filippone, S., Delgado, J., Martin, N., and Poluektov, O. (2010) *ECS Transactions*, **28**, 3. 155, 164
- [8] Sperlich, A., Liedtke, M., Kern, J., Kraus, H., Deibel, C., Filippone, S., Delgado, J.L., Martín, N., and Dyakonov, V. (2011) *Phys. Status Solidi*, **5**, 128. 155, 164
- [9] Pachoumi, O., Li, C., Vaynzof, Y., Banger, K.K., and Sirringhaus, H. (2013) *Adv. Energy Mater.*, **11**, 1428. 155
- [10] Kuo, F.L., Li, Y., Solomon, M., Du, J., and Shepherd, N.D. (2012) *J. Phys. D: Appl. Phys.*, **45**, 065 301. 162
- [11] Forsythe, E.W., Gao, Y., Provost, L.G., and Tompa, G.S. (1999) *J. Vac. Sci. Technol. A*, **17**, 1761. 162
- [12] Leung, T., Kao, C., and Su, W. (2003) *Phys. Rev. B*, **68**, 195 408. 162

-
- [13] Park, S., Kim, H.J., Cho, M.H., Yi, Y., Cho, S., Yang, J., and Kim, H. (2011) *Appl. Phys. Lett.*, **98**, 082111. 162
- [14] Hirsch, M.T., Wolk, J.A., Walukiewicz, W., and Haller, E.E. (1997) *Appl. Phys. Lett.*, **71**, 1098. 163
- [15] Ursaki, V.V., Tiginyanu, I.M., Riccia, P.C., Anedda, A., Hubbard, S., and Pavlidis, D. (2003) *J. Appl. Phys.*, **94**, 3875. 163, 164
- [16] Bao, J., Shalish, I., Su, Z., Gurwitz, R., Capasso, F., Wang, X., and Ren, Z. (2011) *Nanoscale Research Letters*, **6**, 404. 163
- [17] Moore, J. and Thompson, C. (2013) *Sensors*, **13**, 9921. 163
- [18] Trzmiel, J., Weron, K., and Placzek-Popko, E. (2008) *J. Appl. Phys.*, **103**, 114902. 164
- [19] Carrey, J., Carrere, H., Kahn, M., Chaudret, B., Marie, X., and Respaud, M. (2008) *Semicond. Sci. Technol.*, **23**, 025003. 164
- [20] Berberan-Santos, M., Bodunov, E., and Valeur, B. (2005) *Chem. Phys.*, **315**, 171. 164
- [21] Grancini, G., De Bastiani, M., Martino, N., Fazzi, D., Egelhaaf, H.J., Sauermann, T., Antognazza, M., Lanzani, G., Caironi, M., Franco, L., and Petrozza, A. (2014) *Phys. Chem. Chem. Phys.*, **16**, 8294. 166
- [22] Distler, A., Kutka, P., Sauermann, T., Egelhaaf, H.J., Guldi, D., Di Nuzzo, D., Meskers, S., and Janssen, R.A.J. (2012) *Chem. Mater.*, **24**, 4397. 166
- [23] Aguirrea, A., Meskers, S.C.J., Janssen, R.A.J., and Egelhaaf, H.J. (2011) *Organic Electronics*, **12**, 1657. 166
- [24] Trukhanov, V.A., Bruevich, V.V., and Paraschuk, D.Y. (2011) *Phys. Rev. B*, **84**, 205318. 166
- [25] Gregg, B.A. (2009) *Soft Matter*, **5**, 2985. 166

REFERENCES

- [26] Gregg, B.A., Chen, S.G., and Cormier, R.A. (2004) *Chem. Mater.*, **16**, 4586. 166
- [27] Li, C.Z., Yipab, H.L., and Jen, A.K.Y. (2012) *J. Mater. Chem.*, **22**, 4161. 166
- [28] Li, C.Z., Chuen, C.C., Yip, H.L., Ding, F., Li, X., and Jen, A.K.Y. (2013) *Adv. Mater.*, **25**, 2457. 166

Chapter 8

Conclusions and Outlook

In this work an extensive suite of photophysical and electrical experimental techniques were used to study the interfacial physics of organic/metal oxide interfaces in photovoltaic applications. We have demonstrated the crucial role of interfaces in performance and stability of inverted organic photovoltaics both short and long-term. In specific we report that in the case of solution processed Zinc Oxide with unstable surface properties it is important that the origin of these instabilities needs to be well understood and better controlled as well as taken into account when reporting consistent results. It is suggested that the nature of the resulting outcome of an experiment involving such a layer might be completely altered by the way the experiment is being carried out.

A major topic of our experiment focuses on the application of a particular class of materials, transparent conducting n-type mixed metal oxides which are a promising improved alternative to popular but unstable binary systems such as ZnO. We have showed how thin films of ternary metal oxides, ZnSrO and ZnBaO can be easily deposited by a simple one-step sol-gel solution deposition technique using molecular alkoxide precursors. The resulting oxides of high quality, uniformly doped throughout the thickness of the film, highly transparent with similar band-gaps to the undoped ZnO and have an amorphous nature and a smooth surface. Although the three oxides show similar oxygen deficiency the particular environment of the different oxygen species contributing towards the total oxygen in the films is very important for the resulting film properties. As it was proven that the sensitivity of the conductivity of ZnO to UV

light irradiation, nitrogen annealing or deposition conditions can be suppressed with alkaline earth metal doping. Furthermore the commonly observed UV light soaking step before a good device performance is achieved was circumvented when using doped ZnO and an overall superior performance was achieved for an ITO/ZnO/P3HT:PCBM/WO₃/Ag solar cell. Incorporating alkaline earth metals in the ZnO lattice helps reduce electron trapping on the surface associated with oxygen adsorption, which in pure ZnO leads to band bending in the ZnO film towards the surface and an associated reduction in the built-in electric field and device performance. The fact that the overall contribution of oxygen that is not fully coordinated in the doped films often attributed to oxygen vacancies and adsorbed groups, is higher while the oxygen desorption effect with UV light and interfacial dipole are reduced raises more questions regarding the possible environments of oxygen species in the film and it is worth investigating further. It is possible that the mobility of the oxygen deficient sites is an additional factor to determine surface oxygen adsorption and the stability of the metal oxide.

Ternary, quaternary etc. oxides might be the answer towards engineering materials with suitable properties depending on the needs of application. We have shown that the surface properties of metal oxides are not just significant for the resulting electrical properties but also for coverage with a subsequent layer. In hybrid ZnO/P3HT devices strontium doping of ZnO can be used to improve surface modification of ZnO with a self assembled monolayer, PCBA and lead to superior devices. The increased coverage of ZnSrO with PCBA was correlated to a surface defect state which is more pronounced for a ZnSrO film compared to undoped ZnO. Overall not fully coordinated oxygen is higher for doped ZnO, adsorbed oxygen species inducing surface band-bending are reduced and a defect state promoting PCBA adsorption is more pronounced.

A high-resolution optical spectroscopy characterisation technique for studying stability and degradation of organic solar cells has also been reported. We describe the development and implementation of an appropriate spectroscopy setup which allowed us to detect changes in transmittance of the order of $\Delta T/T \sim 10^{-4}$ over long time-scale in-situ measurements. The PTB7 polaron induced absorption was detected in a PTB7:PCBM OPV device without the use of a modulation technique. PTB7 polaron induced absorption was measured as a broad peaks cen-

tred at 1.1eV and was in excellent agreement with charge accumulation results obtained for a PTB7 field effect transistor. Understanding and minimising any contributions towards the resulting optical spectra originating from electroabsorption, interference and electrostriction effects is critical in obtaining reliable results.

The above technique has indicated an instability for a PTB7:PC₇₀BM inverted solar cell with a ZnSrO electron transport layer when photoexposed in vacuum over tens of hours. There is a noticeable increase in the shunt current and a sharp decrease in the open circuit voltage of such a solar cell over long-term exposure to broadband light of high intensity when the device is kept under vacuum conditions. Spectroscopic evidence showed that this degradation is accompanied by a bleaching of the neutral PC₇₀BM absorption and a charge induced absorption located in the NIR and centred at ~ 0.9 eV. The charged species causing the induced absorption was identified as the negatively charged PC₇₀BM radical ion. This degradation was attributed to an electron transfer mechanism from a heavily doped ZnSrO to PCBM. The effect of surface oxygen photo-desorption and electron de-trapping is more favourable in vacuum conditions leading to a heavily doped oxide with a fermi level deeper in the conduction band. Although the light soaking step problem was overcome with the use of the more stable doped oxide it seems that the resulting device is still not free of the oxide's surface instabilities.

It would be really interesting to investigate further whether an excess of PC₇₀BM radical anions in a PTB7:PC₇₀BM blend or any other polymer / fullerene blend might affect the photo-oxidation mechanisms and kinetics since the Donor / Acceptor (polymer / fullerene) interface and the interfacial charge transfer state has previously shown to determine the degradation process caused by air. As a start *pump push photocurrent spectroscopy* measurements for a PTB7 : (*undoped*) PCBM and a PTB7 : (*doped*)PCBM active layer should indicate whether charge separation efficiency is at all affected by the PCBM doping level. Similar experiments to that in chapter 7 could reveal charge trapping mechanisms associated with the organic layer. For example instead of determining the steady state transmission of the device we could detect transmission under open circuit conditions which should give information on the free charges; or we could measure the photo induced absorption and the exciton pair while the device is degrading.
